POLITECNICO DI TORINO
DET - Dipartimento di Elettronica e Telecomunicazioni

Master degree in Electronic Engineering

Multiterminal solar cells with heterojunction-bipolar transistor structure: analysis and design

Supervisor:

Prof. Federica Cappelluti

Candidate:

Gemma Giliberti

April, 2019

Ai miei genitori,
ai quali devo questo importante traguardo. Grazie per tutti i vostri insegnamenti.
Grazie per avermi trasmesso il valore dello studio.
A mia zia Gina, a mio zio Dino che mi hanno da sempre amata e sostenuta.
Al mio nipotino Giuseppe che ha portato tanta allegria durante le mie sessioni estive.
A mia sorella Oriana che aspetta sempre una chiamata.
Grazie per tutte le tue preghiere. Grazie per esserci.
A tutta la mia grande e amata famiglia.
Grazie.

Un ringraziamento speciale ad un gruppo di amiche fantastiche
Megragrosa.

Un Grazie infinito a Marta che, con la sua allegria e dolcezza, mi ha supportato e sopportato in questi ultimi due anni.

Un ringraziamento particolare alla professoressa Cappelluti che mi ha seguita con attenzione ed interesse durante l'intero percorso di tesi. Si ringrazia, inoltre, il professore Bonani per il contributo alla formulazione del modello di Hovel esteso alla struttura bipolare.

Contents

Introduction

Every living thing on Earth exists thanks to a delicate balance held by the Sun that is not only the starting point for the chemical and biological chains, but also is necessary for the development of our society. One of the most important problems of the modern age is being able to combine the economic and technological growth with the global warming and atmospheric pollution. In this scenario, the "clean energies" represent an alternative to the fossil-fuel system.

Among the several energy sources, the solar power is probably one of the most interesting because it can be converted directly into electricity by the solar cell device. In the past, solar cells were limited to space and military applications due to the low conversion efficiency and high manufacturing cost. Today, thanks to a constant research, different kinds of solar cells are not used only in satellite operations or space manufacturing but also for terrestrial applications.

Although many important results have been achieved in the last few years, it is necessary continue investing on the realization of high-performing and low-cost solar cells. This would help the photovoltaic technology to definitively placing on the global market becoming the most important driver in the development of modern societies.

Today, multi-junction (MJ) solar cells achieve the highest performance by stacking several compound semiconductors able to absorb different wavelength ranges of the sun spectrum. Increasing the number of junctions leads to high efficiency alongside to a higher device complexity.

In the thesis it is investigated the possibility of a new kind of solar cell similar to a heterostructure bipolar transistor (HBJT) in order to overcome several constraints of the traditional MJ cells and to achieve a simpler structure. Several simulations lead to a confident conclusion about the possibility of implementation of a HBJT structures as solar energy absorbers, in fact it seems that their efficiency approaches that one of a dual-junction solar cell.

The hope is that, through the following Chapters to the discovery of the features of several solar cells, it may glimpse in the solar power a real alternative to the "non renewable sources".

CHAPTER 1

A green energy future

We live in a world where the *energy* is the driving force in promoting growth, welfare and technology development. Our life is swept up in a sea of scientific and digital innovation.

1.1 Against the "non-renewable" resources

The world energy demand, above all by non-OECD countries, has risen exponentially predicting that it will continue growing in the years ahead.
In order to satisfy the incessant electricity demand, several energy sources are exploited. The Fig. 1.1 shows the energy consumption of both non-OECD and OECD countries and the Energy Resources, in billion toe, used.

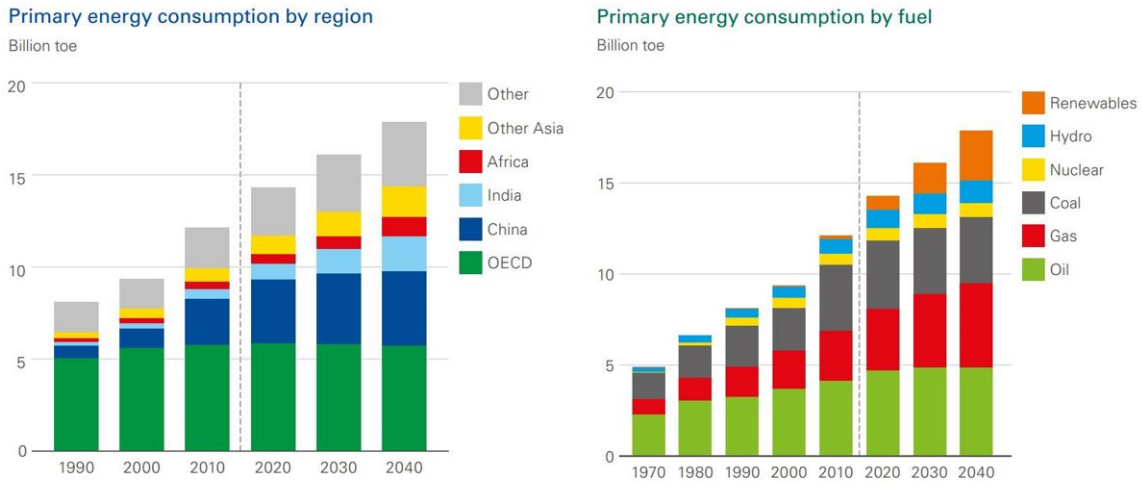

Figure 1.1: Energy Consumption by region on the left & Energy Resources on the right (*BP Energy Outlook* [1]).

In Fig. 1.1 we can note that the fossil fuels, such as Oil Gas and Coal, were and will re-

main at least up 2030/2040 the main resources for the energy production as confirmed also by the International Energy Agency (IEA). Fossil fuels are "non-renewable" because they have considerable time for creation scales of millions of years, hence not compatible with human lifespan. Today, not only the human exploits them much more quickly than they should regenerate, but also their incessant exploitation is responsible for climate change and irreversible ecological disasters.
When fossil fuels are burned to create energy emit a significant amount of carbon dioxide (CO2) in the atmosphere, increasing the global warming (Fig. 1.2), and of sulphur dioxide (SO2) producing acid rain phenomena, responsible of the atmospheric pollution that has worsened in recent years.

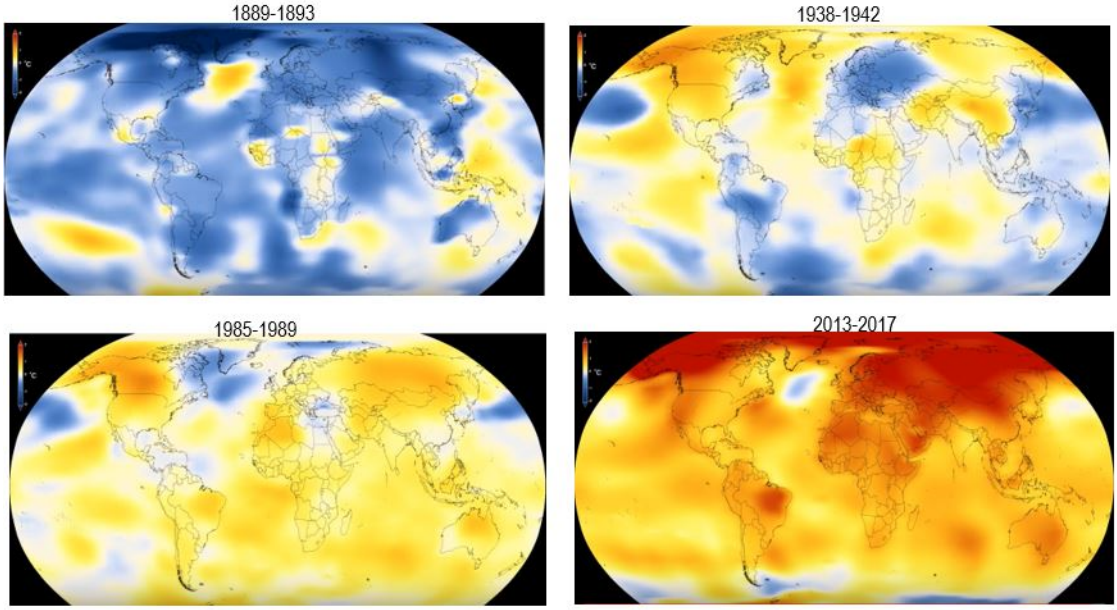

Figure 1.2: Earths global surface temperatures (*Analysis by NASA Climate Change*[2]).

In order to prevent a more critical scenario, on 16 February 2005 the *Kyoto Protocol* entered into effect as a first step against global warming. This international and legal framework commits to industrialized countries to reduce emissions of CO_2. For example Italy has ratified the protocol in 2002, instead USA, that emits more than 36% of the total emissions, has signed but not ratified the protocol. Although the global warming and the atmospheric pollution are among the most alarming problems of the modern age, it seems that a real solution is far from found because of in contrast with the profits of the major world powers. In this scenario, we report some words of the speech of Greta Thunberg, a 16-year-old climate activist, at COP24 in Katowice (Poland 2018) addressing to the worlds leaders [3]:
"*We need to keep the fossil fuels in the ground, and we need to focus on equity. And if solutions within the system are so impossible to find, maybe we should change the system itself.*"

A real solution is to invest more and more in research into renewables resources or "clean energies" such as Solar power, Wind power, Biofuel, Hydroelectric power, Tidal power and Geothermal power. These not only are regarded as infinite sources of energy because they are able to regenerate but also the use of which contribute to complies with natural resources and the environment making alongside global markets more environmentally friendly. This work, particularly, has the aim to explore the converting solar energy into electricity that is made possible thanks to the solar cell device. Differently by the others renewable energies, the ability of photovoltaic application lies in the directly conversion of the solar power into electricity rather than some intermediate form of energy.
Before investigating the study of the photovoltaic device, is necessary to give some information about the primary source used: the Sun.

1.2 Solar Spectrum

Solar cells create energy exploiting photons coming from the Sun. The amount of photons, particles of light emanating uniformly in space in all directions, changes based on the wavelengths creating the so-called Solar Spectra.
The Power distribution versus the wavelength is expressed by the Planck's law (Eq. 1.1)[4]:

$$SI = \frac{2\pi c^2 h}{\lambda^5 \left[\mathrm{e}^{(hc/kT)} - 1\right]} \tag{1.1}$$

where:

- c is the light speed $\left[\frac{\mathtt{m}}{\mathtt{s}}\right]$;
- h is the Planck's constant [$\mathtt{Js}$];
- λ is the wavelength [$\mathtt{m}$];
- k is the Boltzmann's constant $\left[\frac{\mathtt{J}}{\mathtt{K}}\right]$;
- T is the Temperature of the Sun in Kelvin [$\mathtt{K}$] .

In order to apply Eq. 1.1, let's consider the Sun as a black-body whose surface temperature is equal to $T = 5762\,\mathtt{K}$.

For a range of wavelengths from the ultraviolet section up to that infrared of the electromagnetic spectrum we can obtain the entire energy per unit of area emitted by the Sun, also known as Solar Irradiance (SI) (Fig. 1.3) and measured in $\frac{\mathtt{W}}{\mathtt{m}^2}$.

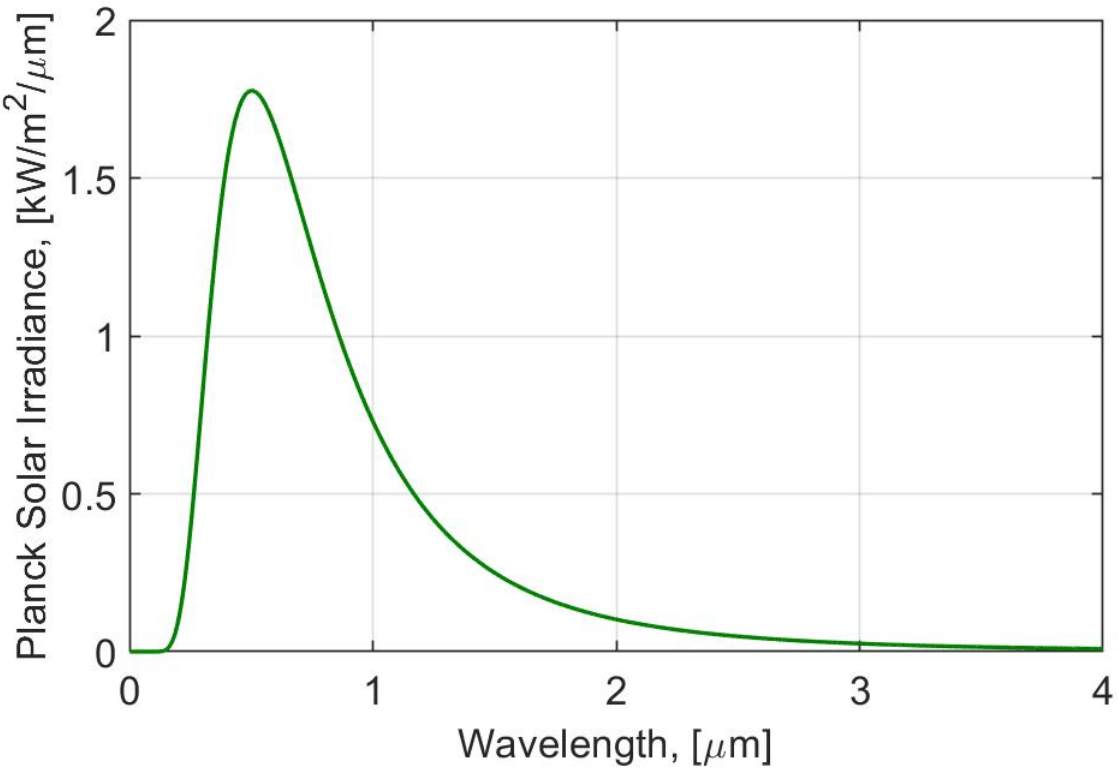

Figure 1.3: Planck Solar Irradiance.

In Fig. 1.3, we can detect that the peak of energy is around the "visible range" that covers the wavelengths for $400\,\mathtt{nm} < \lambda < 700\,\mathtt{nm}$; instead, the Solar Irradiance decreases for $\lambda < 400\,\mathtt{nm}$ in the ultraviolet section and for $\lambda > 700\,\mathtt{nm}$ in the infrared one that covers more than 50 % of the total Solar Spectra.
The Solar Irradiance shown in Fig. 1.3 is not equal to that one on the Earth's surface based on several variables such as latitude, weather conditions, day of the year and others. First, the solar radiation is partially absorbed, reflected, diffused and transmitted crossing the earth's atmosphere.

1.3 Air Mass

Respect to the SI of Fig. 1.3, the solar spectra that arrives on the earth surface is different both in its shape that in the intensity, in fact it is attenuated. These effects are linked to the thick layer of atmosphere and to the path of the light crossing it in order to reach the earth's surface. In order to quantify the reduction in the power of

the Solar Irradiance, it is necessary to introduce the **Air Mass** (AM) parameter. We know the earth revolves around itself and around the sun, but to make the concept of AM simpler, we could think to be at the Zenith and observing the displacement of the Sun, relative to this point, along an arc of an imaginary circumference.
Observing Fig. 1.4, let's assume with P_Z the position of the Sun at the Zenith point respect to the observing point; instead, with P_G a position different by the previous such as in Fig. 1.4. The angle ϑ, subtended to the imaginary arc of circumference between the points P_Z and P_G, gives us information about the shifting of the Sun [5].

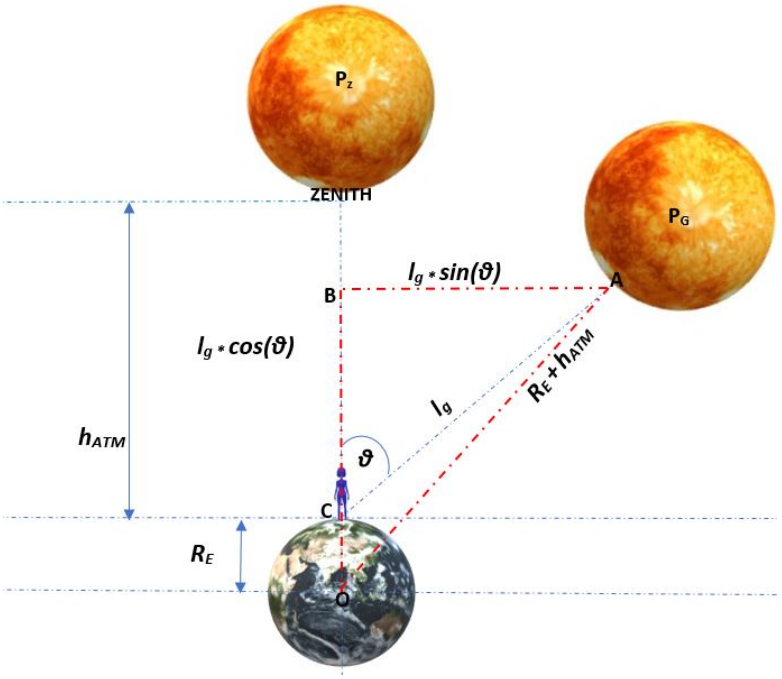

Figure 1.4: Air Mass.

From Fig. 1.4, when the Sun is in the P_G position, the photons before arriving on the Earth's surface must make a longer path. In this case, it is more likely that occur diffusion and absorption phenomena across the atmosphere.
This means that according to the ϑ angle, the Solar Irradiance is not exactly that obtained from Eq. 1.1, but is also attenuated based on the Air Mass parameter.
In order to define the AM, let's consider, from Fig. 1.4, the triangle OAB (red dashed line). By the Pythagorean theorem:

$$OA^2 = OB^2 + BA^2 \tag{1.2}$$

Replacing the terms in the previous equation with the notation adopted in Fig. 1.4:

$$(R_E + h_{ATM})^2 = (R_E + I_g\cos(\theta))^2 + (I_g\sin(\theta))^2 \tag{1.3}$$

Developing Eq. 1.3 and through some simplification we arrive to the following expres-

sion for the AM parameter:

$$AM = \sqrt{(R_E \cos(\theta))^2 + 2R_E h_{ATM} + h_{ATM}^2} - R_E \cos(\theta) \tag{1.4}$$

Eq. 1.4 can be approximated as follows:

$$AM \approx \frac{1}{\cos(\theta)} \tag{1.5}$$

The effect of the AM, computed on the basis of Eq. 1.5, on the ideal Solar Irradiance (Fig. 1.3) is shown in Fig. 1.5 where the blue line is the behavior obtained for AM=1.5 [6] corresponding to ϑ equal to 48.19°.

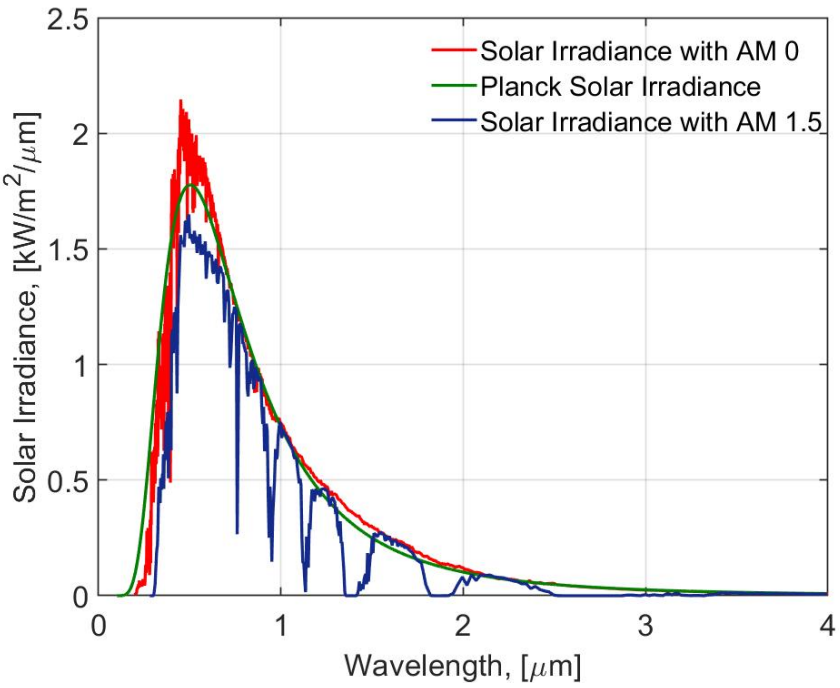

Figure 1.5: Solar Irradiance with AM0 in red line, Planck Solar Irradiation in green line and Solar Irradiance with AM1.5 in blue line.

On Fig. 1.5 is also shown the extraterrestrial radiation, the spectrum outside the atmosphere, known as AM0 [7], in general used for space applications.
We have obtained a first limitation on the ideal Solar spectra given by the attenuation caused by the atmosphere layers and by the path that the light makes arriving on the earth's surface. There are other constraints that could limit the total SI such as the atmospheric conditions. In the following sections we will assume to work in an ideal case, considering the SI spectra of Fig. 1.3.

1.4 Photovoltaic Action

The device able to convert the solar energy into electricity (the so-called photoelectric effect) is the solar cell that is the basis of the photovoltaic system.
In order to exploit the photoelectric effect [8] is necessary to use semiconductor materials characterized by a relatively low *bandgap energy* (E_g measured in eV) between the top state of the *valence band* (the lowest energy states) and the bottom one of the *conduction band* (the highest energy states) (Fig. 1.6). Commonly used semiconductors such as Ge, Si and GaAs have respectively, at room temperature, an E_g equal to 0.67 eV, 1.11 eV and 1.42 eV.
A semiconductor is able to conduct only if electrons by the valence band, acquiring energy, occupy free energy states in the conduction one.

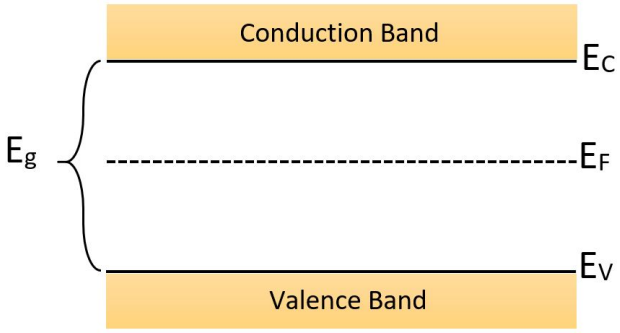

Figure 1.6: Semiconductor Band Diagram where E_c is the bottom state of the conduction band, E_v is the top state of the valence band and E_g is equal to $E_c - E_v$.

At $T = 0\,\mathrm{K}$, all electrons are in the valence band and the conduction band is empty. Instead, at room temperature, without any external excitations such as light, pressure or an electric field, electrons are thermally excited thanks to the thermal energy kT around $0.026\,\mathrm{eV}$. In this condition an appreciable number of electrons jump in the conduction band, leaving an equal number of "holes" in the valence one. If we consider a perfectly ordered and homogeneous semiconductor by a crystallographic point of view, with a small amount of impurities (*intrinsic semiconductor*), at a finite temperature, the number of electrons n is equal to the number of the generated holes p, hence $n = p = n_i$ where n_i is the intrinsic carrier density.
At the thermal equilibrium, there are continuously *generation* and *recombination* of electrons and holes. Physically, the generation corresponds to break a covalent bond in the semiconductor to free an electron that can participate in current conduction; instead the recombination is the opposite phenomena.
The problem of the electrons distribution among the electronic states is solved by the *Fermi-Dirac distribution*, according to which the Fermi level E_F has the 0.5 probability of occupation by an electron (Fig. 1.6). The details of the topic in Ref. [8].

It is necessary to underline that, at room temperature, the values of the intrinsic concentrations $[10^7 \div 10^{13}]$ $\mathtt{cm}^{-3}$ are many orders of magnitude lower than the free electrons and holes concentrations in the metal; hence, the conductivity in the intrinsic semiconductors is very low. An extremely efficient way in order to increase the free charges concentration involves the introduction of impurities (*doping*) in the crystal lattice of the material leading to two different scenarios: an addition of the negative charge carriers or positive charge carriers. Hence, the semiconductor with a high concentration of electrons/holes becomes n-type/p-type, indicating the majority carriers with n_n/p_p and the minority carriers with p_n/n_p. In the case of n-doped material the Fermi level is closer to the bottom of the conduction band. Similarly, for higher positive charge concentration, the Fermi level is closer to the top of the valence band. In both cases the semiconductor is called *extrinsic*.
First, let's consider a semiconductor at non thermal equilibrium condition with an external excitation such as light. When photons are absorbed into a semiconductor material deliver their energy to the electrons that by the valence band jump into the conduction band only if the photons energy $h\nu$ is greater than the E_g of the material considered.

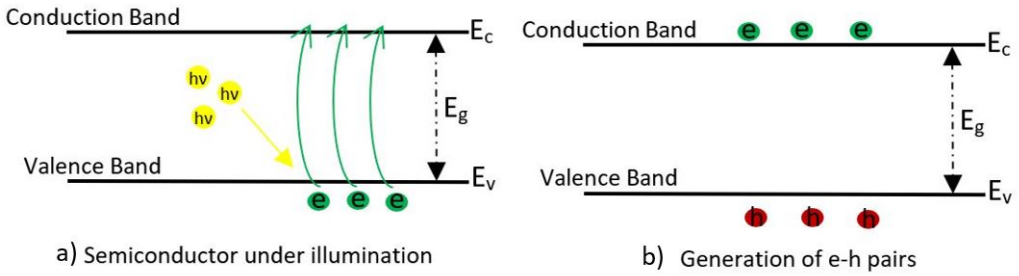

Figure 1.7: Photon energy used to excite electrons from the valence band to the conduction one.

Fig. 1.7 has the aim to show, in a simple way, the situation linked to the absorption of the photons. Considering a semiconductor connected to an external electric load, if $h\nu > E_g$ electrons *jump* in the conduction band where they are free to move and can be transported to a selective n-type metal contact. Once they deliver their excess energy to the load, return to the valence band by a selective p-type contact.
As already mentioned, the Generation mechanism is competed by the recombination one that decreases the solar power conversion because e-h pairs cannot be collected. In order to avoid this effect allowing current to flow in only one direction we have exploit the traditional p-n junction in order to provide a driving force for the spatial separation of electrons and holes.
Fig. 1.8a shows the p-n junction at thermal equilibrium without external bias. When the p-type and n-type semiconductors are jointed together is formed a *depletion region* where the mobile carrier densities are zero and the potential energy difference from

the p-side to n-side is qV_{bi}. By this, electrons majority carriers n_n and holes p_p cannot overcome the potential barrier and are confined in their regions.

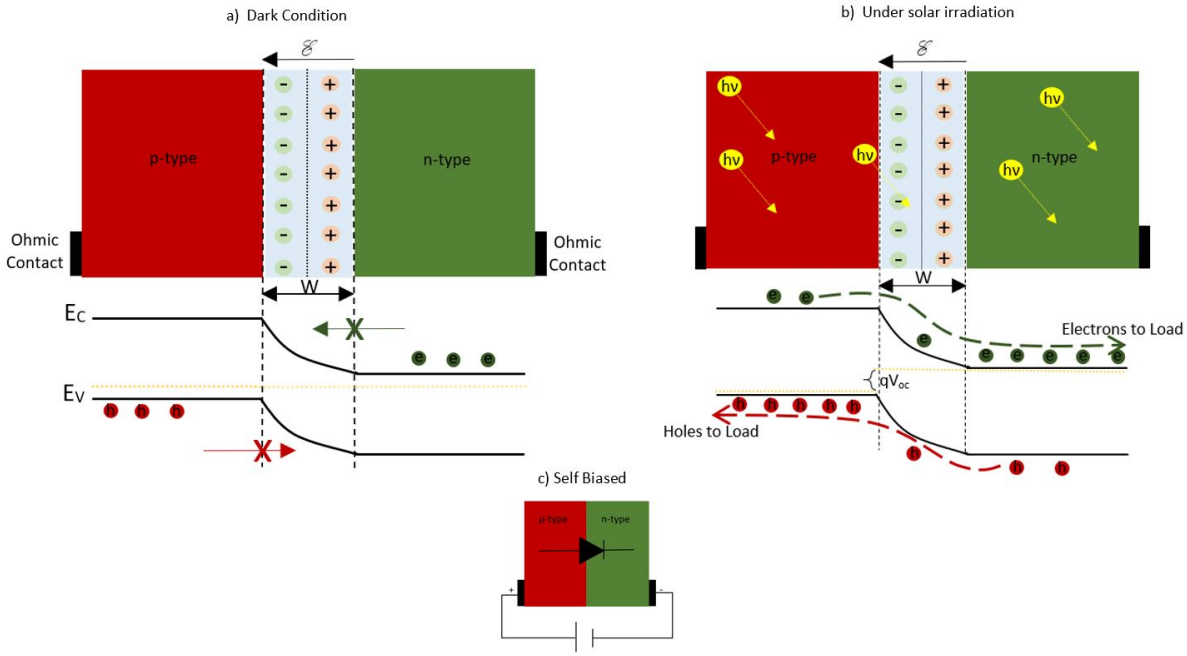

Figure 1.8: a) p-n junction under Dark Condition; b) p-n junction exposed to the solar power; c) p-n junction Self Biased.

Now, assume the p-n junction exposed under solar radiation. In Fig. 1.8b we can observe that photons are absorbed along the device generating e-h pairs. Again, electrons n_n and holes p_p cannot overcome the barrier, but the minority charges n_p(green dashed arrow) and p_n(red dashed arrow) photo-generated are able to move across the depletion region towards the n- and p-side respectively where they can be collected to the metal contacts, then delivering their energy to the load (a detailed description about the transport of carriers is in Chapter 3). By this, the p-n junction is the simplest solar cell, also called Single junction (SJ) solar cell.
When the carriers move to the load, a positive voltage is developed by the p-side contact and a negative one by the n-side. Hence, it feels like the p-n junction is self forward-biased (Fig. 1.8c) where the difference between the two quasi-Fermi levels $E_{Fn} - E_{Fp}$ is equal to qV_{oc} where V_{oc} is the open-circuit voltage. Based on the forward-biased condition, we will have a flux of carriers (*Dark current*) opposite to that photo-generated (*Photocurrent* J_{ph}) (red and green dashed arrows in Fig. 1.8). By this, the J-V characteristic of a p-n junction under illumination (red line in Fig. 1.9) is like that of a diode in forward biased (green line in Fig. 1.9) shifted along the negative J-axis of a quantity J_{ph} since the photocurrent is opposite in direction to the Dark current.

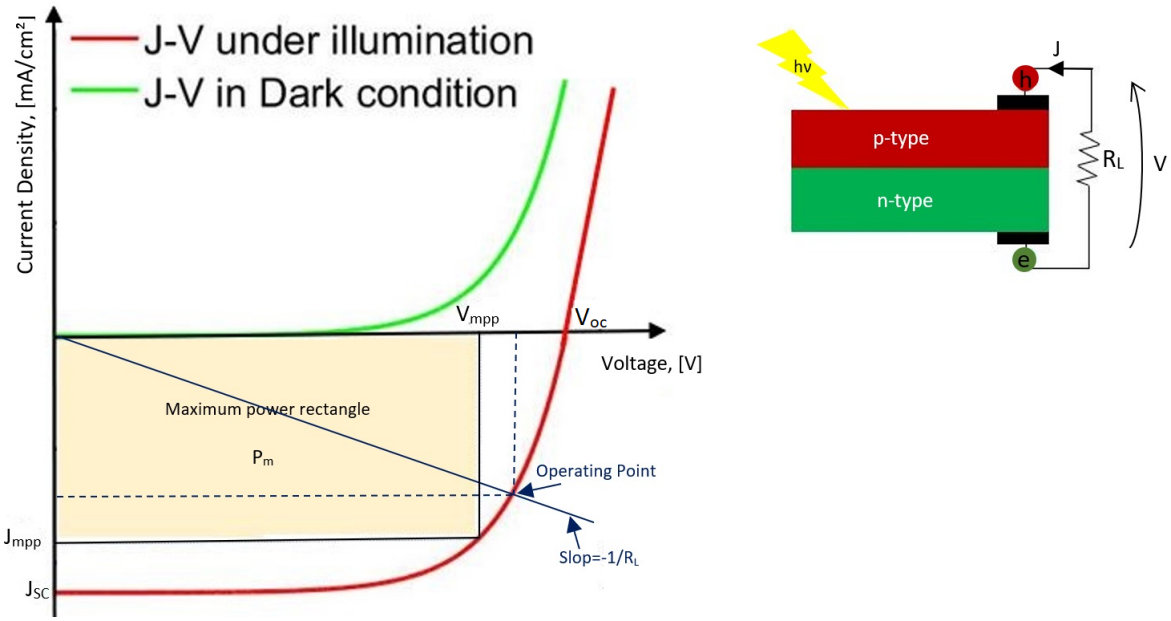

Figure 1.9: J-V characteristic in Dark condition (green line) and under illumination (red line); on the right an ideal model of a SJ solar cell.

The J-V characteristic under illumination is given from Eq. 1.6:

$$J = J_s \left(\mathrm{e}^{qV/kT} - 1\right) - J_{ph} \tag{1.6}$$

In Fig. 1.9 J_{sc} is the short-circuit current density obtained with a short-circuit between the two metal contacts ($V = 0$), and V_{oc} is the open-circuit voltage developed when the two terminals are not connected to the load ($J = 0$).
The *Operating Point*, where the load and the solar cell have the same current and voltage, is given by the intersection between the blue load line with slope $-1/R_L$ and the red J-V characteristic. Hence, it is necessary to choose a proper load in order to extract a power close to 80% of the product $V_{oc}J_{sc}$. In Fig. 1.9 we can also detect the quantities V_{mpp} and J_{mpp} that correspond to the voltage and current for the *maximum power point*. The wheat area is the maximum power rectangle equal to $P_m \triangleq V_{mpp}J_{mpp}$. Hence it is possible to define an ideal efficiency of a solar cell given by:

$$\eta = \frac{V_{mpp}J_{mpp}}{P_{in}} \tag{1.7}$$

where P_{in} is the total incident Power on the solar cell.
Another important parameter is the Fill Factor, **FF**, indicating how much the rectangle of the maximum power (in wheat in Fig. 1.9) is able to cover the rectangle ideally formed by the product $V_{oc}J_{sc}$:

$$FF = \frac{V_{mpp}J_{mpp}}{V_{oc}J_{sc}} \tag{1.8}$$

We have said that photons with $h\nu > E_g$ can create e-h pairs generating the photocurrent. If ideally we consider that for each incident photon that satisfies the previous relationship there is a e-h pair generated, we can obtain the maximum photocurrent (so-called *Cumulative photocurrent*) should be developed by a solar cell.
First, it is necessary to find the number of photons arriving on the solar cell surface. Let's define the "Solar Photon Flux" (**SPF**) the number of photons for second:

$$SPF = \frac{SI}{h\nu} \tag{1.9}$$

From Eq. 1.9 we can obtain the number of photons for each wavelength of the solar spectra. Considering an ideal material able to absorb the entire solar irradiance, the cumulative photocurrent can be defined as follows:

$$J_{ph} = q \int_{\lambda} SPF \, d\lambda \tag{1.10}$$

Fig. 1.10 shows the Cumulative photocurrent versus the wavelength.

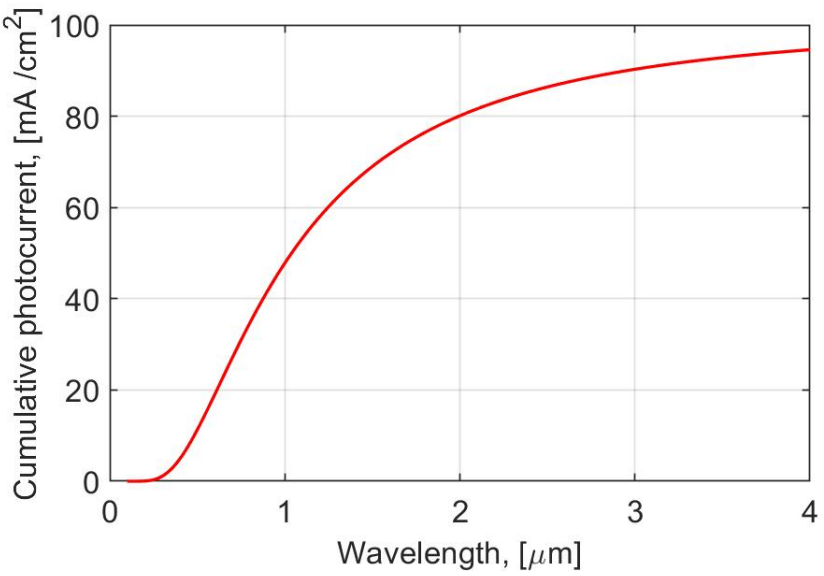

Figure 1.10: Cumulative Photocurrent J_{ph} versus λ.

In the plot, we can observe that the photocurrent increases initially because there is a peak on the "visible region" of the SI (Fig. 1.3) and then it saturates because the SI decreases in the infrared region. From this plot we can have an approximated ideal value of the maximum photocurrent that should be obtained knowing the E_g of a material.

Fig. 1.11 shows the Cumulative photocurrent versus the E_g:

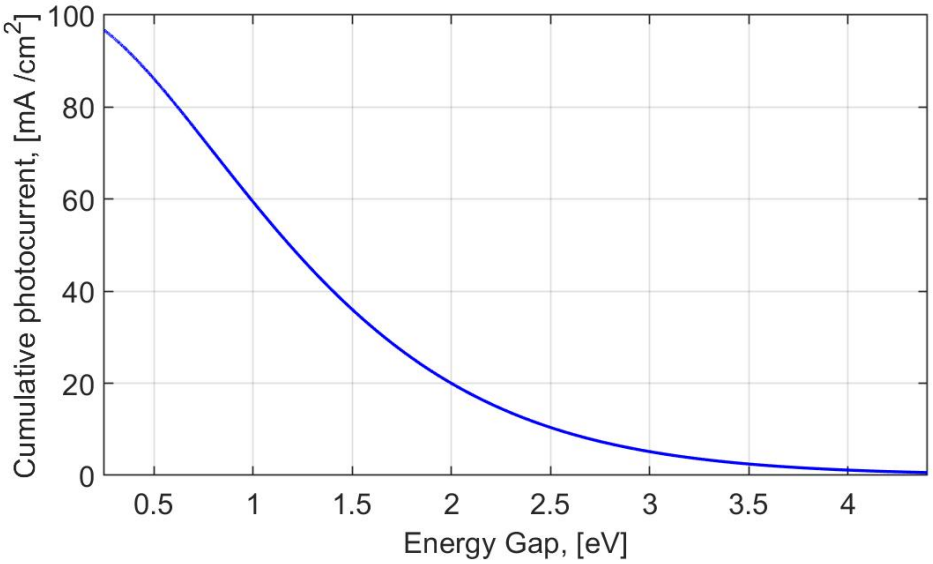

Figure 1.11: Cumulative Photocurrent J_{ph} versus E_g.

Materials with high value of E_g can have a high open circuit voltage V_{oc} but cannot reach an elevated photocurrent. In order to clarify the previous sentence, it is necessary get into a lot more details about the Optical Absorption. Fig 1.7 showed the generation of e-h pairs thanks to photons absorbed. In reality, the *jump* of the electron from the valence band to the energy state of the conduction one depends strongly by the energy of the photons.

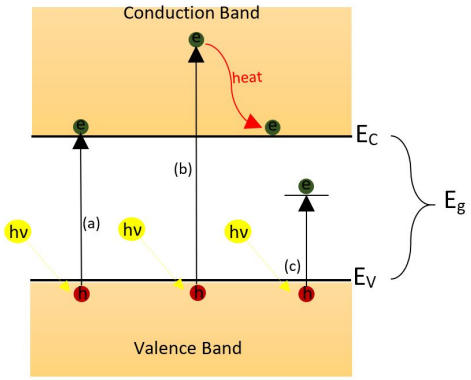

Figure 1.12: Photons absorption for (a) $h\nu = E_g$, (b) $h\nu > E_g$,(c) $h\nu < E_g$.

If $h\nu = E_g$ (Fig 1.12a) electrons jump in the bottom state of the excited states; instead, if $h\nu > E_g$ electrons initially occupy states with energy greater than E_c and then, dissipating as heat the excess energy $h\nu - E_g$, relaxing to the state with energy E_c as shown in Fig. 1.12b. For completeness, if there are chemical impurities or defects in

the lattice (Fig. 1.12c) also for $h\nu < E_g$ photons can be absorbed [8]. From Fig. 1.12, the processes *a* and *b* are called *intrinsic transitions*, instead the other is known as *extrinsic transition*. The process *b* (so-called *thermalization*) provides an upper limit to the energy of the collected electrons to the E_g of the material limiting the V_{oc} that will be proportional to the bandgap. By these considerations, it is possible deduce that the efficiency of a solar cell is limited not only by the Generation rate developing a high photocurrent only if E_g is small, but also, for the same case, by the V_{oc} that will have a small value.

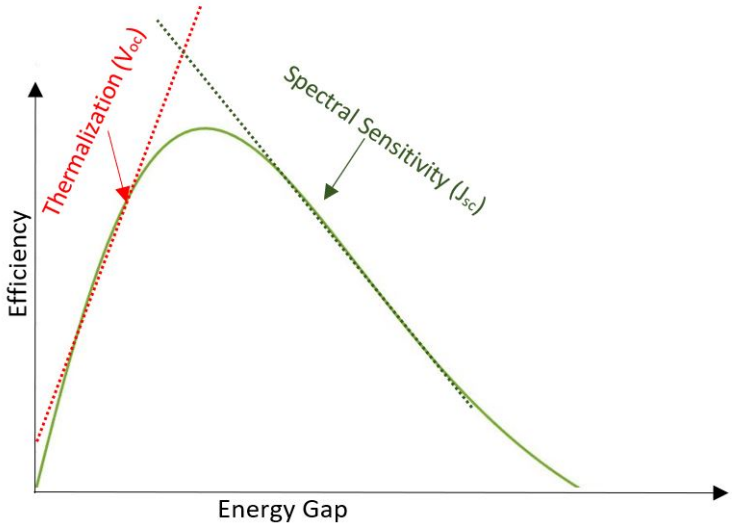

Figure 1.13: Limiting factors on efficiency of a solar cell.

By the previous considerations, we have two limitations on the efficiency:

- for a small E_g the efficiency is limited by the small V_{oc}, but the J_{ph} is high;
- for a high E_g the efficiency is limited by the small photocurrent (Fig. 1.11) given by the fact that the Generation rate decreases, alongside the V_{oc} is high.

By the first/second item we can draw the red/green dashed line in Fig. 1.13. The ideal intersection of the two lines gives us the best Efficiency versus the Energy Gap. In the same figure the green line should be a possible behavior of a solar cell efficiency. In order to obtain values of efficiency versus the E_g for a SJ solar cell, Chapter 2 will have the aim to explore this topic.
We have presented the photovoltaic action and the main parameters of a basic solar cell. In modern day, there are different kind of photovoltaic devices developed above all at the end of the 20^{th} century; a brief scenario of the photovoltaic technology will be summarized in the following section.

1.5 Photovoltaic technology

The conversion of the light, hence the photovoltaic technology can potentially become the most useful and economically tool in the future to produce electrical energy. On 1839 Alexander Edmond Becquerel discovered the photovoltaic effect. Since then, the constant technological developments paved the way to efficient and economical solar cells.

In the past, terrestrial photovoltaic applications were limited due to three important factors: low conversion efficiency, reliability and high manufacturing cost. Especially, the thrust towards better energy efficiency is given by the space race in the '60s, in order to power satellites of various types in orbit around the earth. At the end of the 20^{th} century, the ongoing research in photovoltaics and into innovative materials have led to the development of high-efficiency solar cells not only for military applications but also for terrestrial ones.

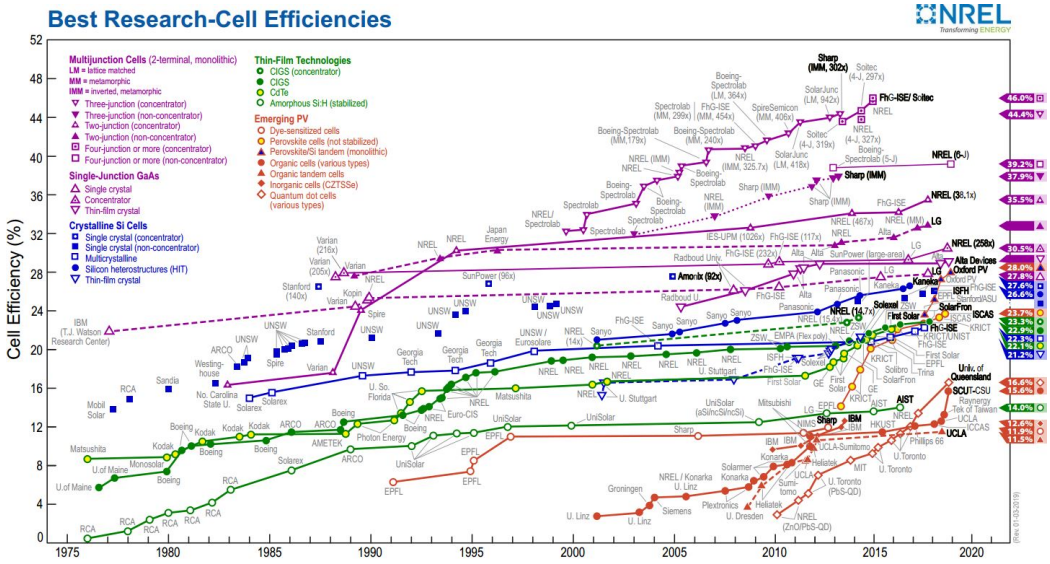

Figure 1.14: The progress of the efficiency over the years for several kinds of photovoltaic technology (*NREL Transforming ENERGY*, [9]).

In Fig. 1.14 we can observe that from 1976 to 2019 the efficiency increased for all kinds of solar cells, especially for multi-junctions (MJ) cells that are built by stacking III-V semiconductor layers on top of each other.

Two examples of Triple junctions are InGaP/GaAs/Ge cell that shows the highest performance for terrestrial applications and GaInP/GaInAs/Ge cell [10] in production for space applications, of which Fig. 1.15 shows qualitatively its structure and the exact bandgap combination. The reason of the success of this technology is linked to the fact that, today, it is possible grow excellent materials quality in a good lattice-matched structure able to harvest a wide spectral range with their bandgaps [10].

From Fig. 1.15, it is possible to detect that each material of the Triple junction solar

cell covers a different range of wavelengths thanks to a correct overlapping.

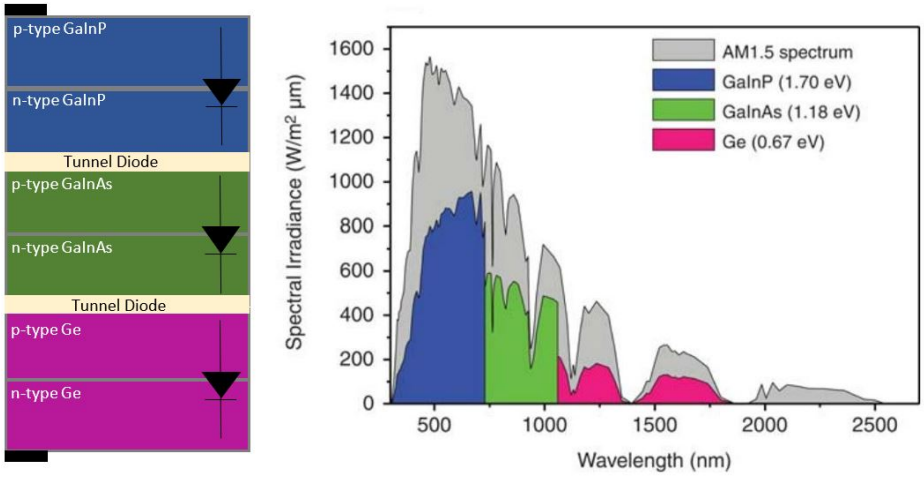

Figure 1.15: A basic structure of a GaInP/GaInAs/Ge solar cell (on the left) and the parts of the spectrum (on the right, [10]) that this kind of cell can, in theory, use.

In Fig. 1.15 the Triple junction solar cell consists of a p-n junction for each sub-cell and the interband tunnel junctions, necessary for the current flow along the device, results in an addition of the number of layers, hence to a more complex structure. However, for high-efficiency, the MJ solar cell plays a leading role and shows up the most promising photovoltaic technologies for the future although many challenges about the structure device and the optimal use of each material, must be achieved.
Today, the aim is focused on further improving the attainable efficiency by increasing the number of junctions towards 4/5 and alongside finding solutions to many structural problems that not only rise the device complexity but also the manufacturing costs.

1.6 Thesis Setting Goals

Based on the fact that the design and practical realization of MJ solar cells is not an easy task due to the constraint on current matching and the need of tunnel junctions, is necessary to achieve a simpler structure. In this scenario, a paper on a new kind of solar cell characterized by a multi-terminal bipolar junction transistor (BJT) structure has been recently published by A. Marti and A. Luque [11]. They were strong-minded about the calculation of the efficiency limit by using the Shokley and Queisser [12] discovering that is necessary review the fundamental constraints of a common bipolar structure in order to obtain the same efficiency of a double junction solar cell. Being motivated by the fact that a heterostructure bipolar transistor, potentially usable as solar energy absorbers, could obtain the same efficiency of a dual-junction cell, the aim of the thesis is to explore it by a more realistic model.
In order to do that Chapter 2 focuses in the exposition of the Shokley-Queisser detailed

balance model for a single junction (SJ) solar cell, then extended also to the DJ case allowing to calculate the efficiency as a function of the top and bottom bandgaps.
Chapter 3 provides some information about the Reflectance and Absorption Coefficient for GaAs and $Al_{0.4}Ga_{0.6}As$ semiconductors, showing also a mobility model [13] applicable to the simulations conducted. Then, the analytical drift-diffusion equations (so-called Hovel model, [14]) are derived and implemented for a homo-junction *p-n* GaAs solar cell, for a *n-p* $Al_{0.4}Ga_{0.6}As$ solar cell and for a *p-n* $Al_{0.4}Ga_{0.6}As$/GaAs hetero-junction solar cell. For each of them, simulations were carried out in order to study their properties including but not limited to: diffusion current of the minority charges along the device and spectral response.
In Chapter 4, after a summary of the most important features of a common BJT, the Hovel model is extended to an HBJT structure with emitter and base in $Al_{0.4}Ga_{0.6}As$ and collector in GaAs. First of all, simulations are carried out for a HBJT with traditional structural parameters discovering that the photocurrent would be very small. Hence, in order to increase the photocurrent several structural changes are done such as increasing the base dimensions and doping levels. By this, the simulations show that the photocurrents behavior seek to that of the *n-p* $Al_{0.4}Ga_{0.6}As$ homojunction solar cell and that *p-n* $Al_{0.4}Ga_{0.6}As$/GaAs heterojunction confirming a good efficiency.
This is an important result because the structure is simple avoiding a significant number of layers required, as just said, in DJ solar cell in order to solve the current matching constraints. Based on the rudimentary simulations carried out in the thesis, an HBJT structure could be used as building block for MJ solar cells, decreasing the number of junctions. In this context, further research is necessary in order to solve many practical challenges on the design and technological levels, such as the necessity to extract additional contacts to connect the sub cells independently.

CHAPTER 2

Detailed Balance Models

2.1 Theoretical efficiency limit for a SJ solar cell

In the previous section, Eq. 1.7 defines the efficiency of a solar cell. In order to calculate exactly the V_{oc} and J_{sc} several physical factors intrinsic/extrinsic to the device should be considered (Chapter 3). When a solar cell is exposed to the solar irradiance, the photons with $h\nu > E_g$ absorbed by the semiconductor material generate e-h pairs (Fig. 1.12).
The reverse process of the Generation is the Recombination process such that an electron and hole recombine resulting in a release of energy. The Recombination process [8] can be of two types:

- Radiative recombination given by electrons that make a transition from the Conduction Band to the Valence Band giving off photons of energy equal to the E_g of the semiconductor material; if the transition between the two bands is done without any external stimulus the recombination is *spontaneous*, otherwise the recombination is called *stimulated*.

- Non Radiative recombination for which the recombination e-h leads not to photons emission but the energy in excess is converted to vibrational energy of lattice atoms generating heat.

In 1961, Shokley and Queisser proposed the "Detailed Balance Limit of Efficiency" [12] for a Single Junction solar cell considering the radiative recombination a fixed fraction of the total recombination phenomena. Following, we will discuss this kind of model in order to obtain a quantitative plot about the efficiency of a solar cell versus its E_g respect to that obtained in Fig. 1.13.

2.1.1 Ultimate Efficiency

First, supposed to have a circular solar cell, at a temperature of $T_c = 0\,\mathrm{K}$, surrounded by a blackbody which temperature is $T_s = 6000\,\mathrm{K}$ (Fig. 2.1).

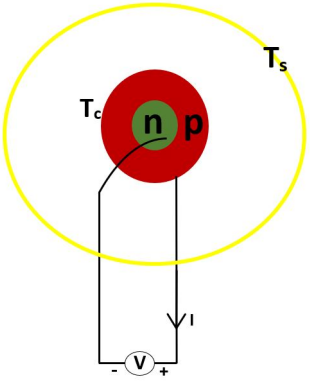

Figure 2.1: Idealized solar cell model: a solar cell maintained at temperature of $T_c = 0\,\mathrm{K}$ surrounded by a black-body (Sun) at temperature of $T_c = 6000\,\mathrm{K}$.

Eq. 1.7 can be rewritten as follows:

$$\eta = \frac{P_{out}}{P_{inc}} \tag{2.1}$$

where P_{out} is the Output Power produced by the solar cell, instead P_{inc} is the Input Power generated by the solar irradiance.
First, in order to find P_{inc} let's consider again the Planck's formulation, now in function of the frequency ν.
Eq. 1.1 in function of λ can be rewritten in function of ν as follows:

$$SI = \frac{2\pi\nu^3 h}{c^2\left[\mathrm{e}^{(h\nu/kT)} - 1\right]} \tag{2.2}$$

By Planck's law, as just done in the Section 2.1, we can calculate the incident Power (P_{inc}) generated by a black-body.
Considering a Solar Cell as in Fig. 2.1, circular in shape, that is able to absorb the blackbody radiation (Sun) without losses due to geometric factors, so we obtain:

$$P_{inc} = A\int_0^\infty SI\, d\nu \tag{2.3}$$

where A is the area subject to the solar radiation.

In order to find out P_{out}, it is necessary to consider that:

- Photons's absorption is modeled by a "*step-function*": the material absorbs the incident photons only if $h\nu > E_g$;
- Each photon absorbed generates a charge q at a voltage of $V_g = h\left(\frac{\nu_g}{q}\right)$;
- Temperature of the cell $T_C = 0\,\mathtt{K}$;
- Circular geometry of the solar cell.

The hypothesis $T_C = 0\,\mathtt{K}$ has an important consequence in order to obtain P_{out}. In fact, we know that if a material is at temperature $T_C > 0\,\mathtt{K}$ the atoms thermal excitement can break some bonds. By the energetic point of view, this means that some electrons jump from the valence band to conduction band increasing the semiconductor conductivity. Instead, $T_C = 0\,\mathtt{K}$ means that none electron jumps from the conduction to valence band unless the material is exposed to the solar irradiance. If we assume that the solar cell is maintained to the $T_C = 0\,\mathtt{K}$ by an external means during the exposure to the solar irradiation we have that the amount of e-h pairs generated are in number equal to the absorbed photons. As done in Section 1.4, we are able to calculate the number of photons (SPF) arriving in the solar cell surface (Eq. 1.9) considering now the SI of Eq. 2.2 arriving to the following expression for the P_{out}:

$$P_{out} = Ah\nu_g \int_{\nu_g}^{\infty} SPF\, d\nu \tag{2.4}$$

where $h\nu_g$ is the energy developed by the each electron promoted from the valence to the conduction band.
We have both P_{in} and P_{out}, hence it is possible to obtain the expression for the efficiency η. In particular, the efficiency found is called "Ultimate Efficiency" $u(\nu_g)$.

$$u(\nu_g) = \nu_g \frac{\displaystyle\int_{\nu_g}^{\infty} \nu^2 \left(\mathrm{e}^{\left(\frac{h\nu}{kT}\right)} - 1\right)^{-1} d\nu}{\displaystyle\int_{0}^{\infty} \nu^3 \left(\mathrm{e}^{\left(\frac{h\nu}{kT}\right)} - 1\right)^{-1} d\nu} \tag{2.5}$$

2.1.2 Nominal Efficiency

Let's consider a more realistic case (Fig. 2.2):

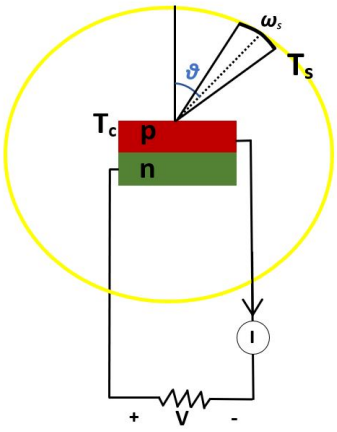

Figure 2.2: Planar solar cell at temperature of $T_c = 300\,\mathrm{K}$ exposed to a spherical blackbody.

where:

- the solar cell has a planar structure;
- the temperature of the cell is $T_c = 300\,\mathrm{K}$;
- the cell is surrounded by a blackbody at its own temperature ($T_s = 300\,\mathrm{K}$).

In this scenario, where the solar cell is at thermal equilibrium with the surrounding environment because they are at the same temperature, all the energy that the cell receives will be divested again to the environment. The solar cell transfers energy to the environment in the form of Radiative recombination. At equilibrium, such as in this case, the rate of recombination with resultant radiation phenomena is exactly equal to the rate of Generation, so the blackbody radiation from the cell can be expressed with F_{c0}:

$$F_{co} = 2A_p\, t_c\, Q_c \tag{2.6}$$

where Q_c is equal to the number of photons absorbed in the solar cell, considering the temperature of $T_c = 300\,\mathrm{K}$. The parameter t_c is equal to the probability that a photon with $h\nu > E_g$ will produce an h-e pair and $2A_p$ is the area of the flat plate of the cell where the black-body radiation comes out.
Under thermal equilibrium condition the **mass action law** holds:

$$np = n_i^2 \tag{2.7}$$

where n is the electron density in the conduction band, p is the hole density in the valence band and n_i^2 is the intrinsic carrier density.
The case described was at thermal equilibrium. In a real case, the environment's temperature is $T_s \approxeq 6000$ K, instead the cell's temperature is $T_c \approxeq 300$ K. If we consider the real case for $T_s \approxeq 6000$ K and $T_c \approxeq 300$ K we move to a situation where there is not thermal equilibrium; hence the Generation rate is different from the Recombination rate and Eq. 2.7 is not valid leading to $np > n_i^2$. In this new scenario, we can redefine the radiative recombination rate in the following way:

$$F_c = F_{co}\left(\frac{np}{n_i^2}\right) = F_{co}\mathrm{e}^{(V/V_c)} \tag{2.8}$$

where:

- V is the voltage difference between the terminals connected to the n and p regions of the solar cell;
- V_c stands for $\dfrac{kT_c}{q}$.

Let's consider also the generation rate F_s of h-e pairs by the incident solar radiation:

$$F_s = Af_\omega t_s Q_s; \tag{2.9}$$

where t_s is the probability that incident photons produce e-h pairs. This parameter is different from the previous t_c based on the difference in the spectral distribution of the black-body radiation given by the two different temperatures T_s and T_c. The parameter f_ω is a geometrical factor function of the solid angle ω_s subtended by the sun (Fig. 2.2), so that:

$$f_\omega = \frac{\omega_s}{\pi} = 2.18\,\mathrm{x}\,10^{-5} \tag{2.10}$$

Actually we have obtained the Generation rate F_s and the radiative recombination rate F_c; in order to carry out the calculation and obtaining the final nominal efficiency, it is necessary to consider also the following three processes:

- $R(V)$: non radiative recombination of e-h pairs;
- $R(0)$: non radiative generation processes;
- the removal of holes and electrons from p and n regions at a rate of $\dfrac{I}{q}$.

By the steady state condition the sum of the listed processes is equal to zero, so that:

$$F_s - F_c(V) + R(0) - R(V) - \frac{I}{q} = 0 \tag{2.11}$$

Eq. 2.11 can be rewritten as follows:

$$F_s - F_{c0} + [F_{c0} - F_c(V) + R(0) - R(V)] - \frac{I}{q} = 0 \tag{2.12}$$

In order to relate the radiative and non radiative rate it is possible to introduce a new parameter f_c :

$$F_{c0} - F_c(V) = f_c \left[F_{c0} - F_c(V) + R(0) - R(V)\right] \tag{2.13}$$

By a simple case of a germanium p-n junctions, it is possible to write:

$$R(V) = R(0)\mathrm{e}^{(V/V_c)}; \tag{2.14}$$

Considering Eq. 2.8, Eq. 2.13, and Eq. 2.14 we obtain:

$$f_c = \frac{F_{c0}}{F_{c0} + R(0)}; \tag{2.15}$$

The term f_c is independent by the voltage and in the case of $F_{c0} \gg R(0)$ we should obtain $f_c \approxeq 1$ leading to non-radiative losses and a greater efficiency.
For a general model, considering $f_c \neq 1$, by the general diode equation (providing power):

$$I = I_0 \left[1 - \mathrm{e}^{(V/V_c)}\right] \tag{2.16}$$

where $I_0 = q[F_{c0} + R(0)]$.

Let's replace Eq. 2.12, Eq. 2.14 and Eq. 2.15 into Eq. 2.8, so that:

$$I = q(F_s - F_{c0}) + q\frac{F_{c0}}{f_c}\left[1 - \mathrm{e}^{(V/V_c)}\right]; \tag{2.17}$$

Eq. 2.19 has the shape of Eq. 1.6 with:

$$I_{sc} = q(F_s - F_{c0}); \tag{2.18}$$

Considering that $T_s > T_c$, it is possible to deduce that $F_s >> F_{c0}$ leading to $I_{sc} \approxeq qF_s$. Hence Eq. 2.19 becomes:

$$I = qF_s + q\frac{F_{c0}}{f_c}\left[1 - \mathrm{e}^{(V/V_c)}\right] \tag{2.19}$$

In order to find the open circuit voltage V_{oc}, it is necessary to force $I = 0$ in Eq. 2.19, so that:

$$V_{oc} = V_c \left[\ln \left(\frac{I_{sc}}{I_0} \right) + 1 \right]; \tag{2.20}$$

As made for I_{sc}, neglecting F_{c0} with respect to the term F_s, with some simplifications we can obtain:

$$V_{oc} = V_c \ln \left(f \frac{Q_s}{Q_c} \right); \tag{2.21}$$

where $f = \dfrac{f_c f_\omega t s}{2 t_c}$.

From Eq. 2.1, the nominal efficiency η in terms I_{sc} and V_{oc} results as:

$$\eta_n = \frac{P_{out}}{P_{inc}} = \frac{V_{oc} I_{sc}}{P_{inc}} = \frac{V_{oc}}{V_g} u(\nu_g) t_s \tag{2.22}$$

Eq. 2.22 is able to provide an upper theoretical limit for a Single Junction solar cell, hence Fig. 2.3 shows the nominal efficiency η_n for a SJ solar cell at temperature $T_c = 300\,\mathrm{K}$ exposed to the blackbody radiation at $T_s = 6000\,\mathrm{K}$.

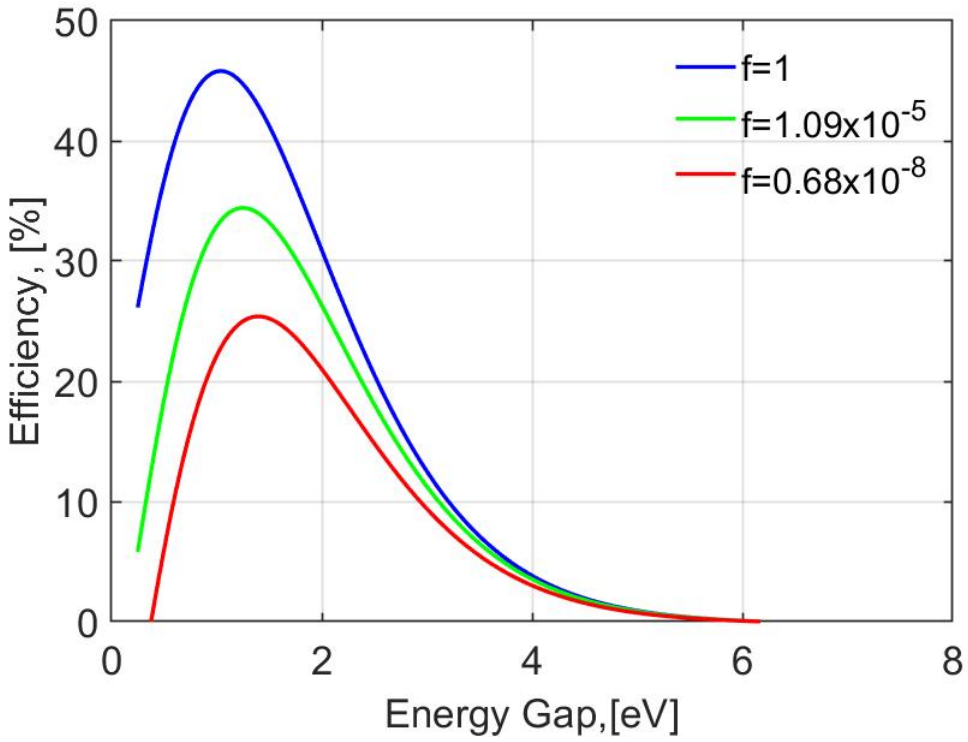

Figure 2.3: nominal efficiency limit based on S-Q Detailed Balance model.

From Fig. 2.3, the nominal efficiency limit for $f = 1$ (blue line) is similar to that we could get from the "ultimate efficiency" with an upper limit around 45% for an Energy Gap of 1.03 eV.
The efficiency decreases taking into account geometrical losses and non radiative recombination (green and red line). In Fig. 2.3, the green curve is the *detailed balance limit of nominal efficiency* based on: a perfectly absorbing cell with $t_s = t_c \equiv 1$, a normal incidence $f_\omega = 2.18\text{x}10^{-5}$ and a non-radiative recombination $f_c = 1$ (data from [12]). This approaches 34% of efficiency for an E_g of 1.2 eV. Furthermore, in the same figure, the red curve is obtained for $f_\omega = 1.36\text{x}10^{-5}$, $f_c = 10^{-3}$ and $t_s = t_c = 0.9$, leading to a less efficiency (data from [12]).
Hence, the maximum limit that a SJ solar cell can approach is first of all function of its Energy Gap, also depend by several geometrical and basic degrading factors. The last step is finding the maximum efficiency.

2.1.3 Detailed Balance Limit of Efficiency

In order to obtain the *Detailed balance limit* of efficiency it is necessary to compute the maximum power output and then replacing it into Eq. 1.7. The maximum power occurs by choosing the voltage V so that the product IV is a maximum. Analytically, P_m can be obtained as follows:

$$\frac{d(IV)}{dV} = 0 \tag{2.23}$$

where I is given from Eq. 2.19.
From Eq. 2.23 we are able to obtain I_{mpp} and V_{mpp} (Fig. 1.9). V_{mpp} is always smaller than the open-circuit voltage V_{oc}. By that, the maximum power output from solar cell is smaller than that obtained from the product $V_{oc}I_{sc}$ (Eq. 2.3).
Considering the expression

$$\eta = \frac{I_{mpp}V_{mpp}}{P_{inc}} \tag{2.24}$$

we will find that the *detailed balance limit* will be a little smaller than that *nominal* in the same conditions ($t_s = t_c \equiv 1$, $f_\omega = 2.18\text{x}10^{-5}$ and $f_c = 1$). Fig. 2.4 shows the nominal efficiency η_n in green line (the same of Fig. 2.3) and η, *detailed balance limit* one.
Light blue curve, in Fig. 2.4, confirms that the upper limit of efficiency, around 30 % for an Energy Gap of 1.25 eV is smaller than that obtained in Fig. 2.3.
The result obtained is very important because give us an idea on the upper limit that a SJ solar cell can obtain versus the E_g of the material semiconductor.

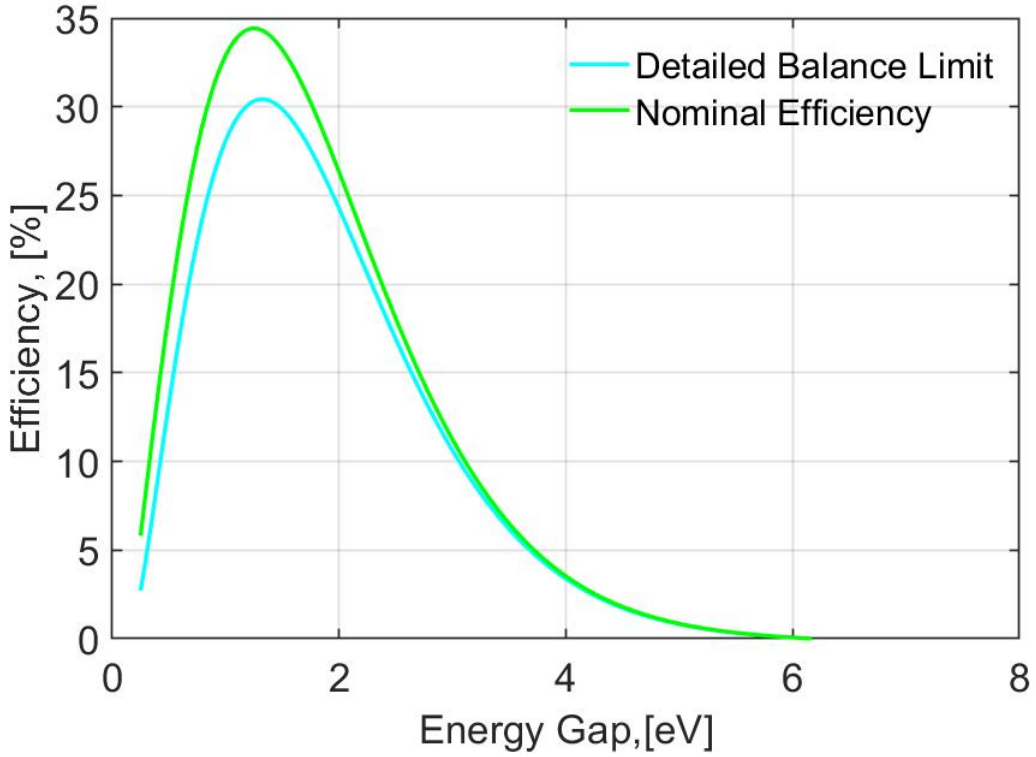

Figure 2.4: nominal efficiency (green curve) and detailed balance limit of efficiency (light blue curve) versus E_g for $t_s = t_c \equiv 1$, $f_\omega = 2.18\text{x}10^{-5}$ and $f_c = 1$.

In Chapter 3, we will see that there are many physical constraints linked to both external and internal factors to the solar cell device that lead to decrease the efficiency. The only way to increase the efficiency is to satisfy, remembering also the considerations done in Sec. 1.4, two opposite requirements:

- high energy gap materials in order to have a significant V_{oc};
- low energy gap materials in order to increase J_{ph}.

These items can be present at the same time in a kind of structure different by that assumed by Shockley and Queisser. In fact, the efficiency can be increased using multiple materials in Double-Junction (DJ) solar cell or Multi-junction solar cell where semiconductors with different bandgap energies can be fabricated in a single piece or fabricated separately and then brought together [10].

2.2 Theoretical efficiency limit for a DJ solar cell

A good way in order to increase the efficiency of a solar cell is creating a structure with different materials, each of which is characterized by its E_g. The aim of this Section is to exploit the characteristic of a DJ solar cell in order to find a simple model that can represent it.
First, in a double junction solar cell the absorption of the blackbody irradiance is done by two different materials (M_1 and M_2): suppose M_1 with Energy Gap E_{g1} and M_2 with the Energy Gap E_{g2} such that $E_{g1} > E_{g2}$.
The main problem is understand how to place the two materials. Let's observe the following cases:

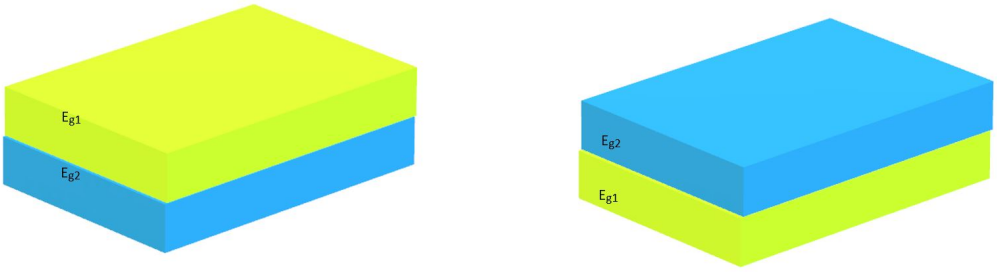

Figure 2.5: **case a** on the left, **case b** on the right

In Fig. 2.5, the **case a** shows an idealized DJ solar cell where the material with the highest E_g is placed above the other; instead the **case b** shows the opposite case. Choosing the **case a** or the **case b** has an important consequence on the absorption of the solar irradiance.
In fact, from Eq. 2.25

$$E_g = h\nu = h\frac{c}{\lambda} \tag{2.25}$$

we can deduce that if $E_{g1} > E_{g2}$ then $\lambda_1 < \lambda_2$. The material with E_{g1} absorbs the region of the spectrum for which it occurs $\lambda < \lambda_1$, instead the material with E_{g2} absorbs up to $\lambda < \lambda_2$. Hence, considering the solar irradiance (Fig. 1.3), we are able to detect the wavelengths absorbed by the two materials.
Based on the previous considerations, the **case a** and the **case b** lead to two different situations showed in Fig. 2.7 and in Fig. 2.6.
Let's consider the **case b** where the material M_2, with the smallest E_g, is on the top of the stack. Considering that $\lambda_1 < \lambda_2$ the material M_1, placed on the bottom, cannot absorb the solar spectrum because the material M_2 will absorb the spectrum in the range of $\lambda < \lambda_2$ (Fig.12), reducing a DJ solar cell to the case of a SJ one.
By this we can conclude that the **case b** is not useful.

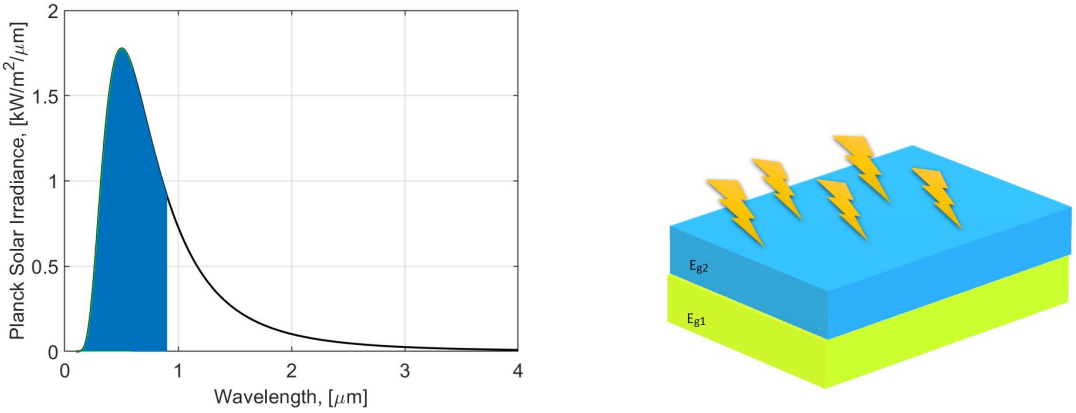

Figure 2.6: **case b**: the material M_2 absorbs the solar spectrum for $\lambda < \lambda_2$ (blue area); the material M_2, placed on the bottom side, cannot absorb the blackbody radiation.

Let's explore the **case a**.
In this situation, the material M_1, placed on the top of the stack, can absorb the part of the spectrum for $\lambda < \lambda_1$. The remaining part is absorbed by the material M_2 that is able to absorb up to λ_2 (Fig. 2.7). We can conclude that the **case a** is useful.

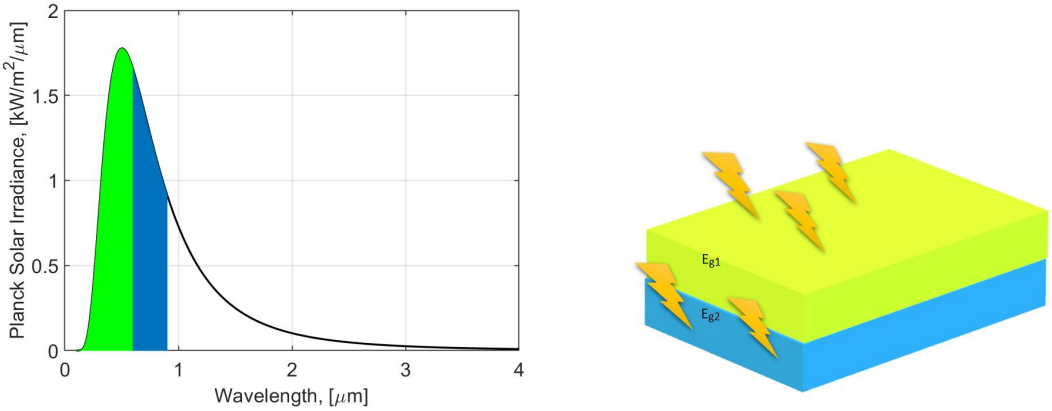

Figure 2.7: **case a**: the material M_1 absorbs the solar spectrum for $\lambda < \lambda_1$ (green area); the material M_2, placed on the bottom side, absorbs the blackbody radiation for$\lambda_1 < \lambda < \lambda_2$ (blue area).

By this discussion, a DJ solar cell consists of two different materials such that the semiconductor with the highest E_g is placed on the top of the stack.
In order to collect holes and electrons it is necessary to dope the materials as discussed in the SJ case. Ideally, a DJ solar cell is formed by a stack of two SJ solar cells (p-n/p-n). About this structure we should understand if the efficiency is greater than that of a SJ one. If a SJ solar cell can be represented by a diode, for a DJ we can consider a system with two diode in series.

From Fig. 2.8,

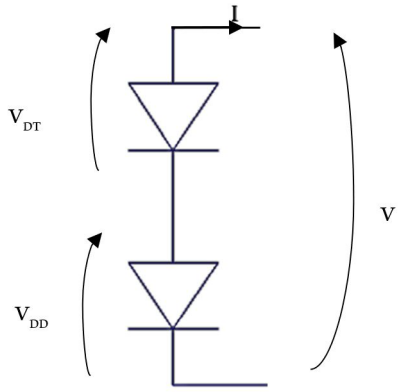

Figure 2.8: Ideal circuit model of a Double Junction solar cell.

we have the following notation:

- I_{DT} is the current in the Top diode;
- I_{DD} is the current in the Bottom diode;
- V_{DT} is the voltage in the Top diode;
- V_{DD} is the voltage in the Bottom diode.

The current on the Top diode, consistent to Eq. 2.19, is:

$$I_{DT} = I_{SHT} + I_{DT}\left[1 - \mathrm{e}^{(V_{DT}/V_C)}\right] \tag{2.26}$$

The current in the Bottom diode is

$$I_{DD} = I_{SHD} + I_{DD}\left[1 - \mathrm{e}^{(V_{DD}/V_C)}\right] \tag{2.27}$$

The Voltage at the terminals is:

$$V = V_{DT} + V_{DD} \tag{2.28}$$

First of all, it is necessary to find the short-circuit current I_{CC}. Let's put $V = 0$ and from the circuit model (Fig. 2.8) we get $I_{DT} = I_{DD} = I_{CC}$. Hence, Eq. 2.26 and Eq. 2.27 yield to :

$$I_{SHT} + I_{DT}\left[1 - \mathrm{e}^{(V_{DT}/V_C)}\right] = I_{SHD} + I_{DD}\left[1 - \mathrm{e}^{(V_{DD}/V_C)}\right]$$

From V=0, it results $V_{DT} = -V_{DD}$:

$$I_{SHT} + I_{DT} - I_{DT}\,\mathrm{e}^{-(V_{DD}/V_C)} = I_{SHD} + I_{DD} - I_{DD}\,\mathrm{e}^{(V_{DD}/V_C)}$$

Substituting $y = \mathrm{e}^{(V_{DD}/V_C)}$ in the previous we obtain:

$$I_{DD}\, y^2 + (I_{SHT} + I_{DT} - I_{SHD} - I_{DD})y - I_{DT} = 0 \tag{2.29}$$

Renaming:

- $a = I_{DD}$
- $b = I_{SHT} + I_{DT} - I_{SHD} - I_{DD}$
- $c = -I_{DT}$

Solving Eq. 2.29 through $y = \dfrac{-b \pm \sqrt{b^2 - 4ac}}{2a}$ we should obtain two solutions; picking up that one for $y > 0$ it is possible to obtain V_{DD} by the previous relation:

$$V_{DD} = V_C \ln(y) \tag{2.30}$$

By this, it is possible obtain the short-circuit current:

$$I_{CC} = I_{SHD} + I_{DD}\left(1 - \mathrm{e}^{(V_{DD}/V_C)}\right) \tag{2.31}$$

The short-circuit current I_{CC} will be the minimum between I_{SHD} and I_{SHT}.
Now, let's put $I = 0$ in order to obtain the open-circuit voltage V_{oc}. Eq. 2.26 and Eq. 2.27, for $I_{DT} = I_{DD} = 0$, yield to:

$$I_{SHT} + I_{DT}\left[1 - \mathrm{e}^{(V_{DT}/V_C)}\right] = 0 \tag{2.32}$$

$$I_{SHD} + I_{DD}\left[1 - \mathrm{e}^{(V_{DD}/V_C)}\right] = 0 \tag{2.33}$$

From Eq. 2.32 and Eq. 2.33, it is possible to obtain V_{DT} and V_{DD} respectively.
Considering that $V_{oc} = V_{DT} + V_{DD}$, the open-circuit voltage will be:

$$V_{oc} = V_C \ln\left(\frac{I_{SHT}}{I_{DT}} + 1\right) + V_C \ln\left(\frac{I_{SHD}}{I_{DD}} + 1\right) \tag{2.34}$$

Now, we have both V_{oc} and I_{cc}. By applying the S-Q model to the top SJ solar cell and to the bottom one, using Eq. 2.34 and Eq. 2.31 into Eq. 2.22 we are able to obtain the nominal efficiency η_n for the DJ solar cell.
Fig. 2.9 shows the nominal efficiency η_n as a function of the E_g of the top and the bottom materials.
The upper limit is around 44% for a Top gap equal to 1.6 and bottom gap equal to 0.71. Also for Top gap equal to 1.8 and bottom gap equal to 0.93 the nominal efficiency

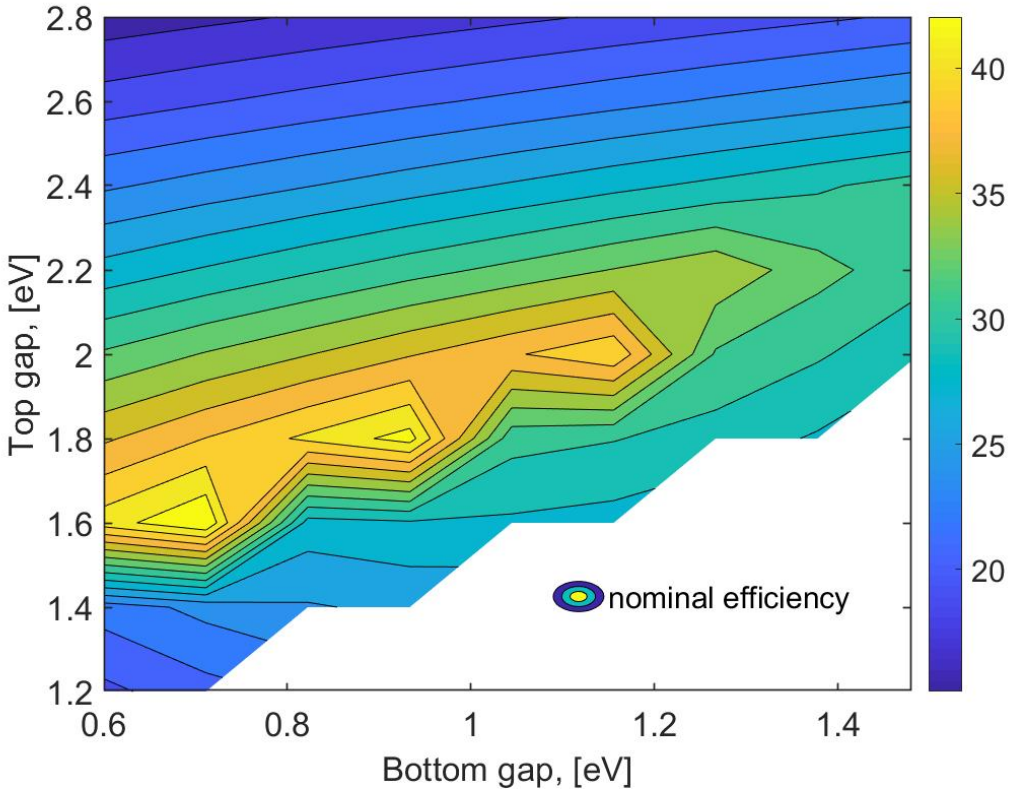

Figure 2.9: Nominal efficiency as a function of the bottom gap and top gap, considering detailed balance parameters: $f = 1.09 \text{ x } 10^{-5}$, $f_\omega = 2.18 \text{ x } 10^{-5}$, $f_c = 1$ and $t_s = t_c = 1$.

has a high value around 43 %.
In order to find a simple mathematical expression for the I-V characteristic, let's consider the explicit expression of V as a function of I.
Hence, Eq. 2.26 yields to:

$$V_{DT}(I) = V_C \ln\left(\frac{I_{SHT} - I}{I_{DT}} + 1\right) \tag{2.35}$$

and from Eq. 2.27:

$$V_{DD}(I) = V_C \ln\left(\frac{I_{SHD} - I}{I_{DD}} + 1\right) \tag{2.36}$$

By the relation $V = V_{DT} + V_{DD}$:

$$V(I) = V_C \ln\left(\frac{I_{SHT} - I}{I_{DT}} + 1\right) + V_C \ln\left(\frac{I_{SHD} - I}{I_{DD}} + 1\right) \tag{2.37}$$

where the current $I = [0 \div \min\{I_{SHT}, I_{SHD}\}]$.

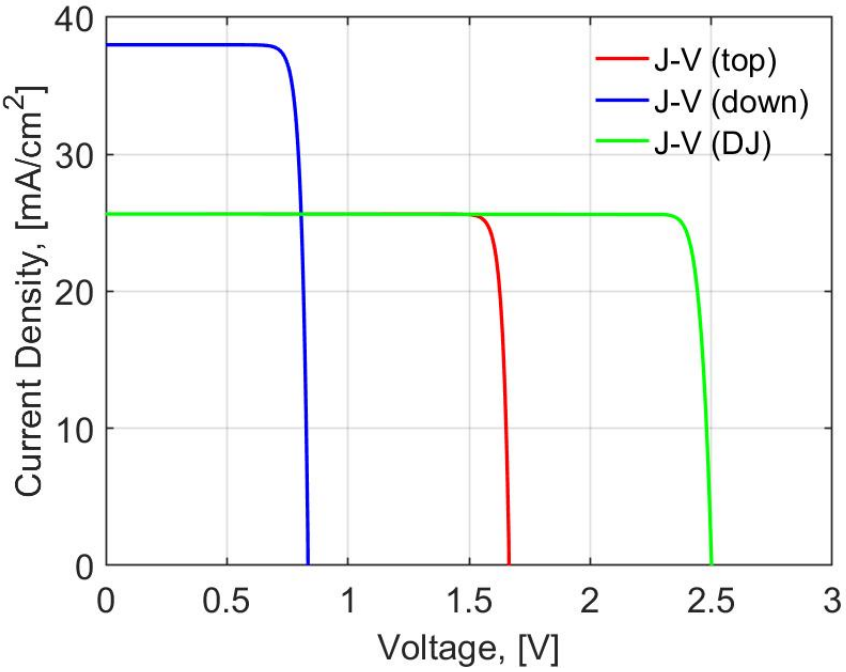

Figure 2.10: J-V characteristics

Fig. 2.10 shows a characteristic J-V related to a top band gap $E_{g1} = 1.97$ and a bottom band gap $E_{g2} = 1.1$.

From Fig. 2.10, we can observe that the characteristic J-V of an ideal DJ solar cell (green line) has its short-circuit current equal to the minimum photocurrent $I_{cc} = \min\{I_{SHT}, I_{SHD}\}$ and the open-circuit voltage is the sum of each one.
In order to obtain the maximum efficiency η (Eq. 1.7), it is necessary to get the maximum power that can be developed by the DJ solar cell. Considering Eq. 2.37:

$$P = I\left[V_C \ln\left(\frac{I_{SHT} - I}{I_{DT}} + 1\right) + V_C \ln\left(\frac{I_{SHD} - I}{I_{DD}} + 1\right)\right] \tag{2.38}$$

The maximum power P_{MAX} can be achieved forcing $\dfrac{dP}{dI} = 0$.

First, it is necessary to get the current I that satisfies the following equation:

$$\ln\left(\frac{I_{SHT} - I}{I_{DT}} + 1\right) + \frac{I}{-I_{SHT} + I - I_{DT}} + \ln\left(\frac{I_{SHD} - I}{I_{DD}} + 1\right) + \frac{I}{-I_{SHD} + I - I_{DD}} = 0 \tag{2.39}$$

By this, the value of I found is nothing more than I_{MAX}. Substituting the value of I_{MAX} into Eq. 2.37 we obtain the value of V_{MAX}, hence P_{MAX}.

As it has already been done for the nominal efficiency η_n (Fig. 2.9), we show the maximum efficiency η as a function of the top bandgap E_{g1} and the bottom bandgap E_{g2}.

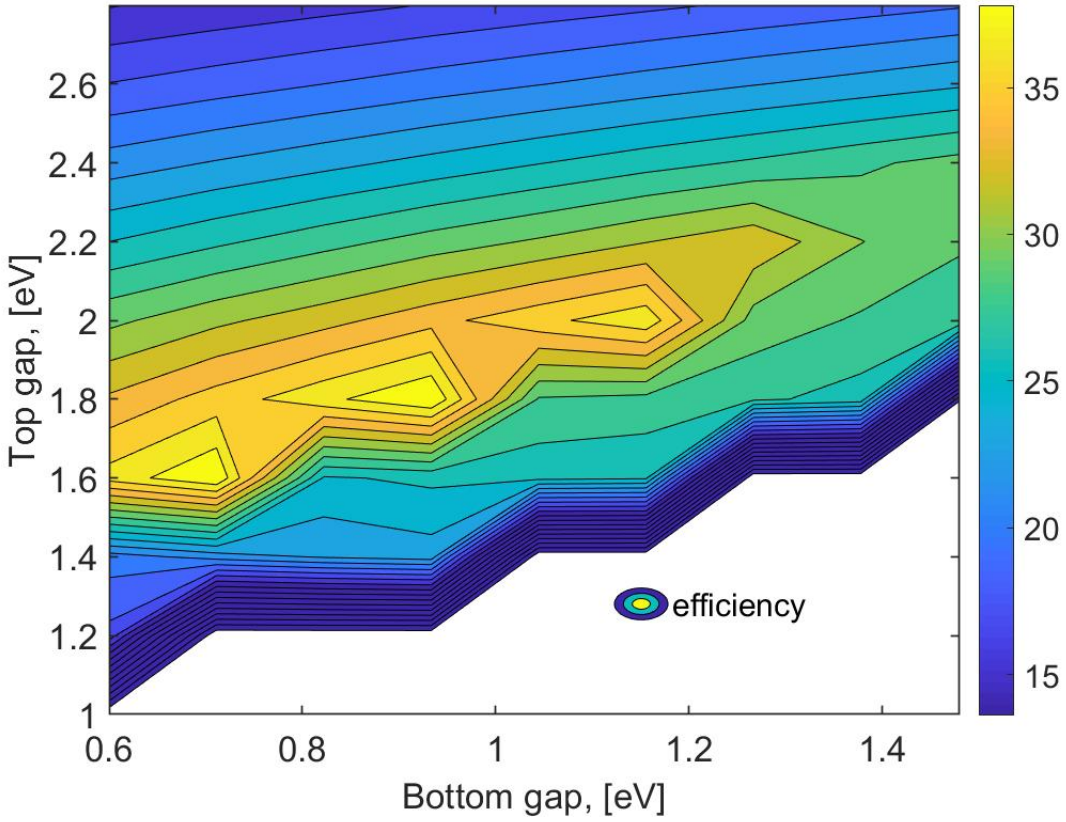

Figure 2.11: Efficiency of an ideal DJ solar cell with $f = 10^{-5}$

The table below summarizes the values of the *nominal efficiency* η_n and the *detailed balance limit of efficiency* η found versus the optimal bandgap for SJ and DJ solar cells based on Shockley-Queisser model:

	f -	Top gap [eV]	Bottom gap [eV]	η_n [%]	η [%]
SJ solar cell	1.09 x 10^{-5}	1.2	-	34.43	30.31
SJ solar cell	1.09 x 10^{-5}	1.25	-	34.4	30.4
DJ solar cell	1.09 x 10^{-5}	1.6	0.71	43.72	39.26
DJ solar cell	1.09 x 10^{-5}	1.8	0.93	42.75	39.32

Putting in comparison the values of efficiency found from Fig. 2.9 and Fig. 2.11 related to a DJ solar cell with that of SJ solar cell (Fig. 2.4), we can conclude that the efficiency of a DJ solar cell is greater than that of a SJ solar cell.
There is the possibility of increasing again the total efficiency using solar cells with

more than two junctions. If we want the limit efficiency of this kind of solar cells it would be enough extend the previously model based on the number of layers chosen. Based on the S-Q model we can obtain an upper bound for the efficiency of the SJ or, in general, for MJ solar cell. For the sake of completeness, considering the DJ and MJ solar cell, the current flow between the diodes is realized, practically, by interconnecting them with intermediate tunnel junctions crossed by the electrons thanks to the tunnel effect. Hence, the circuit model previously exposed should be also modified taking into account intermediate tunnel diodes (see Fig. 1.15).
Anyway, the S-Q model does not take into account several physical constraints limiting the efficiency. Hence, in Chapter 3, we will study a different model in order to obtain a more realistic efficiency for a SJ solar cell and then we will extend it to a new kind of DJ structure.

CHAPTER 3

Device-level model of Single Junction Solar Cells

In the previous chapter, we have explored SJ solar cell and DJ solar cell by a theorical point of view without considering several physical problems such us intrinsic/extrinsic device losses. In this chapter, passing from an ideal model to a physical one, we will explore some physical features of a solar cell leading to an efficiency lower than that ideal; in fact, not only each material has its ability to absorb light of a given wavelength, hence decreasing the probability that for each arriving photon there is a generation of an e-h pair, but also the collection of the photogenerated electrons and holes is in competition with the loss of them because of bulk and surface recombination. These features can be taken into account thanks to the Hovel model [14]. It is a drift-diffusion analytical model based on the assumptions that lifetime, mobility and doping level are reasonably constant, although in reality, these parameters can be function of position above all when the regions of the device are produced by diffusion. However, in our case, Hovel model is an excellent means in predicting a more practical balance of the photocurrent and dark current, hence the external quantum efficiency and the J-V characteristic of a solar cell. The material chosen for the simulations are AlGaAs and GaAs, two of the most important materials used for III-V multiple junction solar cells. Before implementing the Hovel model, we will investigate some features about materials such as AlGaAs and GaAs and explore the minority carriers transport.

3.1 Materials: some properties

The aim of this section is introducing the most important features of the materials used in the thesis. In fact, at the basis of a solar cell there are some semiconductor materials with their intrinsic properties.

3.1.1 Reflectance

One of the hypothesis of the S-Q model is that there is no reflection of photons at the interface between air and the exposed surface of the solar cell.
In a realistic model, it is necessary to consider the Reflection phenomena at the interface because, based on the Snell's law, the amount of photons reaching the solar cell surface is different by that able to cross it. When light reaches the surface, photons can be reflected or refracted based on the refractive index of the material and based on the incident angle of the light at the surface [15], as in figure 3.1:

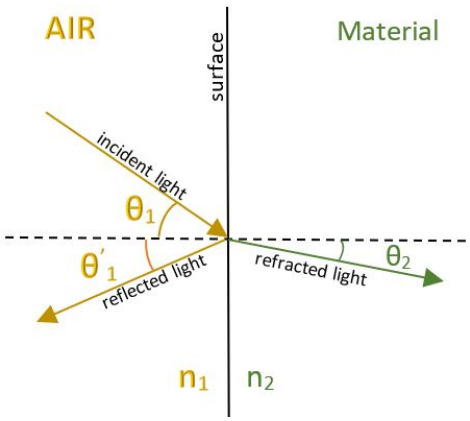

Figure 3.1: Behavior of the incident light at the interface Air-Material.

For our model, we suppose a normal incidence to the solar cell surface. This means that the component that is transmitted through the surface will have the same direction of the incident one, but it is necessary to calculate the amount of reflected light.
By Fresnel equation the Reflectance is:

$$R = \frac{|n_1 - \tilde{n}_2|}{|n_1 + \tilde{n}_2|} \tag{3.1}$$

where the refraction index of the air n_1 is equal to 1 and $\tilde{n}_2$ is the complex refractive index of the material chosen.
The complex refractive index is composed by a real part and by an imaginary part including the extinction coefficient k:

$$\tilde{n} = n - ik$$

If the Reflectance is high, the amount of photons absorbed by the material semiconductor decreases leading to a lower efficiency of the solar cell.
Fig. 3.2 shows three different cases of the Reflectance where it is possible detect that the Reflectance is high for the case studies Air-$Al_{0.4}Ga_{0.6}As$ and Air-GaAs based on the difference between the refractive index n_1 and $\tilde{n_2}$; instead, at the interface $Al_{0.4}Ga_{0.6}As$-GaAs the value of R is very low leading to a small amount of light reflected.

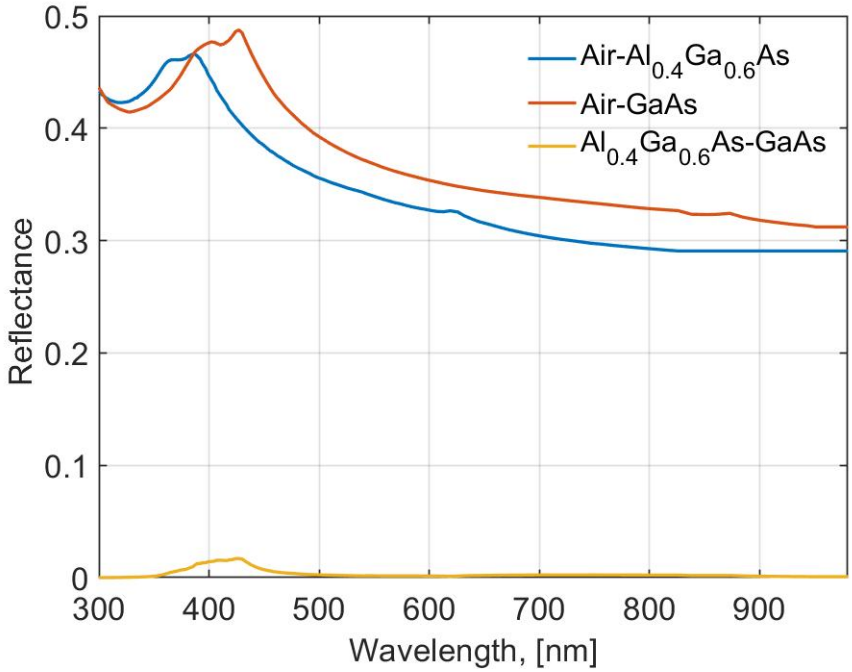

Figure 3.2: Reflectance for: $Al_{0.4}Ga_{0.6}As$ blue line, Air-GaAs red line, $Al_{0.4}Ga_{0.6}As$-GaAs orange line.

In general, it is helpful to put as first layer a material whose index of refraction is similar to that of the air in order to have $R \longrightarrow 0$. Today, is very common using an ARC (Anti-Reflection Coatings) in order to reduce the reflected light.

3.1.2 Absorption coefficient

By S-Q model [12]:

"*Each photon with energy greater than* $h\nu_g$ *produces one electronic charge* q".

This hypothesis, in a physical model, cannot be applied because each material responds differently based on the wavelength. In order to find out a realistic efficiency is necessary to introduce the absorption coefficient α proportional to the extinction coefficient k and to the wavelength λ.

$$\alpha = \frac{4\pi k}{\lambda} \tag{3.2}$$

The absorption coefficient α is measured in units of a reciprocal distance [14]. It is intrinsic to each material giving us a starting point in order to understand how materials responds to different wavelengths.

In general, the larger the bandgap, the smaller the value of α for a given wavelength.

It is also necessary to underline that the absorption coefficient is linked to the densities of states in the valence band and in the conduction one changing if the semiconductor

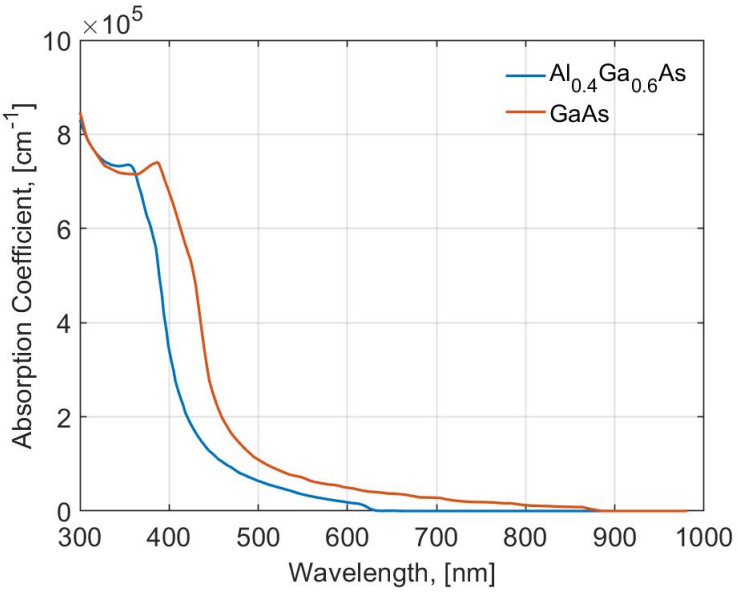

Figure 3.3: Absorption coefficient

material has a direct or indirect bandgap.
Fig. 3.3 shows the absorption coefficient for GaAs and $Al_{0.4}Ga_{0.6}As$ materials.
GaAs can absorb until roughly 870 nm, but in the first part of the spectrum the coefficient α is lower than that one of $Al_{0.4}Ga_{0.6}As$ that is able to absorb until roughly 640 nm.

3.1.3 Generation rate

The absorption problem, so the generation of e-h pairs, is not only related to the absorption coefficient and to the Reflectance, but also to the depth of the material.
By the previous section, the absorption coefficient of a material is given by $\alpha(\lambda)$; we know also, by the first chapter, the expression of the photon flux incident on the solar cell (Eq. 1.9), now renamed F_0. If a semiconductor is illuminated from a light source, a fraction of photons crosses the surface, then travels through the device; the amount of photons absorbed is proportional to the intensity of the incident flux [8]. Hence, it is possible to introduce $F(x)$ that describes the photon flux as a function of depth in the solar cell [16].
It is described by the the Beer-Lambert law:

$$F(x) = (1 - R)F_0 e^{-\alpha x} \tag{3.3}$$

where R is the reflectance at the surface. Fig. 3.4 shows the Relative Photon Flux (RPF) $F(x)/F_0$ in the range of wavelengths $[300 \div 824]$ nm for GaAs material semiconductor. We can observe that for $\lambda = 300$ nm the RPF has a different behavior respect to that for $\lambda = 824$ nm.

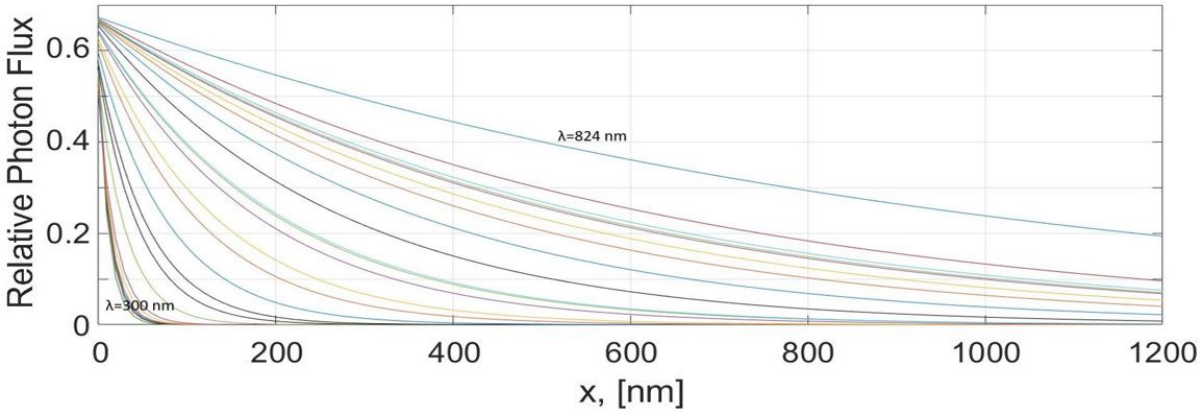

Figure 3.4: Relative photon flux in the solar cell in the range of $\lambda = [300 \div 824]$ nm.

In fact, for $\lambda = 300$ nm the photons will be absorbed above all for $x < 100$ nm based on the fact the RPF has a strongly exponential decreasing; instead, for $\lambda = 824$ nm the photons can be absorbed very good until $x < 600$ nm thanks to the relative RPF that decreases always exponentially, but less pronounced. Hence, we can detect that photons incident on the solar cell surface falls off in intensity by a factor 1/e for each $1/\alpha$, *absorption length*, distance into the material [14].
It is necessary taking into account this effect by choosing properly the dimensions of the solar cell in order to absorb at best the solar spectrum. For example, if we want to absorb photons with $\lambda = 824$ nm and we choose an absorption region dimension of 200 nm, from Fig. 3.4 we can deduce that most photons escape without generating e-h pairs, decreasing the efficiency of the solar cell; instead photons with $\lambda = 300$ nm will be fully absorbed.
Summarizing, the generation of the e-h pairs is not uniform along the device, but it is based on two factors:

- wavelength λ;
- depth x.

Eq. 3.3 allows the Generation rate $G(\lambda, x)$ to be written as:

$$G(\lambda, x) = \alpha(\lambda)(1 - R(\lambda))F_0(\lambda)\mathrm{e}^{(-\alpha(\lambda)x)} \tag{3.4}$$

Thanks to Eq. 3.4 it is possible to analyze the distribution of the photons absorbed along the device with respect to the total photon flux incident on the surface of the solar cell. Let's apply Eq. 3.4 to GaAs and $Al_{0.4}Ga_{0.6}As$ and detect the differences.
Observing Fig.3.5, based on the SI distribution, the following features can be detected for GaAs:

- $\lambda < 340$ nm the SI is low and photons are absorbed in the first layers of the material.

- 340 nm $< \lambda <$ 460 nm the SI is high, photons are absorbed first of all in the first 10 nm, but also e-h pairs are generated at greater depth. The peak of absorption is around 420 nm.
- 460 nm $< \lambda <$ 700 nm the SI is high, photons are able to get deeper into the device, but totally $G(\lambda, x)$is lower than the previous case.

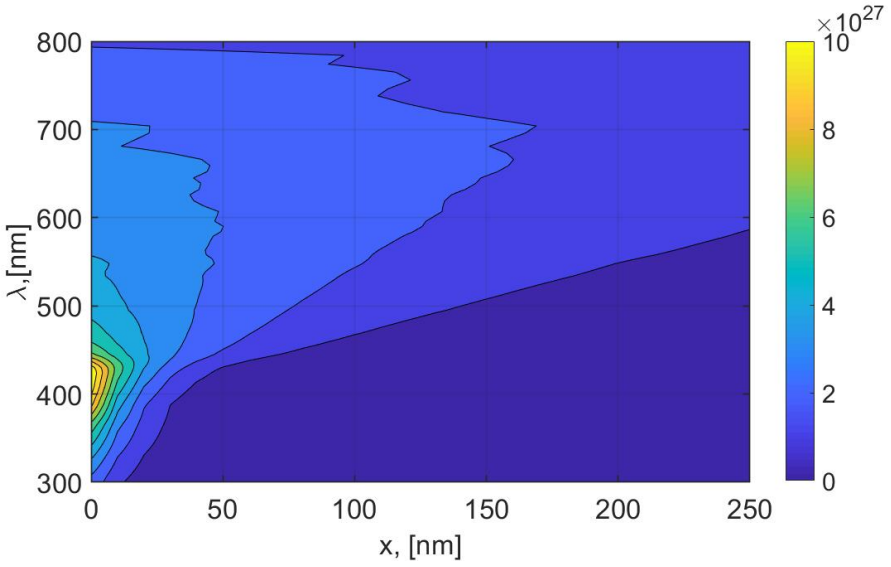

Figure 3.5: Generation rate in GaAs material measured in $[\mathrm{s}^{-1}\,\mathrm{m}^{-3}]$.

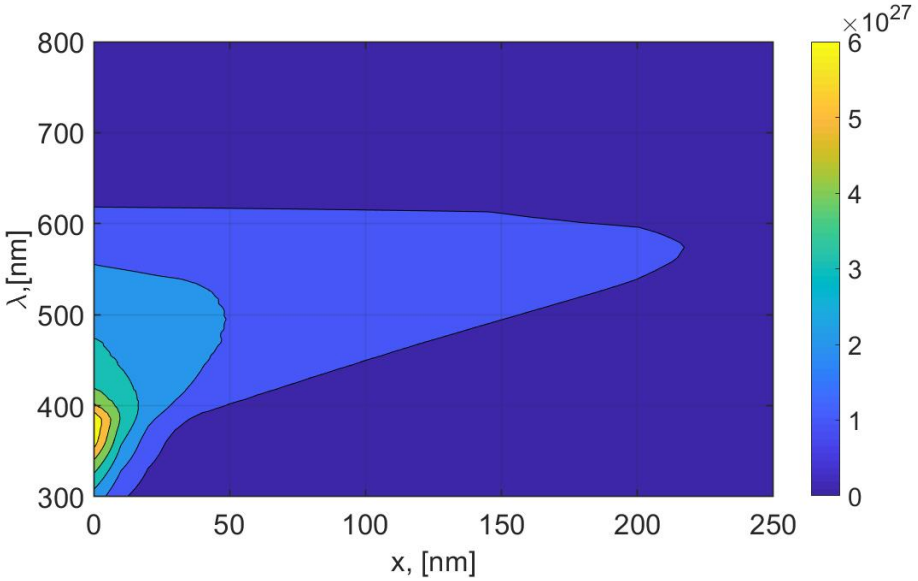

Figure 3.6: Generation rate in $Al_{0.4}Ga_{0.6}As$ material measured in $[\mathrm{s}^{-1}\,\mathrm{m}^{-3}]$

Fig. 3.6 is about the Generation rate of $Al_{0.4}Ga_{0.6}As$:

- $\lambda < 340$ nm the SI is low and photons are absorbed in the first layers of the material.
- 340 nm $< \lambda <$ 390 nm the SI is high, photons are absorbed first of all in the first 10 nm, but also e-h pair are generated at greater depth.
- 390 nm $< \lambda <$ 700 nm the SI is high, photons are able to get deeper into the device, but intensity of the $G(\lambda, x)$ is lower than the previous case.

Both the Generation rate of Fig. 3.6 and Fig. 3.5 confirms the considerations done in the previous section, in fact the generation of e-h of $Al_{0.4}Ga_{0.6}As$ is greater than that GaAs for $\lambda < 400$ nm.
When e-h pairs are created, not all of them can be collected at the terminals because, moving across the device, they suffer the bulk and surface recombination.

3.1.4 Bulk & Surface Recombination

From Fig. 1.9, free electrons in conduction band and free holes in valence band, must be collected to the metal contacts in order to make a solar cell work. The problem is that there are several *recombination mechanisms* [18], as said in Sec. 2.1: recombination through traps (*defects*) in the forbidden gap (Fig. 3.7a), radiative (*band-to-band*) recombination (Fig. 3.7b), and Auger recombination (Fig. 3.7c). Based on these phenomena, the electrons and holes involved cannot deliver their energy to the load.

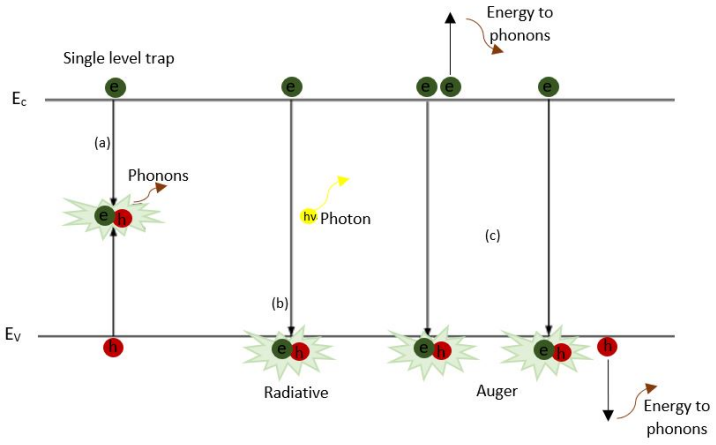

Figure 3.7: Band Diagram of a p-n junction

The recombination linked to the single level trap within the forbidden gap is also known as *Shockley-Read-Hall* recombination where the carrier lifetimes τ_{SLT} are given by:

$$\tau_{SLT} = \frac{1}{\sigma \, \nu_{th} \, N_T} \tag{3.5}$$

where σ is the capture cross section, ν_{th} is the thermal velocity of the carriers and N_T is the concentration of traps [18]. Based on Eq. 3.5, increasing the concentration of traps the probability of interaction with them increases, hence the lifetimes, inversely proportional to the trap concentration, decrease and the rates of recombination grow. Considering a SJ solar cell (Fig. 1.8), in each *n-p* region there are far fewer minority carriers than majority carriers, hence it is expecting that the recombination rate is solely dependent on the minority carriers. The *Shockley-Read-Hall* recombination rate R_{SLT} in a *p*-type region, in *low injection* condition ($n_0 \leq n \ll p_0$), is equal to:

$$R_{SLT} \approx \frac{n - n_0}{\tau_{SLT,n}} \tag{3.6}$$

The same expression, function of holes, is valid in a *n*-type region.
The inverse of the photo-generation process is the *Radiative recombination*; when it occurs, electrons and holes recombine delivering the energy in the form of emitted photons. The *Radiative recombination* rate, in a *p*-type material for *low injection* condition, can be written as:

$$R_{\lambda} \approx \frac{n - n_0}{\tau_{\lambda,n}} \tag{3.7}$$

where the carrier lifetimes is equal to:

$$\tau_{\lambda,n} = \frac{1}{p_0 B} \tag{3.8}$$

where B is the bimolecular recombination coefficient.
Finally, in *Auger recombination* (Fig. 3.7c) the energy of electron or hole transition is given to another minority carrier that then relaxes thermally delivering its excess energy and momentum to phonons. In a *p*-type material, in *low injection* condition, the net *Auger* recombination rate can be written as:

$$R_{Auger} \approx \frac{n - n_0}{\tau_{Auger,n}} \tag{3.9}$$

where the carrier lifetimes is equal to:

$$\tau_{Auger,n} = \frac{1}{\Lambda_n p_0^2} \tag{3.10}$$

Finally, Eq. 3.11 expresses the *total Recombination*:

$$R = \sum_{traps\, i} R_{SLT,i} + R_{\lambda} + R_{Auger} \tag{3.11}$$

and the total carrier lifetime is equal to:

$$\frac{1}{\tau} = \sum_{traps\, i} \frac{1}{\tau_{SLT,i}} + \frac{1}{\tau_{\lambda}} + \frac{1}{\tau_{Auger}} \tag{3.12}$$

Another important phenomena in the solar cells is the *Surface recombination*. Each semiconductor is characterised by a periodicity of its crystal lattice, its abrupt termination leads to a high concentration defects that are called *dangling bonds*.

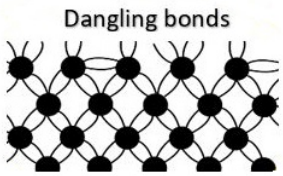

Figure 3.8: Dangling Bonds.

Electrons and holes can recombine through them just as in Fig. 3.7a; hence, based on the abrupt discontinuity of the lattice structure at the top and bottom surface of the solar cell, many charges recombine and cannot be collected to the metal contacts leading to a lower efficiency. The surface recombination rate can be written as:

$$R_{S,n} = S_n(n_p - n_{p0}); \quad \text{for } p\text{-type material} \tag{3.13}$$

$$R_{S,p} = S_p(p_n - p_{n0}); \quad \text{for } n\text{-type material} \tag{3.14}$$

where:

- S_n is the surface recombination velocity of the electrons minority carriers in the p-type material;
- S_p is the surface recombination velocity of the holes minority carriers in the n-type material.

Electron-hole pairs are created inside the solar cell thanks to the absorption of the photons. The objective is to collect the minority carriers before they are lost to recombination [18].

3.1.5 Minority Carriers Transport

The aim of this section is to show the carrier transport and we will try to find the recombination phenomena in opposition to the collection of the minority carriers.
Electrons and holes are subject to the drift and diffusion processes. The drift process, so the generation of the *drift current*, occurs when an electric field E is applied to the semiconductor, hence each electron and hole moves in the opposite direction to the field.

Fig. 3.9 shows the electrons and holes flux generated by the electric field E.

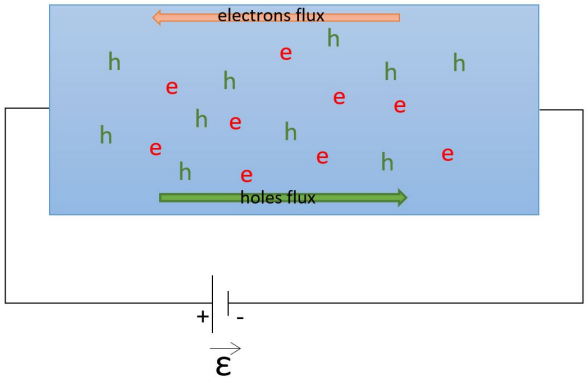

Figure 3.9: Drift current.

Eq. 3.15 and Eq. 3.16 are the analytical expressions for the *Drift current*:

$$J_n = q\mu_n nE; \tag{3.15}$$

$$J_p = q\mu_p pE. \tag{3.16}$$

The other current component is the *Diffusion current*. It is generated if there is a non-uniform concentration of charges along the device (Fig. 3.10).

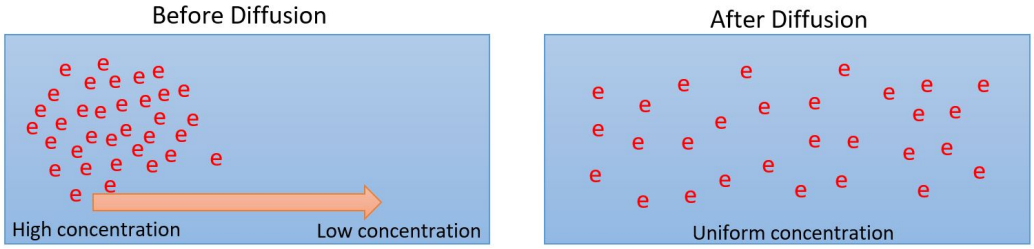

Figure 3.10: Diffusion current.

$$J_n = qD_n\frac{dn}{dx}; \tag{3.17}$$

$$J_p = -qD_p\frac{dp}{dx}. \tag{3.18}$$

where D_n and D_p are the *diffusion coefficients*.
From this, we introduce the parameter $L_p = \sqrt{D_p\tau_p}$, *diffusion length* for holes in the n-region, and $L_n = \sqrt{D_n\tau_n}$, *diffusion length* for electrons in p-region. L_p and L_n are

very important parameters because give us an idea of how long a hole or electron can move, along the device, without a recombination phenomena occurs. For example, if the *diffusion length* is lower than the thickness of a region of the solar cell, electrons n_p or holes p_n are not able to be collected because they recombine before arriving to the metal contacts. Hence, it is necessary also taking into account the *diffusion length* in order to design the solar cell.
The total current density for electrons is:

$$J_n = q\mu_n nE + qD_n \frac{dn}{dx} \tag{3.19}$$

the total current density for holes is:

$$J_p = q\mu_p pE - qD_p \frac{dp}{dx} \tag{3.20}$$

Now, we consider a SJ solar cell. The relative p-n band diagram is showed in Fig. 3.11. Let's try to understand how electrons and holes minority carriers can be collected to the terminals.

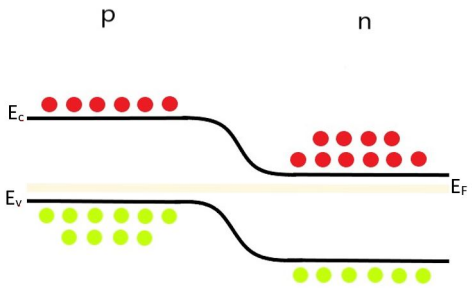

Figure 3.11: Band Diagram of a p-n junction

From Fig. 3.11, at thermal equilibrium, in the p-region electrons n_p are the minority charges; holes, p_p, are majority charges that cannot cross the high built-in potential barrier and go into the n-region. In this last one, holes are the minority carriers; instead electrons, majority carriers n_n, cannot overcome the barrier and go in the p-region.
When the p-n junction is under illumination e-h pairs are generated such as in figure 3.12. In this situation, in the p-type (n-type), the increase of the n_p (p_n) concentration rate under illumination in percentage is greater than the increase of the majority carriers p_p (n_n). The situation, in which the change is significant only for the minority charges is called *low injection level*. The n_n and p_p majority carriers cannot cross the built-in barrier, but minority carriers n_p in the p-region and p_n in the n-region *diffuse* towards the depletion region where the electric field sweep out them into the region where they become majority carriers [17].
In opposition to the carrier transport described, there are the radiative and non-radiative *recombination mechanisms* that, if occur, lead to the loss of the minority

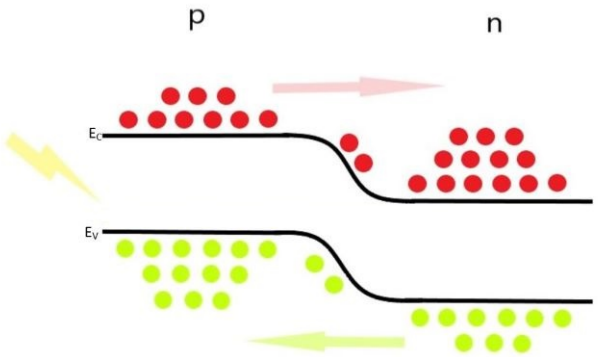

Figure 3.12: p-n junction under illumination.

charges n_p and p_n. In addition, the surface recombination phenomena creates a current flux opposite in direction to that photogenerated. The n_p and p_n carriers diffuse towards the depletion region according to the arrow's direction of Fig. 3.12. In reality, let's consider that there are many dangling bonds in the p/n-surface, hence the concentration of electrons n_p/p_n photogenerated in non-uniform along the p/n-region. Hence, many electrons n_p/ holes p_n diffuse towards the p/n-surface in order to recombine with the free holes/electrons generated by the dangling bonds. It is necessary taking into account this flux toward the surface.
The behavior of the minority carrier linked to the surface recombination, so the current density toward the surface is expressed by:

$$J_{Sp} = qS_p(p_n - p_{n0}) \tag{3.21}$$

$$J_{Sn} = qS_n(n_p - n_{p0}) \tag{3.22}$$

We will observe the effect of the surface recombination in Sec. 3.3.1, where we will discover that it is non negligible leading to a lower efficiency. The problem of dangling bonds can be solved with a technique of *passivation*.

3.1.6 Mobility model

GaAs and AlGaAs are the materials used in the simulations and will be necessary find intrinsic parameter values of the materials that depends on the mobility of electrons μ_n and holes μ_p. In this context, the choice of implementing a model able to provide mobility values changing the doping level. The model is that developed by M.Sotoodeh, A.H.Khalid, and A. A. Rezazadeh [13] based on physically interpolation schemes. This kind of model gives the possibility to find out electrons and holes mobility not only for binary compounds, such as GaAs or InP, but also for ternary compounds as $Al_xGa_{(1-x)}As$ and quaternary alloys $In_{1-x}Ga_xAs_yP_{1-y}$.
The low-field mobility model is based on Eq. 3.23:

$$\mu_{LF}(N,T) = \mu_{min} + \frac{\mu_{max}(300K)\left(\frac{300K}{T}\right)^{\theta_1} - \mu_{min}}{1 + \left(\frac{N}{N_{ref}(300K)\left(\frac{T}{300K}\right)^{\theta_2}}\right)^{\lambda}} \tag{3.23}$$

where $\mu_{max}(T)$ is the saturation value of mobility at very low doping concentration, μ_{min} is the saturation value of mobility at very high doping concentration and θ_1, θ_2, λ influence the mobility depending on the temperature T.
In the table there are parameters value for Eq. 3.23 both for GaAs and AlGaAs:

	$\mu_{max}(300K)$ $\left[\frac{cm^2}{Vs}\right]$	$\mu_{min}(300K)$ $\left[\frac{cm^2}{Vs}\right]$	$N_{ref}(300K)$ $[cm^{-3}]$	λ	θ_1	θ_2
$GaAs_{electron}$	9400	500	6 x 10^{16}	0.394	2.1	3.0
$GaAs_{hole}$	491.5	20	1.48 x 10^{17}	0.38	2.2	3.0
$AlAs_{electron}$	400	10	5.46 x 10^{17}	1	2.1	3.0
$AlAs_{hole}$	200	10	3.84x 10^{17}	0.488	2.24	3.0
$Al_{0.3}Ga_{0.7}As_{hole}$	240	5	1 x 10^{17}	0.324	- -	- -

For ternary compounds the values in the table are function of the *mole fraction* x. Hence it is necessary to adopt interpolation schemes. The $Al_xGa_{(1-x)}As$ material changes its features based on Al mole fraction x. GaAs is a direct Energy gap semiconductor with its minimum conduction band in the Γ-valley, instead AlAs is an indirect Energy gap material with its minimum conduction band in the X-valley. Hence, the Energy Gap of the $Al_xGa_{(1-x)}As$ changes by direct to indirect based on Al mole fraction.
By Fig. 3.13, the values of the three valleys are obtained with a quadratic interpolation scheme (Eq. 3.24):

$$E_{g\nu}(x) = xE_{g\nu}(\text{AlAs}) + (1-x)E_{g\nu}(\text{GaAs}) - b(\text{AlGaAs})x(1-x) \tag{3.24}$$

where b is the band gap bowing parameter.

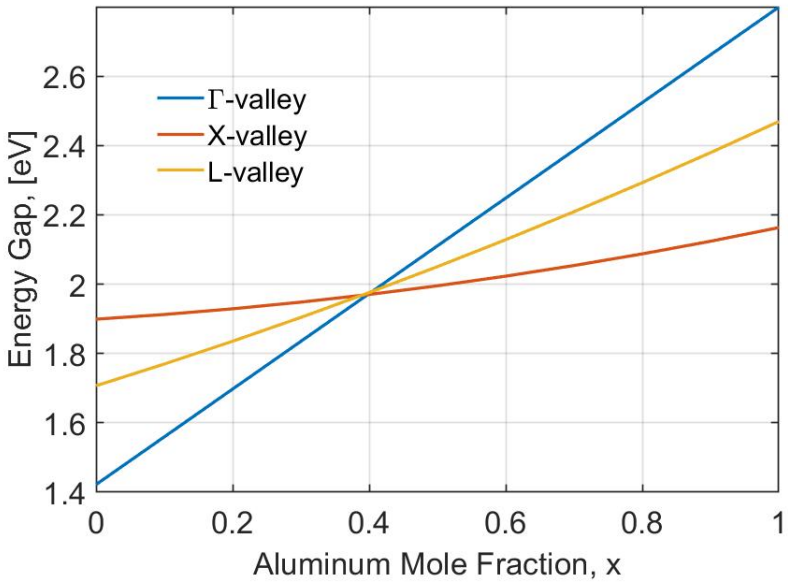

Figure 3.13: Γ-valley, X-valley and L-valley for $Al_xGa_{(1-x)}As$.

It is possible detect by Fig. 3.13 the critical point is for $x = 0.4$.

- for $x < 0.4$ $Al_xGa_{(1-x)}As$ is a direct band-gap material ;
- for $x > 0.4$ $Al_xGa_{(1-x)}As$ is an indirect band-gap material.

Considering that the value of the Eg can change based on x, in order to find out μ_{max} and μ_{min} for Eq. 3.23, it is defined an effective mobility, for electrons:

$$\mu_M(x) = \frac{n_\Gamma(x)\mu_D(x) + [n_X(x) + n_L(x)]\,\mu_I(x)}{n} \tag{3.25}$$

where $\mu_D(x)$ and $\mu_I(x)$ are the electron mobility in the direct and indirect conduction valleys. The parameters $n_\Gamma(x), n_X(x), n_L(x)$ are the concentrations in corresponding conduction band minima. In order to find out $\mu_D(x)$, it is possible use Eq. 3.26:

$$\mu_D = \mu_M(\text{GaAs}) \left[\frac{m_{n\Gamma}(GaAs)}{m_{n\Gamma}(x)}\right]^{3/2} \frac{\varepsilon_\infty^{-1}(\text{GaAs}) - \varepsilon_s^{-1}(\text{GaAs})}{\varepsilon_\infty^{-1}(x) - \varepsilon_s^{-1}(x)} \tag{3.26}$$

where $m_{n\Gamma}(\text{GaAs})$ is the effective mass in the relative conduction band for the electrons, instead ε_∞ is the optical dielectric constant and ε_s is the static one. In order to find out $m_{n\Gamma}(x)$ is used a linear interpolation scheme:

$$m_{n\nu}(x) = x m_{n\nu}(x)(\text{AlAs}) + (1-x) m_{n\nu}(x)(\text{GaAs}) \tag{3.27}$$

Based on Eq. 3.28 it is possible obtain both the optical and static dielectric constant.

$$\varepsilon_{\infty,s}(x) = \frac{1+2A+2B}{1-A-B} \tag{3.28}$$

where:

- A= $x\dfrac{\varepsilon_{\infty,s}(\text{AlAs})-1}{\varepsilon_{\infty,s}(\text{AlAs})+2}$
- B= $(1-x)\dfrac{\varepsilon_{\infty,s}(\text{GaAs})-1}{\varepsilon_{\infty,s}(\text{GaAs})+2}$

Then, the others formulas are:

$$\mu_I = \mu_M(\text{AlAs}) \tag{3.29}$$

$$N_{n,ref} = [N_{n,ref}(\text{GaAs})]^{1-x}\,[N_{n,ref}(\text{AlAs})]^{x} \tag{3.30}$$

$$\theta_{n1} = \frac{(1-x)\theta_{n1}(\text{GaAs}) + x\theta_{n1}(\text{AlAs})}{1+mx(1-x)} \tag{3.31}$$

In order to find out the mobility for holes, the parameters of μ_p(AlGaAs) like $\mu_{p,max}(300K)$, $\mu_{p,min}$, λ and $N_{p,ref}$ are obtained with quadratic interpolation scheme using GaAs, AlAs and $Al_{0.3}Ga_{0.7}As$; instead, θ_{p1}(AlGaAs) is assumed equal to θ_{n1}(AlGaAs) and θ_{p2}(AlGaAs) is assumed equal to θ_{p2}(GaAs).
The quadratic interpolation scheme is that of Eq. 3.32:

$$P_{\text{Al}_x\text{Ga}_{(1-x)}\text{As}}(x) = xP_{\text{AlAs}} + (1-x)P_{\text{GaAs}} - P_{\text{Al}_{0.3}\text{Ga}_{0.7}\text{As}}x(1-x) \tag{3.32}$$

In the following table we summarize the values of the parameters used, taken by the reference article:

	ε_s [ε_0]	ε_∞ [ε_0]	$E_{g\Gamma}$ [eV]	E_{gX} [eV]	E_{gL} [eV]	$m_{n\Gamma}$ [eV]	m_{nX} [m_0]	m_{nL} [m_0]	b_G [eV]	b_X [eV]	b_L [eV]
GaAs	12.90	10.92	1.422	1.899	1.707	0.065	0.85	0.56	–	–	–
AlAs	10.06	8.16	2.799	2.163	2.469	0.150	0.71	0.66	–	–	–
AlGaAs	–	–	–	–	–	–	–	–	0	0.143	0.15

In Fig. 3.14 we report an example of holes mobility obtained with this model:

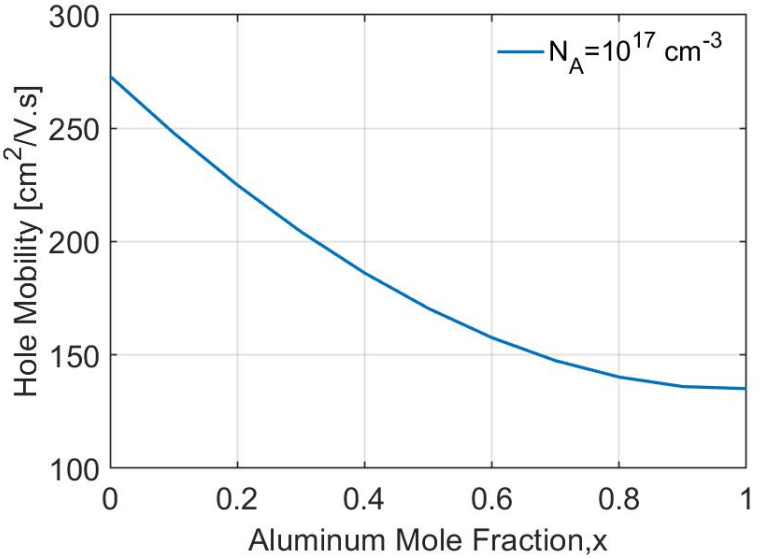

Figure 3.14: AlGaAs Hole mobility for $N = 10^{17}$ $\mathtt{cm}^{-3}$.

Following, an example of electron mobility for AlGaAs fixing the doping concentration, changing the mole fraction.

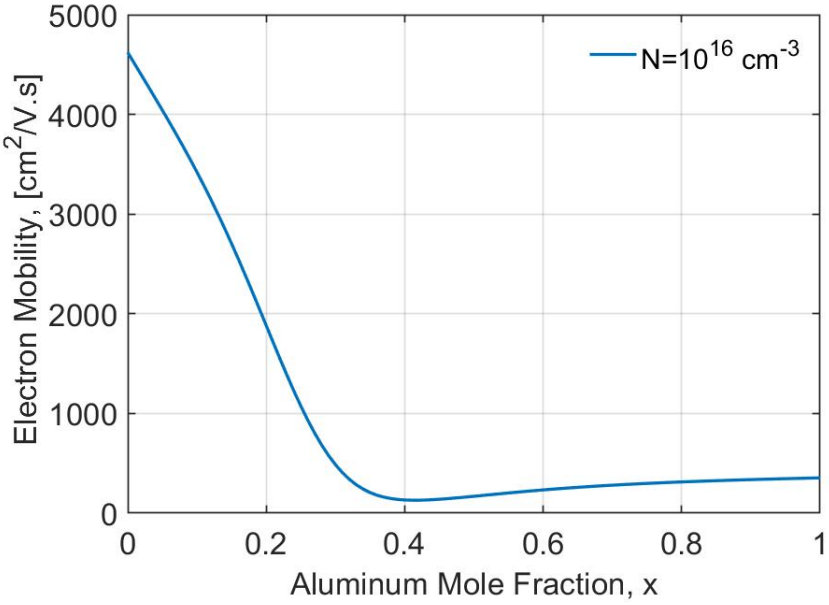

Figure 3.15: AlGaAs Electron mobility for $N = 10^{16}$ $\mathtt{cm}^{-3}$.

3.2 Single Junction solar cell: Analytical Approach

The aim of this section is to obtain a model able to describe the current flow of the minority charges under illumination along a SJ solar cell. Let's consider the continuity equations for minority carriers under *low-injection* condition.

Holes equation in the n-type material:

$$\frac{1}{q}\left(\frac{dJ_p}{dx}\right) - G_p + \frac{p_n - p_{n0}}{\tau_p} = 0 \tag{3.33}$$

Electrons equation in the p-type material:

$$\frac{1}{q}\left(\frac{dJ_n}{dx}\right) + G_n - \frac{n_p - n_{p0}}{\tau_n} = 0 \tag{3.34}$$

where p_{n0} and n_{p0} are the minority carrier concentrations at equilibrium condition. Into Eq. 3.33 and Eq. 3.34 we can note both the Generation and the explicit Recombination term. The case study in order to derive the drift-diffusion model (the so-called Hovel model) is a solar cell with a p-type emitter (exposed to the sun) and n-type base [14]. All following considerations are the same in the case for n-type emitter and p-type base, only changing n_p with p_n and otherwise.
Let's consider a p-n junction with both sides of the junction uniform in doping. This means that there is not an Electric Field E outside the depletion region.

3.2.1 *p*-type Emitter

In the case of uniform doping, Eq. 3.19 becomes:

$$J_n = qD_n\frac{dn_p}{dx} \tag{3.35}$$

Substituting Eq. 3.35 into Eq. 3.34 yields:

$$\frac{d^2(n_p - n_{p0})}{dx^2} - \left(\frac{n_p - n_{p0}}{D_n\tau_n}\right) + \frac{G_n}{D_n} = 0 \tag{3.36}$$

Considering the Generation rate equation, Eq. 3.4, the complete expression of the Eq. 3.36 is:

$$\frac{d^2(n_p - n_{p0})}{dx^2} - \left(\frac{n_p - n_{p0}}{D_n\tau_n}\right) + \left(\frac{\alpha F(1-R)\mathrm{e}^{(-\alpha x)}}{D_n}\right) = 0 \tag{3.37}$$

where F is the photon flux.

Solution of the differential equation

In order to solve Eq. 3.37, let's rename the following terms :

- $y(x) = n_p - n_{p0}$;
- $b = \dfrac{1}{D_n \tau_n}$
- $f(x) = -\left(\dfrac{\alpha F(1-R)\mathrm{e}^{(-\alpha x)}}{D_n}\right)$

the equation has the shape of a *second order non-homogeneous differential equation*:

$$y''(x) - by(x) = f(x) \tag{3.38}$$

The solution is the sum of:

- $z(x)$: homogeneous function associated to the Eq. 3.38;
- $\varphi(x)$: particular solution of the Eq. 3.38.

First, consider the homogeneous function in order to find out z(x):

$$y''(x) - by(x) = 0 \tag{3.39}$$

whose characteristic equation is:

$$k^2 - bk = 0 \tag{3.40}$$

The solutions are real and distinct such as $k_1 = \sqrt{b}$ and $k_2 = -\sqrt{b}$. The function $z(x)$ will be:

$$z(x) = \Gamma \mathrm{e}^{\left(x\sqrt{b}\right)} + \Theta \mathrm{e}^{\left(-x\sqrt{b}\right)} \tag{3.41}$$

where Γ and Θ are the two integration constants.
In order to find the particular solution $\varphi(x)$, apply *similarity method.* Observing the term $f(x)$, it has the shape:

$$f(x) = \rho(x)\mathrm{e}^{-\beta x} \tag{3.42}$$

where $\rho(x)$ is of zero degree.
β is not a solution of the equation Eq. 3.40, hence the particular solution is:

$$\varphi(x) = A\mathrm{e}^{-\alpha x} \tag{3.43}$$

In order to find A, consider the equation of (3.38) and replace in it the function $\varphi(x)$, whose derivatives are:

- $\varphi(x)' = -A\alpha e^{-\alpha x}$
- $\varphi(x)'' = A\alpha^2 e^{-\alpha x}$

The resulting expression is:

$$A\alpha^2 e^{-\alpha x} - bAe^{-\alpha x} = -\left(\frac{\alpha F(1-R)e^{(-\alpha x)}}{D_n}\right)$$

and A results as:

$$A = -\left(\frac{\alpha F(1-R)}{D_n(\alpha^2 - b)}\right)$$

Considering Eq. 3.43 and the expression of the diffusion length $L_n = \sqrt{D_n \tau_n}$:

$$\varphi(x) = -\frac{\alpha F(1-R)\tau_n}{\alpha^2 L_n^2 - 1} e^{-\alpha x} \tag{3.44}$$

Equation Eq. 3.37 has the following solution:

$$n_p - n_{p0} = \Gamma e^{\left(\frac{x}{L_n}\right)} + \Theta e^{\left(-\frac{x}{L_n}\right)} - \frac{\alpha F(1-R)\tau_n}{\alpha^2 L_n^2 - 1} e^{-\alpha x} \tag{3.45}$$

By the trigonometric formulas:

- $e^x = \cosh(x) + \sinh(x)$
- $e^{-x} = \cosh(x) - \sinh(x)$

Eq. 3.45 becomes:

$$n_p - n_{p0} = \Gamma\left[\cosh\left(\frac{x}{L_n}\right) + \sinh\left(\frac{x}{L_n}\right)\right] + \Theta\left[\cosh\left(\frac{x}{L_n}\right) - \sinh\left(\frac{x}{L_n}\right)\right] - \frac{\alpha F(1-R)\tau_n}{\alpha^2 L_n^2 - 1} e^{-\alpha x} \tag{3.46}$$

Renaming $A = (\Gamma + \Theta)$ and $B = (\Gamma - \Theta)$:

$$n_p - n_{p0} = A\cosh\left(\frac{x}{L_n}\right) + B\sinh\left(\frac{x}{L_n}\right) - \frac{\alpha F(1-R)\tau_n}{\alpha^2 L_n^2 - 1} e^{-\alpha x} \tag{3.47}$$

Eq. 3.47 give us the minority carriers concentration, $n_p - n_{p0}$, along the emitter part of the solar cell device.
Based on the fact that the concentration of electrons changes along the x-axis because of several physical phenomena, it is necessary taking into account these constraints into Eq. 3.47 through the coefficients A and B.

A and B coefficients

In order to obtain the coefficients A and B of Eq. 3.47, consider the boundary conditions referring to the emitter part of Fig. 3.16.

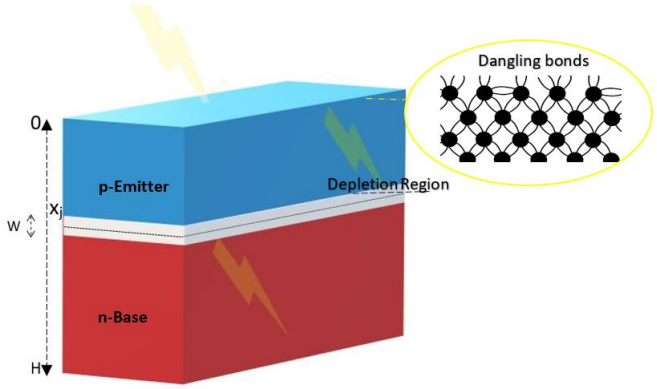

Figure 3.16: p-n solar cell structure.

In Fig. 3.16, the total width of the solar cell is H, of which W is the dimension of the depletion region. The boundary conditions are at the surface because of the surface recombination phenomena and at the interface with the depletion region, so for $x = x_j$. These two can be expressed by the following equations:

$$\frac{d(n_p - n_{p0})}{dx} = \frac{S_n}{D_n}(n_p - n_{p0}); \quad \text{for } x = 0 \tag{3.48}$$

$$n_p - n_{p0} = 0; \quad \text{for } x = x_j \tag{3.49}$$

Let's apply Eq. 3.48:

$$\frac{A}{L_n}\sinh\left(\frac{x}{L_n}\right)+\frac{B}{L_n}\cosh\left(\frac{x}{L_n}\right)+\delta\alpha e^{-\alpha x} = \frac{S_n}{D_n}\left[A\cosh\left(\frac{x}{L_n}\right) + B\sinh\left(\frac{x}{L_n}\right) - \delta e^{-\alpha x}\right]$$

where: $\delta = \dfrac{\alpha F(1-R)\tau_n}{\alpha^2 L_n^2 - 1}$.

Put $x = 0$:

$$\frac{B}{L_n} + \delta\alpha = \frac{S_n}{D_n}(A - \delta)$$

$$B = A\frac{S_n L_n}{D_n} - \delta L_n\left(\alpha + \frac{S_n}{D_n}\right) \tag{3.50}$$

In order to obtain the A coefficient, one can consider the 2^{nd} boundary equation Eq. 3.49.

For $x = x_j$:

$$A\cosh\left(\frac{x_j}{L_n}\right) + B\sinh\left(\frac{x_j}{L_n}\right) = \delta e^{-\alpha x_j}$$

Substituting Eq. 3.50 in the previous equation:

$$A\cosh\left(\frac{x_j}{L_n}\right) + \left[A\frac{S_n L_n}{D_n} - \delta L_n\left(\alpha + \frac{S_n}{D_n}\right)\right]\sinh\left(\frac{x_j}{L_n}\right) = \delta e^{-\alpha x_j}$$

One obtains:

$$A = \frac{\delta L_n\left(\alpha + \frac{S_n}{D_n}\right)\sinh\left(\frac{x_j}{L_n}\right) + \delta e^{-\alpha x_j}}{\cosh\left(\frac{x_j}{L_n}\right) + \frac{S_n L_n}{D_n}\sinh\left(\frac{x_j}{L_n}\right)} \tag{3.51}$$

At this point, A and B are known; hence, putting them into Eq. 3.47 it is possible to obtain:

$$n_p - n_{p0} = \left[\cosh\left(\frac{x}{L_n}\right) + \frac{S_n L_n}{D_n}\sinh\left(\frac{x}{L_n}\right)\right]\frac{\delta L_n\left(\alpha + \frac{S_n}{D_n}\right)\sinh\left(\frac{x_j}{L_n}\right) + \delta e^{-\alpha x_j}}{\cosh\left(\frac{x_j}{L_n}\right) + \frac{S_n L_n}{D_n}\sinh\left(\frac{x_j}{L_n}\right)} +$$
$$- \sinh\left(\frac{x}{L_n}\right)\left[\delta L_n\left(\alpha + \frac{S_n}{D_n}\right)\right] - \frac{\alpha F(1-R)\tau_n}{\alpha^2 L_n^2 - 1}e^{-\alpha x} \tag{3.52}$$

Bringing together the terms in $e^{-\alpha x_j}$, then considering the trigonometric formula:

$$\sinh\left(\frac{x_j - x}{L_n}\right) = \sinh\left(\frac{x_j}{L_n}\right)\cosh\left(\frac{x}{L_n}\right) - \cosh\left(\frac{x_j}{L_n}\right)\sinh\left(\frac{x}{L_n}\right)$$

Eq. 3.52 becomes:

$$n_p - n_{p0} = \delta\left[\frac{e^{-\alpha x_j}\left(\cosh\left(\frac{x}{L_n}\right) + \frac{S_n L_n}{D_n}\sinh\left(\frac{x}{L_n}\right)\right) + \sinh\left(\frac{x_j - x}{L_n}\right)\left(\alpha L_n + \frac{S_n L_n}{D_n}\right)}{\cosh\left(\frac{x_j}{L_n}\right) + \frac{S_n L_n}{D_n}\sinh\left(\frac{x_j}{L_n}\right)}\right] +$$
$$- \delta e^{-\alpha x} \tag{3.53}$$

Finally, considering Eq. 3.35, it is possible to obtain the electron photocurrent density along the emitter part of the solar cell:

$$J_n = qD_n\frac{\alpha F(1-R)\tau_n}{\alpha^2 L_n^2 - 1}\left[\frac{e^{-\alpha x_j}\left[\frac{1}{L_n}\sinh\left(\frac{x}{L_n}\right) + \frac{S_n}{D_n}\cosh\left(\frac{x_j}{L_n}\right)\right] - \cosh\left(\frac{x_j - x}{L_n}\right)\left(\alpha + \frac{S_n}{D_n}\right)}{\cosh\left(\frac{x_j}{L_n}\right) + \frac{S_n L_n}{D_n}\sinh\left(\frac{x_j}{L_n}\right)}\right] +$$
$$+ qD_n\frac{\alpha F(1-R)\tau_n}{\alpha^2 L_n^2 - 1}\alpha e^{-\alpha x} \tag{3.54}$$

3.2.2 *n*-type Base

In order to obtain the Hole photocurrent density in the base part of the solar cell, is necessary to repeat again the previous method with some changes.
By Eq. 3.20, for E=0:

$$J_p = -qD_p \frac{dp_n}{dx} \tag{3.55}$$

Let's substitute Eq. 3.55 into Eq. 3.33 obtaining the same equation of (3.37) in terms of $p_n - p_{n0}$. Solving it in the same way, the solution is:

$$p_n - p_{n0} = A\cosh\left(\frac{x}{L_p}\right) + B\sinh\left(\frac{x}{L_p}\right) - \frac{\alpha F(1-R)\tau_p}{\alpha^2 L_p^2 - 1}\mathrm{e}^{-\alpha x} \tag{3.56}$$

Again we must find out A and B coefficient based on the following boundary conditions (Fig. 3.16):

- from interface n-type base with depletion region:

$$p_n - p_{n0} = 0; \quad \text{for } x = x_j + W \tag{3.57}$$

- from surface recombination on the bottom side:

$$\frac{d(p_n - p_{n0})}{dx} = -\frac{S_p}{D_p}(p_n - p_{n0}); \quad \text{for } x = H \tag{3.58}$$

From Eq. 3.57:

$$A\cosh\left(\frac{x_j + W}{L_p}\right) + B\sinh\left(\frac{x_j + W}{L_p}\right) - \delta\mathrm{e}^{-\alpha(x_j+W)} = 0 \tag{3.59}$$

From Eq. 3.58:

$$\frac{A}{L_p}\sinh\left(\frac{x}{L_p}\right) + \frac{B}{L_p}\cosh\left(\frac{x}{L_p}\right) + \delta\alpha\mathrm{e}^{-\alpha x} = -\frac{S_p}{D_p}\left[A\cosh\left(\frac{x}{L_p}\right) + B\sinh\left(\frac{x}{L_p}\right) - \delta\mathrm{e}^{-\alpha x}\right] \tag{3.60}$$

The Eq 3.60 for $x = H$ yields:

$$A\left[\sinh\left(\frac{H}{L_p}\right) + \frac{S_p L_p}{D_p}\cosh\left(\frac{H}{L_p}\right)\right] = -B\left[\frac{S_p L_p}{D_p}\sinh\left(\frac{H}{L_p}\right) + \cosh\left(\frac{H}{L_p}\right)\right] + \\ + \delta\left(\frac{S_p L_p}{D_p} - \alpha L_p\right)\mathrm{e}^{-\alpha H} \tag{3.61}$$

In order to make the development of the equations easier, the following parameters are introduced:

- $\varepsilon = \sinh\left(\frac{H}{L_p}\right) + \frac{S_p L_p}{D_p}\cosh\left(\frac{H}{L_p}\right)$
- $\varphi = \frac{S_p L_p}{D_p}\sinh\left(\frac{H}{L_p}\right) + \cosh\left(\frac{H}{L_p}\right)$
- $\delta' = \delta\left(\frac{S_p L_p}{D_p} - \alpha L_p\right)$

With these parameters, the coefficient A is equal to:

$$A = \frac{-B\varphi + \delta' \mathrm{e}^{-\alpha H}}{\varepsilon} \tag{3.62}$$

Substituting Eq. 3.62 into Eq. 3.59:

$$B\varphi\cosh\frac{x_j + W}{L_p} - B\varepsilon\sinh\frac{x_j + W}{L_p} - \delta' \mathrm{e}^{-\alpha H}\cosh\frac{x_j + W}{L_p} = -\varepsilon\delta \mathrm{e}^{-\alpha(x_j + W)} \tag{3.63}$$

With the following thrigonometric formulas:

- $\varphi\cosh\frac{x_j + W}{L_p} = \frac{S_p L_p}{D_p}\sinh\left(\frac{H}{L_p}\right)\cosh\frac{x_j + W}{L_p} + \cosh\left(\frac{H}{L_p}\right)\cosh\frac{x_j + W}{L_p}$
- $-\varepsilon\sinh\frac{x_j + W}{L_p} = -\frac{S_p L_p}{D_p}\cosh\left(\frac{H}{L_p}\right)\sinh\frac{x_j + W}{L_p} - \sinh\left(\frac{H}{L_p}\right)\sinh\frac{x_j + W}{L_p}$

calling $H' = H - (x_j + W)$, Eq. 3.63 becomes:

$$B\left[\frac{S_p L_p}{D_p}\sinh\left(\frac{H'}{L_p}\right) + \cosh\frac{H'}{L_p}\right] = \delta' \mathrm{e}^{-\alpha H}\cosh\frac{x_j + W}{L_p} - \varepsilon\delta \mathrm{e}^{-\alpha(x_j + W)} \tag{3.64}$$

The coefficient B is:

$$B = \frac{\delta' \mathrm{e}^{-\alpha H}\cosh\left(\frac{x_j + W}{L_p}\right) - \varepsilon\delta \mathrm{e}^{-\alpha(x_j + W)}}{\chi} \tag{3.65}$$

where $\chi = \left[\frac{S_p L_p}{D_p}\sinh\left(\frac{H'}{L_p}\right) + \cosh\frac{H'}{L_p}\right] = \varphi\,\cosh\frac{x_j + W}{L_p} - \varepsilon\sinh\frac{x_j + W}{L_p}$

Considering again the coefficient A, put B into the Eq. 3.62:

$$A = \frac{-\varphi\delta' e^{-\alpha H}\cosh\frac{x_j+W}{L_p} + \varepsilon\delta\varphi \mathrm{e}^{-\alpha(x_j+W)} + \chi\delta'\mathrm{e}^{-\alpha H}}{\varepsilon\chi} \tag{3.66}$$

Let's simplify the previous expression considering the relationship between χ, φ and ε, hence A can be written as:

$$A = \frac{-\delta'\mathrm{e}^{-\alpha H}\sinh\frac{x_j+W}{L_p} + \delta\varphi\mathrm{e}^{-\alpha(x_j+W)}}{\chi} \tag{3.67}$$

Now, with A and B into Eq. 3.56:

$$\begin{aligned} p_n - p_{n0} = \cosh\left(\frac{x}{L_p}\right) & \frac{-\delta'\mathrm{e}^{-\alpha H}\sinh\left(\frac{x_j+W}{L_p}\right) + \delta\varphi\mathrm{e}^{-\alpha(x_j+W)}}{\chi} + \\ + \sinh\left(\frac{x}{L_p}\right) & \frac{\delta'\mathrm{e}^{-\alpha H}\cosh\left(\frac{x_j+W}{L_p}\right) - \varepsilon\delta\mathrm{e}^{-\alpha(x_j+W)}}{\chi} - \delta\mathrm{e}^{-\alpha x} \end{aligned} \tag{3.68}$$

Collect the common term $\mathrm{e}^{-\alpha(x_j+W)}$:

$$\begin{aligned} p_n - p_{n0} = \delta\mathrm{e}^{-\alpha(x_j+W)} & \left[\frac{-\cosh\left(\frac{x}{L_p}\right)\sinh\left(\frac{x_j+W}{L_p}\right)\left(\frac{S_pL_p}{D_p}-\alpha L_p\right)\mathrm{e}^{-\alpha H'} + \varphi\cosh\left(\frac{x}{L_p}\right)}{\chi}\right] + \\ + \delta\mathrm{e}^{-\alpha(x_j+W)} & \left[\frac{\sinh\left(\frac{x}{L_p}\right)\cosh\left(\frac{x_j+W}{L_p}\right)\left(\frac{S_pL_p}{D_p}-\alpha L_p\right)\mathrm{e}^{-\alpha H'} - \varepsilon\,\sinh\,\left(\frac{x}{L_p}\right)}{\chi}\right] + \\ - \delta\mathrm{e}^{-\alpha(x_j+W)}\mathrm{e}^{-\alpha(x-x_j-W)} & \end{aligned} \tag{3.69}$$

In order to simplify the previous expression, let's work on the two different parts of it. First of all:

$$\begin{aligned} -\cosh\left(\frac{x}{L_p}\right)\sinh\left(\frac{x_j+W}{L_p}\right)\left(\frac{S_pL_p}{D_p}-\alpha L_p\right)\mathrm{e}^{-\alpha H'} + \\ + \sinh\left(\frac{x}{L_p}\right)\cosh\left(\frac{x_j+W}{L_p}\right)\left(\frac{S_pL_p}{D_p}-\alpha L_p\right)\mathrm{e}^{-\alpha H'} \end{aligned}$$

can be simplified into:

$$\left(\frac{S_p L_p}{D_p} - \alpha L_p\right) \mathrm{e}^{-\alpha H'} \sinh\left(\frac{x-(x_j+W)}{L_p}\right)$$

The second part:

$$\varphi\cosh\left(\frac{x}{L_p}\right) - \varepsilon\sinh\left(\frac{x}{L_p}\right) = -\left[\sinh\left(\frac{H}{L_p}\right)\sinh\left(\frac{x}{L_p}\right) + \frac{S_p L_p}{D_p}\sinh\left(\frac{x}{L_p}\right)\cosh\left(\frac{H}{L_p}\right)\right] + \left[\cosh\left(\frac{H}{L_p}\right)\cosh\left(\frac{x}{L_p}\right) + \frac{S_p L_p}{D_p} sinh\left(\frac{H}{L_p}\right)\cosh\left(\frac{x}{L_p}\right)\right]$$

Considering $H = H' + x_j + W$, the previous expression can be simplified into:

$$\varphi\cosh\left(\frac{x}{L_p}\right) - \varepsilon\sinh\left(\frac{x}{L_p}\right) = \cosh\left(\frac{x-(H'+x_j+W)}{L_p}\right) + \frac{S_p L_p}{D_p}\sinh\left(\frac{-x+(H'+x_j+W)}{L_p}\right)$$

Let's analyze the two terms at the 2^{nd} member:

$$\cosh\left(\frac{x-(H'+x_j+W)}{L_p}\right) = \left[\cosh\left(\frac{x-x_j-W}{L_p}\right)\cosh\left(\frac{H'}{L_p}\right) + -\sinh\left(\frac{x-x_j-W}{L_p}\right)\sinh\left(\frac{H'}{L_p}\right)\right]$$

Based on the fact that the function $\sinh(y)$ is an odd function, so $\sinh(-y) = -\sinh(y)$:

$$\sinh\left(\frac{-x+(H'+x_j+W)}{L_p}\right) = -\sinh\left(\frac{x-(H'+x_j+W)}{L_p}\right)$$

we can write:

$$\sinh\left(\frac{-x+(H'+x_j+W)}{L_p}\right) = -\left[\sinh\left(\frac{x-(x_j+W)}{L_p}\right)\cosh\left(\frac{H'}{L_p}\right)\right] + \left[\cosh\left(\frac{x-(x_j+W)}{L_p}\right)\sinh\left(\frac{H'}{L_p}\right)\right]$$

With the previous expressions, we can rewrite:

$$\varphi\cosh\left(\frac{x}{L_p}\right)-\varepsilon\sinh\left(\frac{x}{L_p}\right)=cosh\left(\frac{x-x_j-W}{L_p}\right)\left[\frac{S_pL_p}{D_p}\sinh\left(\frac{H'}{L_p}\right)+\cosh\left(\frac{H'}{L_p}\right)\right]$$
$$-\sinh\left(\frac{x-x_j-W}{L_p}\right)\left[\frac{S_pL_p}{D_p}\cosh\left(\frac{H'}{L_p}\right)+\sinh\left(\frac{H'}{L_p}\right)\right]$$

With these simplifications Eq. 3.69 becomes:

$$p_n-p_{n0}=\frac{\alpha F(1-R)\tau_p}{\alpha^2L_p^2-1}\mathrm{e}^{-\alpha(x_j+W)}\left[\cosh\left(\frac{x-x_j-W}{L_p}\right)-\mathrm{e}^{-\alpha(x-x_j-W)}\right]+$$
$$-\frac{\alpha F(1-R)\tau_p}{\alpha^2L_p^2-1}\mathrm{e}^{-\alpha(x_j+W)}\left[\frac{\frac{S_pL_p}{D_p}\left[\cosh\frac{H'}{L_p}-\mathrm{e}^{-\alpha H'}\right]+\sinh\frac{H'}{L_p}+\alpha L_p\mathrm{e}^{-\alpha H'}}{\cosh\left(\frac{H'}{L_p}\right)+\frac{S_pL_p}{D_p}\sinh\left(\frac{H'}{L_p}\right)}\sinh\frac{x-x_j-W}{L_p}\right] \tag{3.70}$$

Considering the Eq. 3.55, it is possible to obtain the hole photocurrent density:

$$J_p=-qD_p\frac{\alpha F(1-R)\tau_p}{\alpha^2L_p^2-1}\mathrm{e}^{-\alpha(x_j+W)}\left[\frac{1}{L_p}\sinh\left(\frac{x-x_j-W}{L_p}\right)+\alpha\mathrm{e}^{-\alpha(x-x_j-W)}\right]+$$
$$+qD_p\frac{\alpha F(1-R)\tau_p}{\alpha^2L_p^2-1}\mathrm{e}^{-\alpha(x_j+W)}\left[\frac{\frac{S_pL_p}{D_p}\left[\cosh\frac{H'}{L_p}-\mathrm{e}^{-\alpha H'}\right]+\sinh\frac{H'}{L_p}+\alpha L_p\mathrm{e}^{-\alpha H'}}{\cosh\left(\frac{H'}{L_p}\right)+\frac{S_pL_p}{D_p}\sinh\left(\frac{H'}{L_p}\right)}\right]$$
$$\mathrm{x}\left[\frac{1}{L_p}\cosh\frac{x-x_j-W}{L_p}\right] \tag{3.71}$$

In order to have a complete model, it is necessary to consider also the photogeneration of carriers that takes place into the *depletion region* (see Fig. 3.12 and Fig. 3.16). In fact, photons not only create *e-h* pairs in the *n*-region and *p*-region, but also into the depletion one. In this region, the electric field is high enough that *e-h* pairs photogenerated are swept out of the depletion region before they can recombine [14]. Hence, the electron and hole pairs can be collected are equal to the number of photons absorbed. Hence, considering Eq. 3.4, the equation of the generated photocurrent into the depletion region can be written as:

$$J_{dr}=qF(1-R)\mathrm{e}^{-\alpha(x_j)}\left(1-e^{-\alpha W}\right) \tag{3.72}$$

At this point, we have three equations able to describe the generated photocurrent along the entire solar cell device: Eq. 3.54 for p-type emitter, Eq. 3.72 for the depletion region, Eq. 3.71 for n-type base.

3.3 Single Junction solar cells: Simulations

In the previous section we have obtained a model able to characterize a p-n solar cell. Obviously the same model can be used for a n-p solar cell with the same boundary conditions remembering that in the emitter the minority charges will be holes and in the base will be electrons. Now, in order to appreciate some physical aspects, let's simulate a p-n solar cell in GaAs.

3.3.1 GaAs solar cell: concentration profile and photocurrent

Following we will explore the trend of the minority carriers along the device and then the total photocurrent carried by them. As we have seen in Section 3.1.2, GaAs absorbs up to $\lambda = 870$ nm, so let's consider two different wavelengths:

- $\lambda = 400$ nm
- $\lambda = 750$ nm

Based on the selected λ, the absorption coefficient α and the reflectance R have different values:

λ [nm]	α [cm^{-1}]	R
400	6.7 x 10^5	0.48
750	1.88 x 10^4	0.33

From the table, for $\lambda = 400$ nm the absorption coefficient $\alpha(\lambda)$ is greater than that for $\lambda = 750$ nm. The propagation of the waves, along the device, is attenuated as a decreasing exponential leading to a greater absorption near the front surface; opposite behavior for an increasing λ.
In order to plot the concentration profile of the minority carriers along the device, we consider a solar cell with the following parameters (taken from [14]):

x_j	W	H	D_p	D_n	τ_p	τ_n	N_E	N_B
[μm]	[μm]	[μm]	$\left[\frac{cm^2}{s}\right]$	$\left[\frac{cm^2}{s}\right]$	[s]	[s]	[cm^{-3}]	[cm^{-3}]
0.5	0.09	10	5.7	32.4	1.58 x 10^{-8}	1 x 10^{-9}	2 x 10^{19}	2 x 10^{17}

From the table we obtain L_n=1.8 μm and L_p=3 μm.
For the emitter part let's analyze the concentration profile of the excess minority carriers $n_p - n_{p0}$. The Eq. 3.53 is based on two different boundary conditions (Eq. 3.48 , Eq. 3.49); this means that in the point $x = x_j$, at the interface with the depletion region, we should expect $n_p - n_{p0} = 0$ and for $x = 0$ we should observe the effect of the surface recombination phenomena.
In order to appreciate it, Fig. 3.17 and Fig. 3.18 show several concentration profiles for different values of recombination velocity S_n.

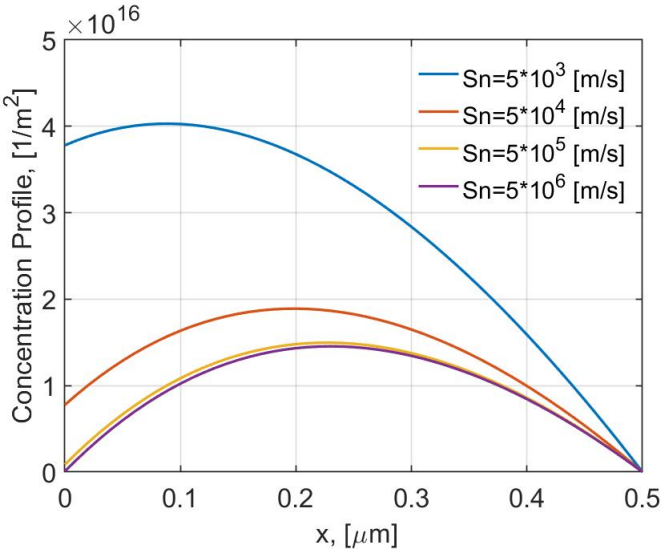

Figure 3.17: electrons concentration in the p-emitter for $\lambda = 750\,\mathtt{nm}$.

By the previous plot we can confirm that:

- at the interface p-emitter/depletion region the concentration profile $n_p - n_{p0} = 0$;
- for $x = 0$, at the surface, changing the value of S_n the profile $n_p - n_{p0}$ is different. In fact, increasing S_n the electron minority carrier concentration decreases. We will see that the value of the recombination velocity has an important impact on the photogenerated current.

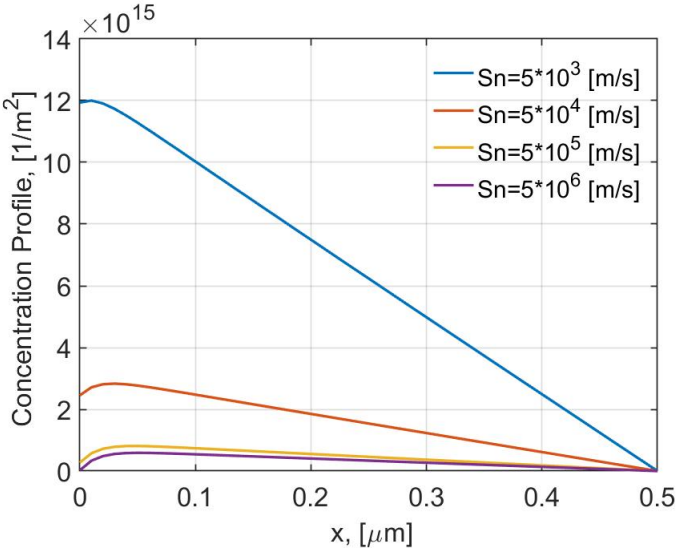

Figure 3.18: electrons concentration in the p-emitter for $\lambda = 400\,\mathtt{nm}$

For $\lambda = 400\mathtt{nm}$ (Fig. 3.18) we can note the same behavior at the interface and for $x = x_j$. Instead, in the middle part of the emitter, the concentration profile for the

two wavelengths is different given by the fact that the Generation rate changes with λ and x.
In order to understand how much the surface recombination influences the performance of the solar cell let's consider the diffusion current density for the minority carriers based on equations (3.54) and (3.71).
For $\lambda = 750$ nm and $S_n = 10^6 \left[\frac{\text{m}}{\text{s}}\right]$ we obtain the following plot:

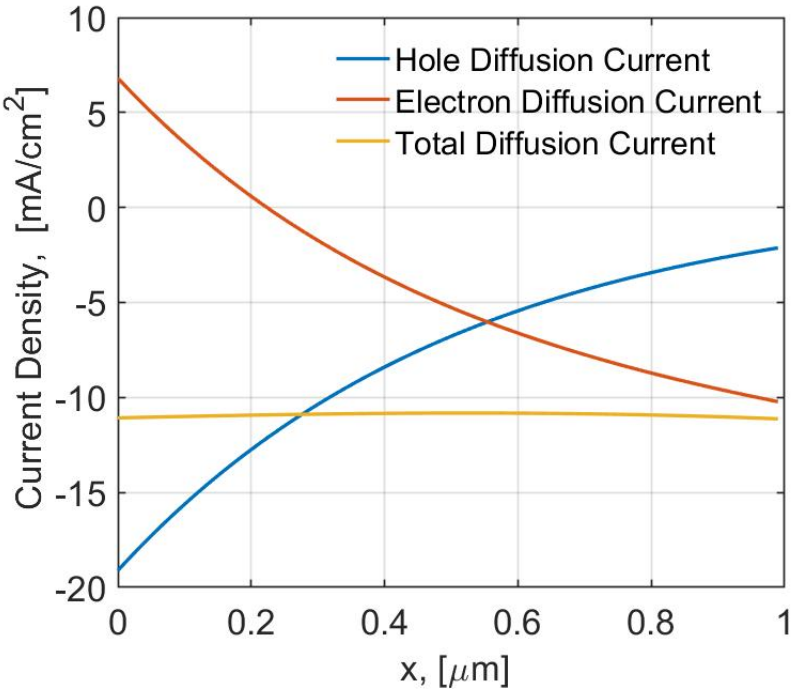

Figure 3.19: Hole and Electron Current Density for $\lambda = 750\,\text{nm}$.

In Fig. 3.19:

- for $x < 0.2\,\mu\text{m}$, the electron diffusion current is positive, produced by the diffusion of the minority charges to the front section of the solar cell because of the surface recombination. Greater S_n, greater will be the net rate of the electron diffusion current that decrease negatively the total diffusion current. In this case J_{TOT} will be lower than that obtained for a small S_n. Hence, S_n has a key role in the rate of the total diffusion photocurrent.
  Summing up, a small S_n means a greater concentration of electrons n_p able to reach the n-base through Diffusion phenomena.
  Also, in this region, by the plot, we can note that the electron diffusion current is compensated by the excess of photogenerated holes, so the total diffusion current is close to the hole diffusion current J_p;

- for $x > 0.5\,\mu\text{m}$ going towards the n-region the total current density J_{TOT} is close to J_n. In the back surface of the solar cell, in this case, the surface recombination

phenomena has a lower impact than that of the front surface, so holes go through Diffusion phenomena to p-emitter.

For $\lambda = 400$ nm and $S_n = 10^6 \left[\frac{\text{m}}{\text{s}}\right]$ we obtain the following plot:

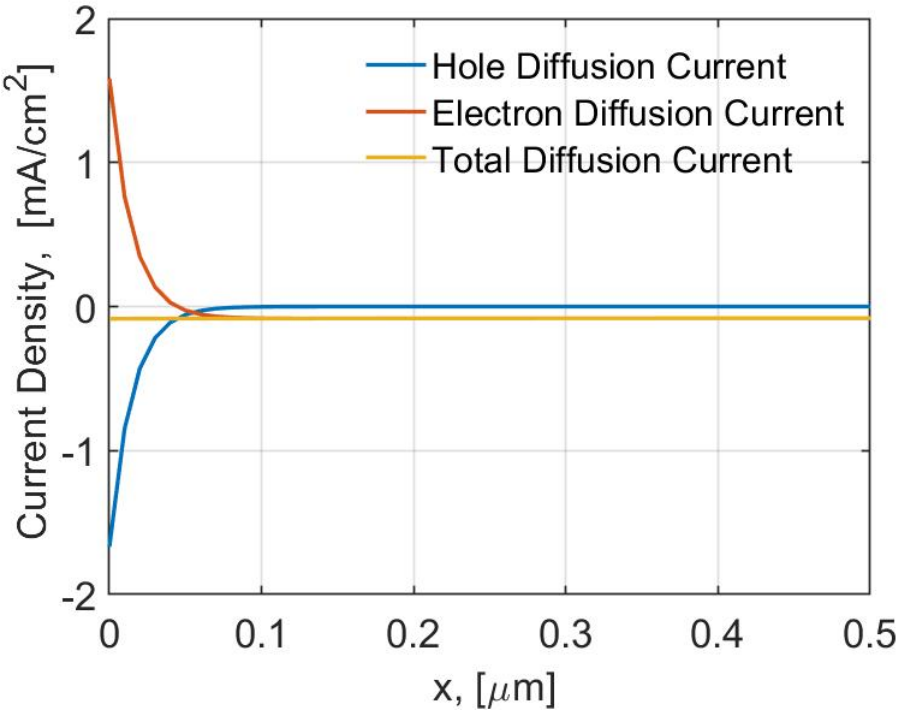

Figure 3.20: Hole and Electron Current Density for $\lambda = 400\,\text{nm}$

If we put in comparison Fig. 3.20 with Fig. 3.19, we note that the only difference is that for $\lambda = 400$ nm most photons are absorbed near the surface contact, so the photogenerated electrons suffer more the recombination phenomena.
In fact, for $x < 0.05\,\mu\text{m}$ the J_n is relatively high and the diffusion current J_p cannot compensate it as in the case for $\lambda = 750$ nm, so the amount of the diffusion photocurrent is small.
The previous plots give us an idea of the impact of the surface recombination on the performance of the solar cell. In fact, if the generated photocurrent is small, the Power extracted by the solar cell decreases leading to a lower efficiency.
We have said that in order to decrease the amount of losses linked to the Surface Recombination there was the possibility of using several technique such us passivation of the dangling bonds leading to a very small values of S. Now, we should simulate this situation forcing $S_n = 1$ and $S_p = 1$. This is an ideal case, but it is very important in order to understand the bad impact of this kind of recombination on the photocurrent.

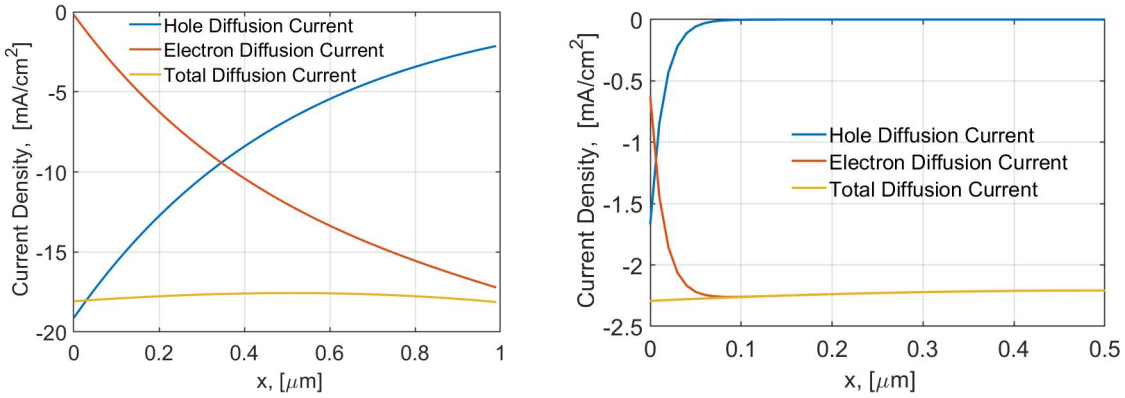

Figure 3.21: Diffusion Current for $\lambda = 750\texttt{nm}$ on the left, Diffusion Current for $\lambda = 400\texttt{nm}$ on the right; $S_n = 1$ and $S_p = 1$ for both cases.

From Fig. 3.21, in both cases, the total diffusion photocurrent value is near to the ideal photogenerated current. In order to better understand how much the performances of a solar cell are linked to the Surface Recombination we will study in the following section the EQE (External Quantum Efficiency) of a n-p solar cell.

3.3.2 GaAs solar cell: EQE

The aim of this Section is studying the behavior of the solar cell at each wavelength of the solar spectrum. Considering that at each wavelength the number of incident photons is different, we want to understand how many of those photons create e-h pairs that can be collected.
The amount of e-h generated with respect to the number of incident photons is called EQE: External Quantum Efficiency [14].

$$EQE = \frac{J_n}{qF} + \frac{J_p}{qF} + \frac{J_{dr}}{qF} \tag{3.73}$$

First, let's consider the p-n solar cell of Fig. 3.16 with the parameters used before. If we put Eq. 3.54, Eq. 3.71, calculated for $x = x_j$ and $x = x_j + W$ respectively, and Eq. 3.72 into Eq. 3.73, the EQE is shown in Fig. 3.22. From Fig.3.22 we can see that the p-emitter part is able to absorb around 31 % of the total solar irradiance for $\lambda <$ 430 $\texttt{nm}$; this small value of EQE is given by the value of Surface Recombination equal to $S_n = S_p = 5\,\text{x}10^3\ \left[\frac{\texttt{m}}{\texttt{s}}\right]$. Increasing the value of λ the total EQE increases thanks to the photons also absorbed into the depleted region and into the n-base, instead the amount of photons collected by the emitter decreases for high wavelength ($\lambda > 600\ \texttt{nm}$) because of its width. Then, for $\lambda >$870 $\texttt{nm}$ the absorption of the photons is zero and so the EQE decreases quickly.

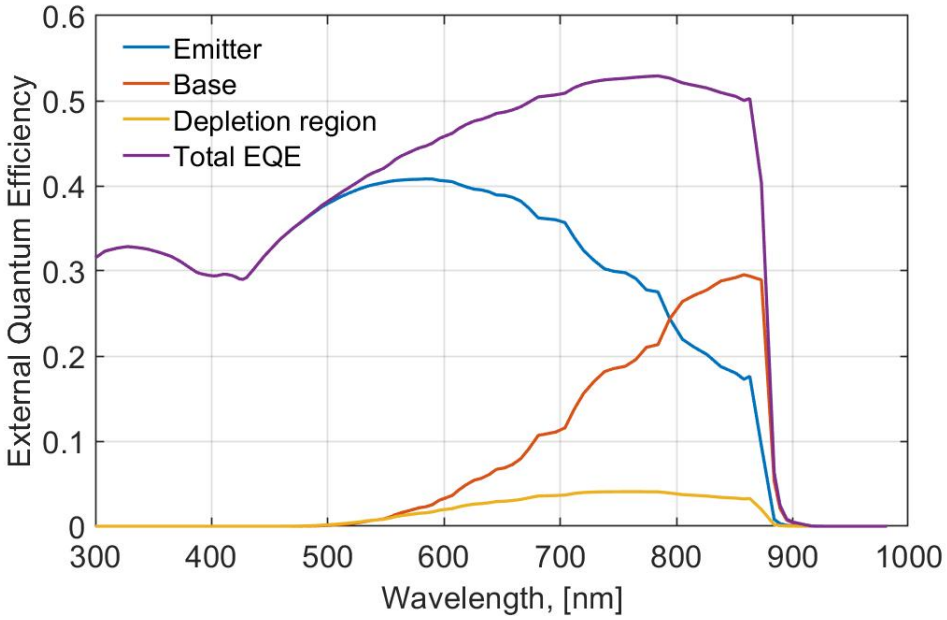

Figure 3.22: EQE for p-n GaAs solar cell.

Now, we will study the Spectral Response of a *n-p* solar cell comparing the obtained results with that of the Lumb article [16]. Consider the reference structure (Fig. 3.23) and the table with some parameters used for the simulation.

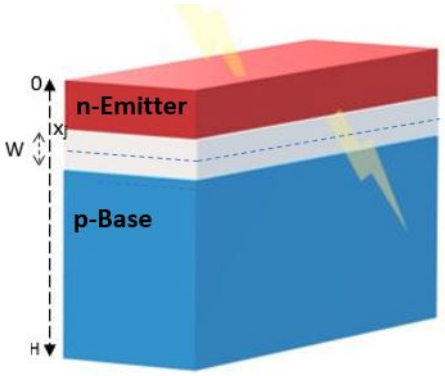

Figure 3.23: n-p GaAs solar cell

x_j [nm]	H [nm]	S_n $\left[\frac{\text{m}}{\text{s}}\right]$	S_p $\left[\frac{\text{m}}{\text{s}}\right]$	N_E $\left[\frac{1}{\text{cm}^3}\right]$	N_B $\left[\frac{1}{\text{cm}^3}\right]$
100	1300	5 x 10^3	5 x 10^3	5 x 10^{17}	5 x 10^{16}

In Lumb's article, lifetime of the minority charges is obtained with the following parameters:

- radiative lifetime $\tau_r = B_{rad}N$ where N is the doping concentration in the considered region, instead B_{rad} is the bimolecular recombination coefficient, or B-coefficient.
  This last one changes based on the doping concentration, but, in this case, the value is $B_{rad} = 2.86 \text{ x } 10^{-10} \left[\frac{\mathtt{cm}^3}{\mathtt{s}}\right]$
- Shockley-Read-Hall lifetime $\tau_{SRH} = 20\mathtt{ns}$ in both emitter and base region.

The total carrier lifetime can be obtained from Eq. 3.74 where the Auger recombination phenomena is neglected respect to Eq. 3.12:

$$\frac{1}{\tau} = \frac{1}{\tau_{SRH}} + \frac{1}{\tau_r} \tag{3.74}$$

Considering that $L_n = \sqrt{D_n\tau_n}$ and $L_p = \sqrt{D_p\tau_p}$, it is necessary to obtain the Diffusion coefficients D_n and D_p where: $D_n = \dfrac{\mu_n KT}{q}$ and $D_p = \dfrac{\mu_p KT}{q}$.

In order to obtain D_n and D_p similar to that of the Lumb's article, we have used the approximated values of mobility μ_n and μ_p of the reference article [19]:

- $D_p = 3.88 \left[\frac{\mathtt{cm}^2}{\mathtt{s}}\right]$
- $D_n = 207 \left[\frac{\mathtt{cm}^2}{\mathtt{s}}\right]$
- $L_n = 0.103 \, [\mu\mathtt{m}]$
- $L_p = 2.45 \, [\mu\mathtt{m}]$

Eq. 3.54 and Eq. 3.71 can be rewritten for the case of n-p GaAs solar cell, considering that what has been said about the p-n solar cell is also valid for a solar cell whose n-region is exposed to the solar spectrum. For a n-p solar cell the equations linked to the diffusion photocurrent of the minority carriers, calculated for $x = x_j$ and $x = x_j + W$ respectively for J_p and J_n are:

$$J_p = q\frac{\alpha F(1-R)L_p}{\alpha^2 L_p^2 - 1}\left[\frac{\mathrm{e}^{-\alpha x_j}\left(-\sinh\left(\frac{x_j}{L_p}\right) - \frac{S_p L_p}{D_p}\cosh\left(\frac{x_j}{L_p}\right)\right) + \left(\alpha L_p + \frac{S_p L_p}{D_p}\right)}{\cosh\left(\frac{x_j}{L_p}\right) + \frac{S_p L_p}{D_p}\sinh\left(\frac{x_j}{L_p}\right)} - \alpha L_p \mathrm{e}^{-\alpha x_j}\right] \tag{3.75}$$

$$J_n = q\frac{\alpha F(1-R)\text{Ł}_n}{\alpha^2 L_n^2 - 1}\mathrm{e}^{-\alpha(x_j+W)}\left[L_n\alpha - \frac{\frac{S_n L_n}{D_n}\left[\cosh\frac{H'}{L_n} - \mathrm{e}^{-\alpha H'}\right] + \sinh\frac{H'}{L_n} + \alpha L_n \mathrm{e}^{-\alpha H'}}{\cosh\left(\frac{H'}{L_n}\right) + \frac{S_n L_n}{D_n}\sinh\left(\frac{H'}{L_n}\right)}\right] \tag{3.76}$$

Let's consider the n-p solar cell (Fig. 3.23) based on the Lumb article.
The EQE obtained for this kind of solar cell is the following:

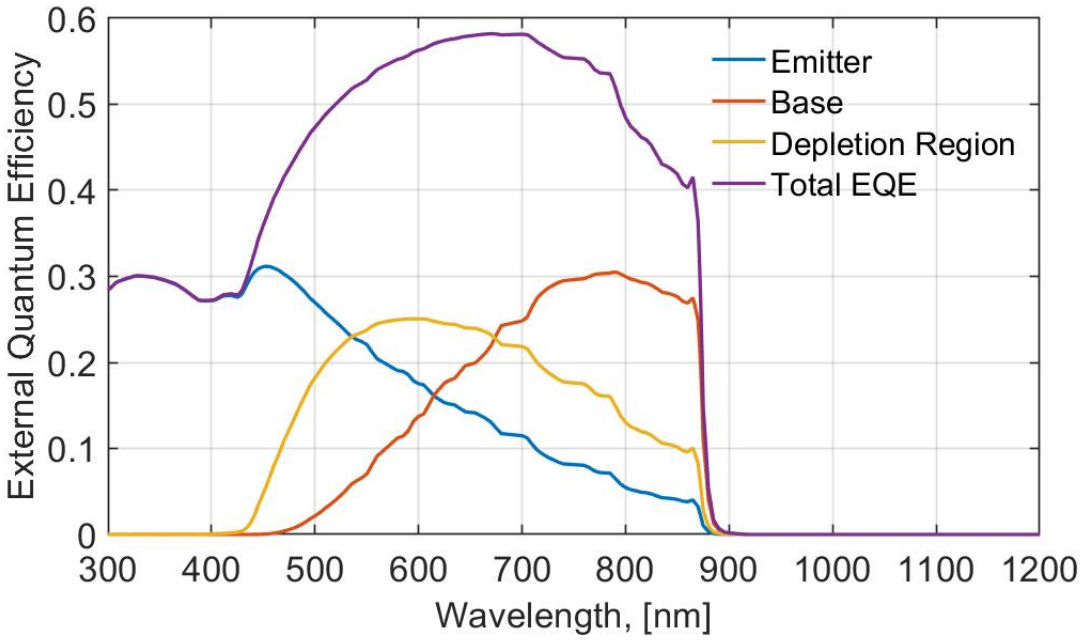

Figure 3.24: EQE for n-p GaAs solar cell.

From Fig. 3.24 we can see that the n-emitter part is able to absorbs a 30 % of the total solar irradiance for $\lambda < 450$ nm; this small value of EQE is given by the value of Surface Recombination but also by the high reflectance in this part of the spectra (Fig. 3.2). Hence, also, the reflectance is an important problem for a performance of a solar cell.
Increasing the value of λ, photons are absorbed into the depleted region and into the p-base, instead the amount of photons collected by the emitter decreases for high wavelength because of its small width. Then, for λ >870 nm the absorption of the photons is zero and so the EQE decreases quickly.
Fig. 3.25 puts in comparison the total EQE obtained from the simulation and that of the Lumb model. The blue line is the EQE obtained by our simulation, instead the black line is taken from Lumb article. There is a good qualitative agreement, with some minor quantitative discrepancy possibly done to the different optical model and mobility models.

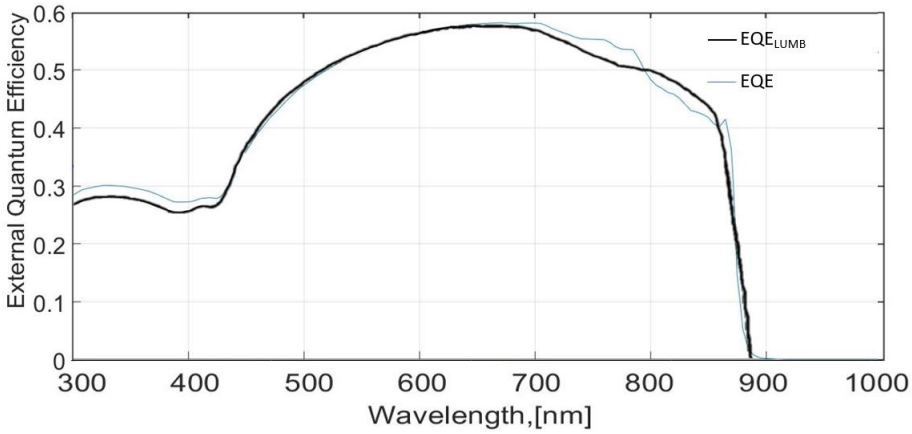

Figure 3.25: Comparison between the EQE obtained from the simulation and that one reported in the Lumb article.

3.3.3 GaAs solar cell: influence of the Surface Recombination on EQE

In the previous discussion we have observed the influence of the Surface Recombination on the electrons and holes photocurrent (Fig. 3.21). Now, considering the n-p solar cell of Fig. 3.23, we want to see the impact of surface recombination on the EQE, changing the value of S_n, referred to the bottom side, and S_p, referred to the top side of the solar cell. We will see, based on the value of S_n how much the efficiency may decrease and we will compare it with the efficiency lost changing S_p.
In the following simulations the values of the electrons and holes mobility are obtained with the method exposed in the sub-section 3.1.6.
First, growing up S_n, the EQE has the following variations:

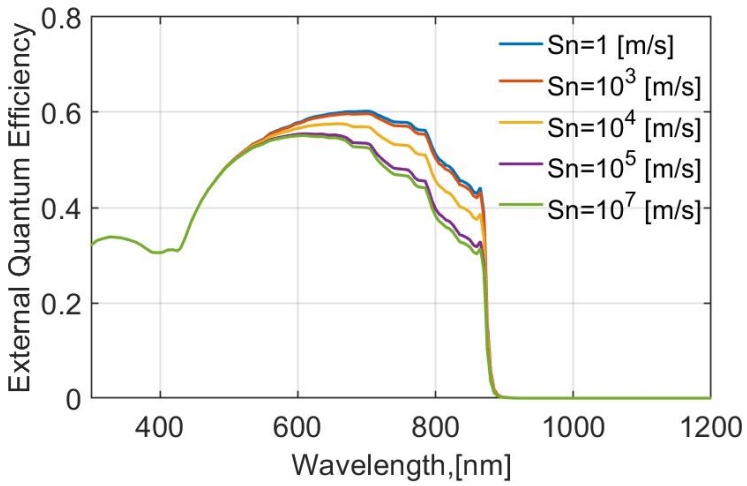

Figure 3.26: EQE(S_n).

Increasing S_n (Fig. 3.26) there is a decreasing of the EQE for $\lambda > 600\,\mathtt{nm}$; in this case, the surface recombination interests the back surface that absorbs photons with high wavelengths.
Changing the value of S_p, the EQE will be:

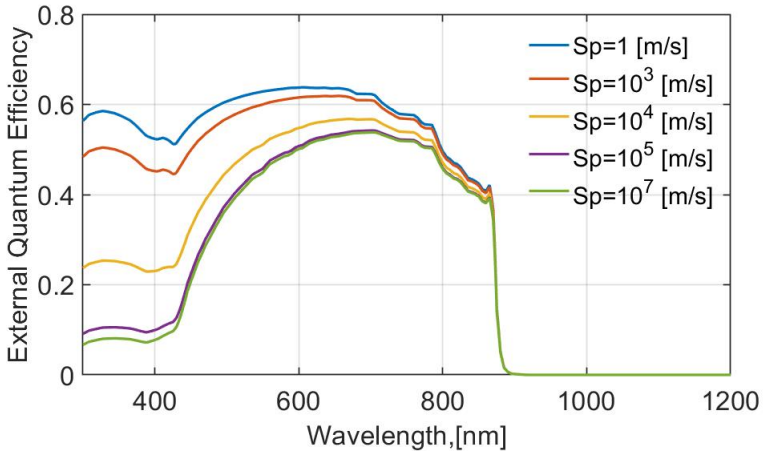

Figure 3.27: EQE(S_p).

From Fig. 3.27 we have the opposite case. In fact, we can see there is a decrease of the EQE for $\lambda < 450\,\mathtt{nm}$.
Decreasing or growing up S_n or S_p the alterations on the EQE are not negligible.
In order to quantize the variation of the EQE, we consider an ideal case for the EQE with $S_n = 1$ and then for $S_p = 1$. Hence, it is possible to obtain the Efficiency Losses (E.L.), in percentage, of the EQE respect to the ideal case.
Changing S_n the Efficiency Losses will be:

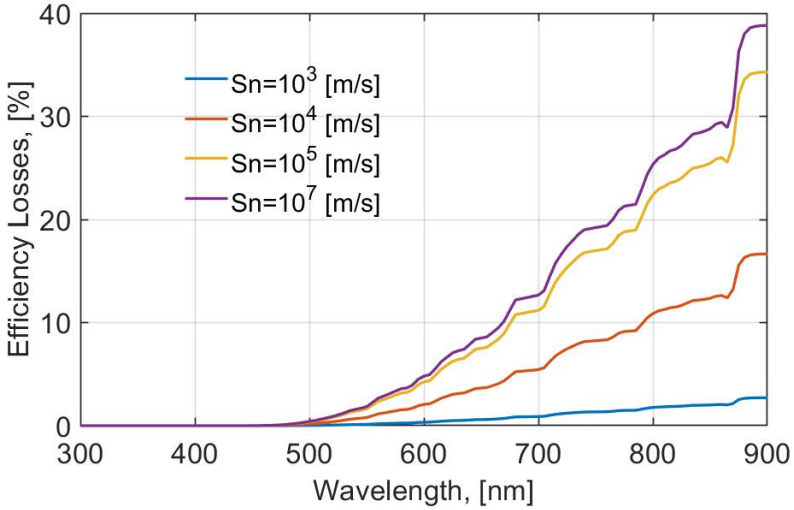

Figure 3.28: Efficiency losses(S_n).

Changing S_p:

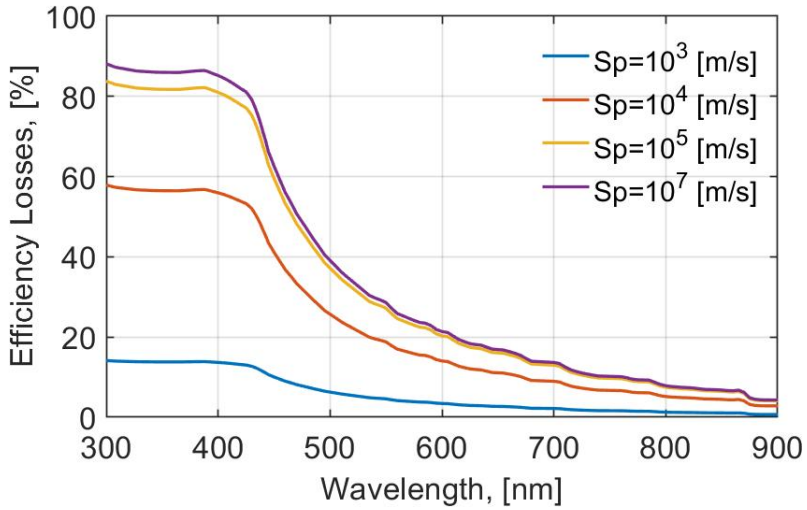

Figure 3.29: Efficiency losses(S_p).

The worst case is for $S_n = 10^7 \left[\frac{\mathrm{m}}{\mathrm{s}}\right]$ (Fig. 3.28) and for $S_p = 10^7 \left[\frac{\mathrm{m}}{\mathrm{s}}\right]$ (Fig. 3.29). By the two plots it is possible to observe that for the values of S_n and S_p up to $10^3 \left[\frac{\mathrm{m}}{\mathrm{s}}\right]$ there are low efficiency losses, around 3 % and 12 % respectively. Putting in comparison the two cases, although S_p has a greater negative influence in a n-p GaAs solar cell, it is necessary working on both S_p and S_n in order to have good performances.

3.3.4 GaAs solar cell: influence of the Surface Recombination and Carrier Lifetime on the Saturation current

From Section 3.2 we have obtained the equations linked to the generated photocurrent. In the previous sections we have seen also the Surface Recombination effect on the photocurrent density and on the EQE.
We know that the photocurrent is not the only current component travelled along the device; in fact, there is also the component of "Dark current" that exists also when the junction is not under illumination. The Dark current aims to decrease the total current collected at the terminals of the device, in fact it is opposite in direction to the photocurrent. Now, we apply the drift-diffusion equations for the case of non-illumination in order to find the Dark component. We consider only the "Injected current" created by the electrons injected from the n-side to the p-side and opposite for the holes. It is anticipated that the simulations in this Section are based on the parameters shown in the Section 3.3.2.

Equations of the Dark current Let's consider the equations of the minority carriers without the term of Generation rate because of the hypothesis of "not illumination" .
Considering the structure of Fig. 3.23, the starting equations are:

for the *n-emitter region*

$$\frac{1}{q}\left(\frac{dJ_p}{dx}\right)+\frac{p_n-p_{n0}}{\tau_p}=0 \tag{3.77}$$

for the *p-base region*

$$\frac{1}{q}\left(\frac{dJ_n}{dx}\right)+\frac{n_p-n_{p0}}{\tau_n}=0 \tag{3.78}$$

The general solutions are, respectively:

$$p_n-p_{n0}=A\cosh\left(\frac{x}{L_p}\right)+B\sinh\left(\frac{x}{L_p}\right) \tag{3.79}$$

$$n_p-n_{p0}=A\cosh\left(\frac{x}{L_n}\right)+B\sinh\left(\frac{x}{L_n}\right) \tag{3.80}$$

Again we must find out A and B coefficient for each equation. In order to obtain the complete solution of the Eq. 3.79 the boundary conditions are:

$$\frac{d(p_n-p_{n0})}{dx}=\frac{S_p}{D_p}(p_n-p_{n0});\quad \text{for } x=0 \tag{3.81}$$

$$p_n=p_{n0}\mathrm{e}^{\left(\frac{qV_d}{kT}\right)};\quad \text{for } x=x_j \tag{3.82}$$

In order to obtain the complete solution of the Eq. 3.80 the boundary conditions are:

$$n_p=n_{p0}\mathrm{e}^{\left(\frac{qV_d}{kT}\right)};\quad \text{for } x=x_j+W \tag{3.83}$$

$$\frac{d(n_p-n_{p0})}{dx}=-\frac{S_n}{D_n}(n_p-n_{p0});\quad \text{for } x=H \tag{3.84}$$

where V_d is the voltage across the device, in this case, generated by the incident light. Considering the previous boundary equations, the complete solution for the n-emitter region, for $x=x_j$ is :

$$J_{pdark}=-qD_p\frac{ni^2}{N_D}\frac{1}{L_p}\left[\frac{\sinh\left(\frac{x_j}{L_p}\right)+\frac{S_pL_p}{D_p}\cosh\left(\frac{x_j}{L_p}\right)}{\cosh\left(\frac{x_j}{L_p}\right)+\frac{S_pL_p}{D_p}\sinh\left(\frac{x_j}{L_p}\right)}\right]\left(\mathrm{e}^{\left(\frac{qV_d}{KT}\right)}-1\right) \tag{3.85}$$

for the p-base, in the point $x = x_j + W$:

$$J_{ndark} = -qD_n \frac{ni^2}{N_A} \frac{1}{L_n} \left[\frac{\sinh\left(\frac{H'}{L_n}\right) + \frac{S_n L_n}{D_n} \cosh\left(\frac{H'}{L_n}\right)}{\cosh\left(\frac{H'}{L_n}\right) + \frac{S_n L_n}{D_n} \sinh\left(\frac{H'}{L_n}\right)} \right] \left(e^{\left(\frac{qV_d}{KT}\right)} - 1 \right) \tag{3.86}$$

where $H' = H - (x_j + W)$.
Eq. 3.85 can be rewritten as:

$$J_{pdark} = J_{p0} \left(1 - e^{\left(\frac{qV_d}{KT}\right)} \right) \tag{3.87}$$

and the Eq. 3.86 as:

$$J_{ndark} = J_{n0} \left(1 - e^{\left(\frac{qV_d}{KT}\right)} \right) \tag{3.88}$$

Now, the aim is to explore the influence of S_p, S_n and of the carrier lifetime τ_p, τ_n on the saturation current density components J_{p0}, J_{n0} respectively. In Eq. 3.85 and Eq. 3.86 we can note that the transport of minority carriers depend also on the diffusion length $L_p = \sqrt{D_p \tau_p}$ and $L_n = \sqrt{D_n \tau_n}$.

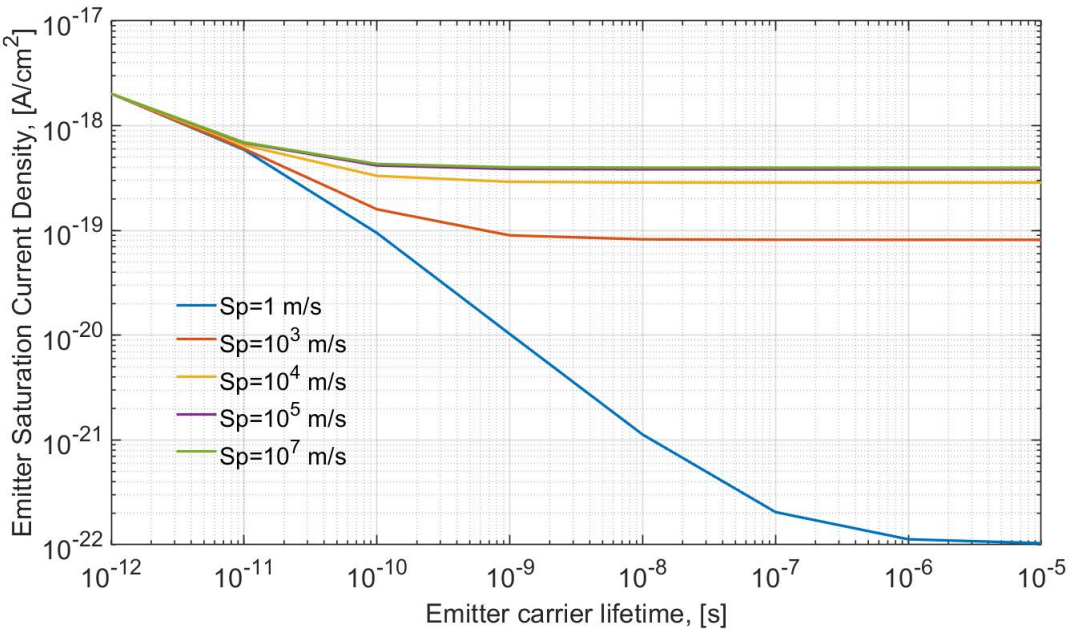

Figure 3.30: Saturation current density J_{p0} versus minority carrier lifetime τ_p considering values of recombination velocities S_p in the range $[10^0 \div 10^7]$ $\left[\frac{\mathrm{m}}{\mathrm{s}}\right]$.

Fig. 3.30 investigates the effect of the surface recombination velocity S_p on J_{p0} considering also different values of carrier lifetime τ_p. We can note that increasing S_p,

the value of J_{p0} increases of several orders of magnitude respect to the ideal case for $S_p = 1 \left[\frac{\mathtt{m}}{\mathtt{s}}\right]$ for high carrier lifetimes. Instead, the effect of the surface recombination velocity is irrelevant considering short carrier lifetimes.

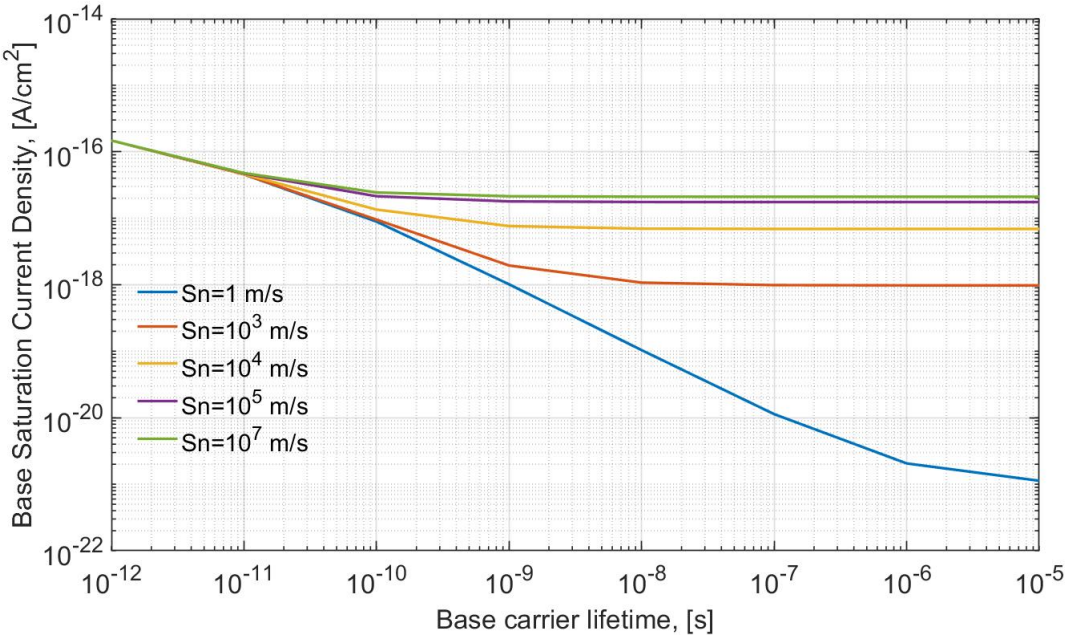

Figure 3.31: Saturation current density J_{n0} versus minority carrier lifetime τ_n considering values of recombination velocities S_n in the range $[10^0 \div 10^7] \left[\frac{\mathtt{m}}{\mathtt{s}}\right]$.

In the p-base region, Fig. 3.31 investigates the effect of S_n on J_{n0} considering carrier lifetime τ_n in the range of $[10^{-12} \div 10^{-5}]$ $\mathtt{s}$. We can note that the qualitative behavior of the saturation current J_{n0} is the same of that of J_{p0} in Fig. 3.30.
We know, from Chapter 2, that the Dark current component shall be taken into consideration when calculating the open circuit voltage V_{oc} in order to obtain the J-V characteristic and the total efficiency η. Hence, the value of the saturation current influences the total power that the solar cell can deliver to the external load.
In the next Section we will observe also the behavior of the V_{oc} versus the Saturation current.

3.3.5 GaAs solar cell: J-V characteristic

In Section 1.4 we have introduced the concept of Dark Current and Photocurrent calculating them with the *Shokley-Queisser model*, then showing the J-V characteristic. Now we want to obtain the characteristic of a solar cell based on the Hovel model. Hence, let's consider the n-p GaAs solar cell of Fig. 3.23 and put Eq. 3.72, Eq. 3.75, Eq. 3.76, Eq. 3.85 and Eq. 3.86 into Eq. 3.89. The total current is given by:

$$J = J_n + J_p + J_{dr} + J_{pdark} + J_{ndark} \tag{3.89}$$

In order to obtain the J-V characteristic it is necessary to find the open circuit Voltage V_{oc}.
Calling $J_{ph} = J_n + J_p + J_{dr}$, Eq. 3.89 becomes:

$$J = J_{ph} + (J_{p0} + J_{n0}) \left[1 - \mathrm{e}^{\left(\frac{qV_d}{KT}\right)} \right] \tag{3.90}$$

It is necessary to put the total current J equal to zero. Hence, Eq. 3.90 yields to:

$$V_{oc} = \left(\frac{kT}{q} \right) \ln \left(\frac{J_{ph} + J_o}{J_o} \right) \tag{3.91}$$

where $J_0 = J_{p0} + J_{n0}$.

Influence of the Surface Recombination and Carrier Lifetime on the open circuit voltage From Eq. 3.91 we can deduce that the V_{oc} depends on the value of photocurrent J_{ph} and saturation current J_0. Although quantitatively the relationship between the two current components is $J_{ph} \gg J_0$ (see Fig. 3.21 and Fig. 3.31), the effect of J_0 is significant for the value of the open circuit voltage V_{oc}. On the basis of these considerations Fig. 3.32 shows the V_{oc} as a function of carrier lifetime and surface recombination velocity.

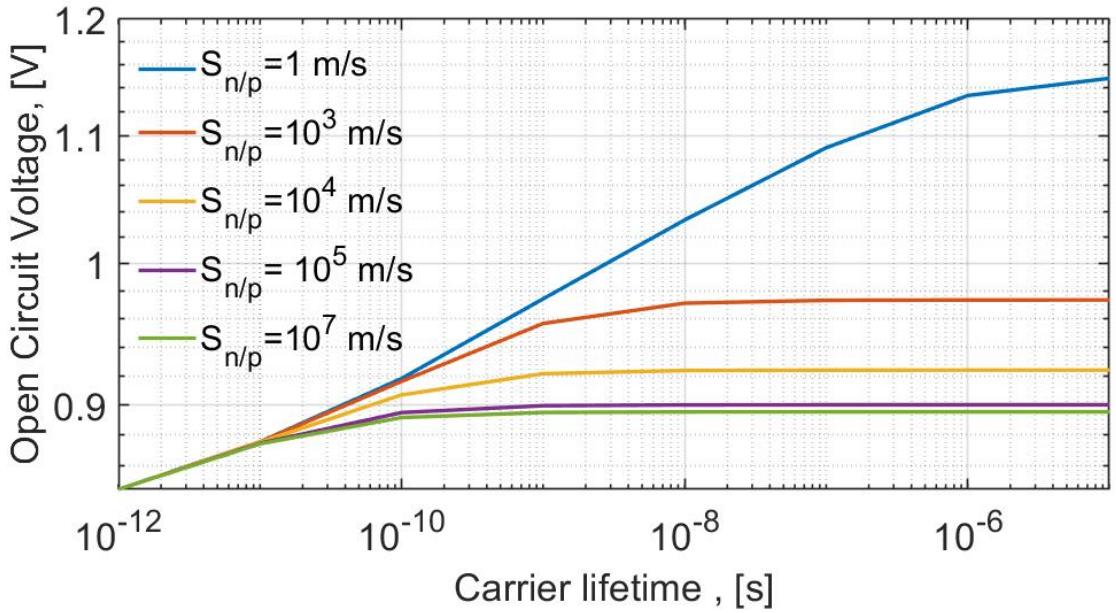

Figure 3.32: Open circuit voltage V_{oc} as a function of minority carrier lifetime. We assume $\tau_p = \tau_n$ considering values of recombination velocities $S_n = S_p$ in the range $[10^0 \div 10^7] \frac{\mathrm{m}}{\mathrm{s}}$.

From Fig. 3.32 we can note that V_{oc} gets smaller decreasing the value of the carrier lifetime or increasing the surface recombination velocity.

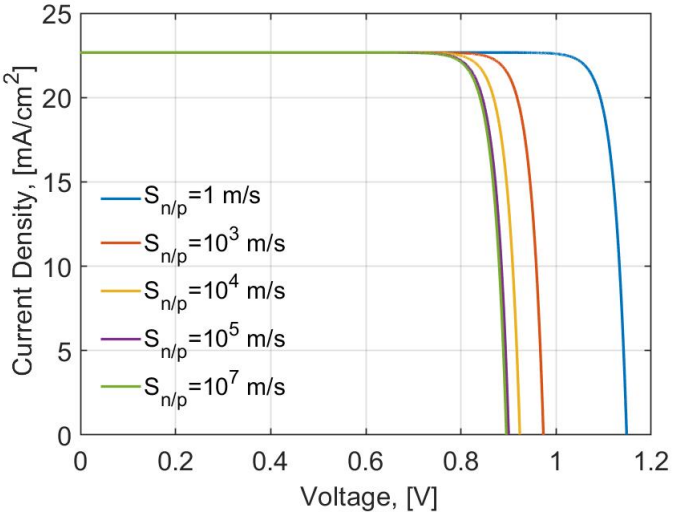

Figure 3.33: J-V characteristics as functions of the recombination velocities $S_n = S_p$ in the range $[10^0 \div 10^7] \frac{\mathtt{m}}{\mathtt{s}}$ and assuming $\tau_p = \tau_n = 10^{-5}\,\mathtt{s}$.

In Fig. 3.33 are shown different J-V characteristics based on carrier lifetime $\tau_n = \tau_p = 10^{-5}\,\mathtt{s}$.
We know that the efficiency depends on the open circuit voltage, so we can understand that for small values of V_{oc} the efficiency decreases. Hence, it is necessary to get $S_{n/p}$ and recombination phenomena under control in order to achieve good results.

J-V characteristic based on *Shokley-Queisser* model and *Hovel* model
Fig. 3.34 shows the ideal characteristic, based on Shokley-Queisser model of a SJ solar cell whose E_g is equal to 1.42 $\mathtt{eV}$.
Based on this E_g, the nominal efficiency η_n is equal to 33.7 % (Fig. 2.4), instead the *detailed balance limit* of efficiency η is equal to 30.3 % (Fig. 2.4). Now, let's consider the n-p GaAs solar cell with the n-region exposed to the Solar Irradiance (Fig 3.23), we show the relative J-V characteristic (Fig. 3.35) for ideal value of surface recombination $S_{n/p} = 1$ and reflection loss summed into shadowing loss, producing $R = 6.6\,\%$. The value of R is taken by [20] considering an ARC typically used on the front of the solar cell in order to reduce the reflection of the photons. Although we have forced ideal values for these critical parameters, we can detect that the photocurrent and the V_{oc} are lower than that of Fig. 3.34.

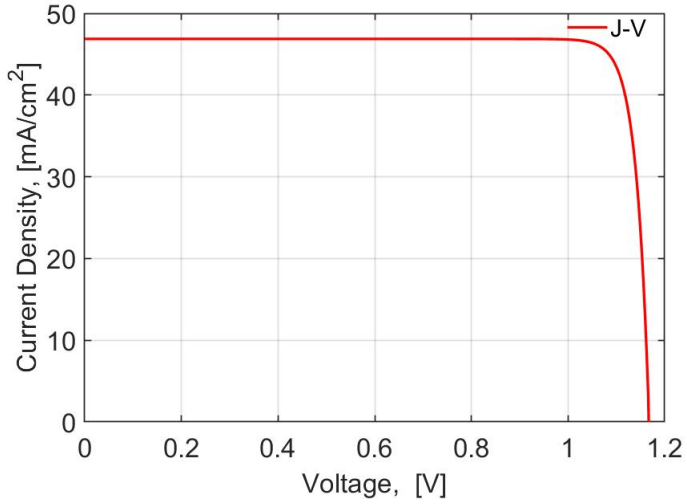

Figure 3.34: J-V characteristic obtained with S-Q model.

Fig. 3.35 is based on parameters taken by Lumb article except for the value of R. However, the J-V characteristic (Fig. 3.35) is comparable with that shown in [16].

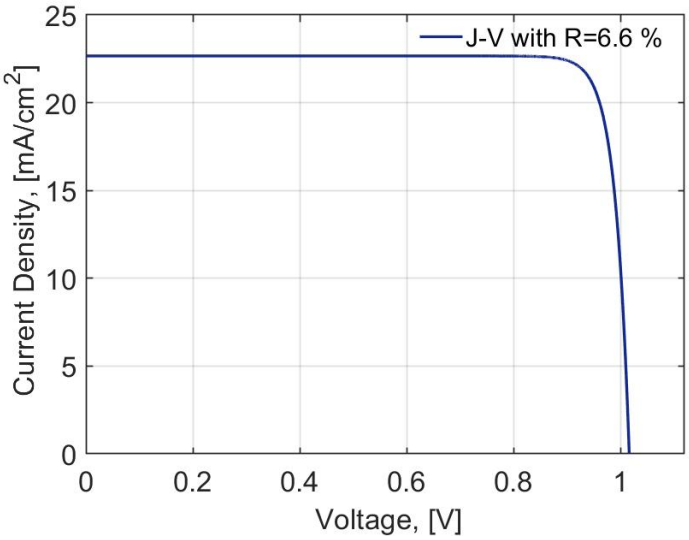

Figure 3.35: J-V characteristic obtained with Hovel model.

For the J-V characteristic of Fig. 3.35 the nominal efficiency is equal $\eta_n = 17\%$ and $\eta = 15\%$, also the Fill Factor results $FF = 88\%$.

3.3.6 AlGaAs solar cell: photocurrent, EQE, J-V characteristic

The aim of this subsection is to apply the same model to another device: $Al_{0.4}Ga_{0.6}As$ n-p solar cell. The following study is not relevant for a real implementation such as SJ solar cell, but it is a benchmark for the study that we will carry out in Chapter 4 for a DJ solar cell. In Fig. 3.3 we can see that $Al_{0.4}Ga_{0.6}As$ absorbs up to 650 $\mathtt{nm}$; this limit is smaller than that of GaAs leading to a lower photocurrent and efficiency.
Consider as reference structure that of Fig. 3.23 exposed by the n-side. The parameters in the following table have been chosen in accordance with several criteria linked to the simulations of Section 4.4.1.

x_j	W	H	S_n	S_p	N_E	N_B	L_p	L_n
$[\mu\mathtt{m}]$	$[\mu\mathtt{m}]$	$[\mu\mathtt{m}]$	$\left[\frac{\mathtt{m}}{\mathtt{s}}\right]$	$\left[\frac{\mathtt{m}}{\mathtt{s}}\right]$	$\left[\frac{1}{\mathtt{cm}^3}\right]$	$\left[\frac{1}{\mathtt{cm}^3}\right]$	$[\mu\mathtt{m}]$	$[\mu\mathtt{m}]$
0.56	0.15	4.7	1	5 x 10^3	10^{17}	10^{18}	4	1.38

Fig. 3.36 reports the behavior of the current density along the emitter and base region.

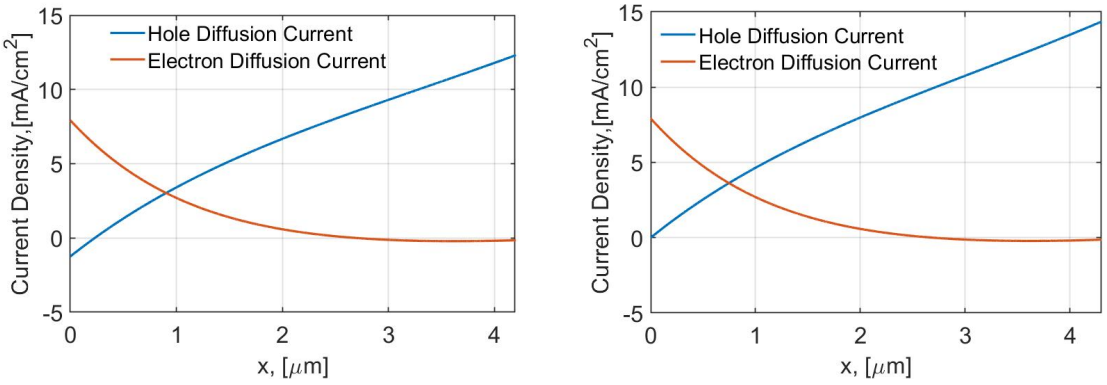

Figure 3.36: Electron and Hole Diffusion Current along x for a n-p $Al_{0.4}Ga_{0.6}As$ solar cell. On the left for $S_p = 5\text{x}10^3$ $\left[\frac{\mathtt{m}}{\mathtt{s}}\right]$, on the right for $S_p = 1$ $\left[\frac{\mathtt{m}}{\mathtt{s}}\right]$.

In Fig. 3.36, on the left, for $x < 0.5$ $\mu\mathtt{m}$, the negative value of the hole photocurrent is given by the Surface Recombination phenomena. We can observe that changing the value of S_p, on the right, the hole photocurrent increases leading to a higher total current. The behavior and comments are the same done for GaAs (Fig. 3.21). The only difference is that the total current will be lower than that obtained for GaAs based on the fact that $Al_{0.4}Ga_{0.6}As$ material has an $E_g = 1.97$. This high bandgap puts a strong limitation on the photocurrent that can be collected, in fact if we focus on Fig. 1.12, in Chapter 1, we can see that the E_g limits the cumulative photocurrent around 25 $\frac{\mathtt{mA}}{\mathtt{cm}^2}$. For this kind of structure, let's obtain the Spectral Efficiency in order to understand how this material, with the reference structure considered, responds to the Solar Irradiance.

From Fig. 3.37, for $S_p = 5\text{x}10^3 \left[\frac{\text{m}}{\text{s}}\right]$, it is possible to appreciate that for $\lambda < 400$ nm the emitter has a bad EQE, instead for $400\,\text{nm} < \lambda < 600\,\text{nm}$ it increases its spectral response around 40%.
The base increases its External Quantum Efficiency beyond 500 nm. Near to 650 nm all the components decrease, linked to the absorption coefficient behavior.

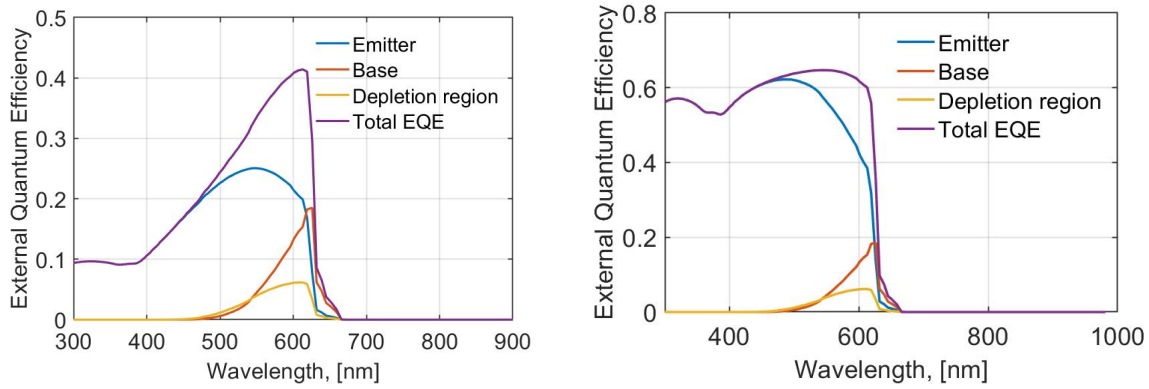

Figure 3.37: EQE for the n-p $Al_{0.4}Ga_{0.6}As$ solar cell. On the left for $S_p = 5\text{x}10^3 \left[\frac{\text{m}}{\text{s}}\right]$, on the right for $S_p = 1 \left[\frac{\text{m}}{\text{s}}\right]$.

For $S_p = 1 \left[\frac{\text{m}}{\text{s}}\right]$, the total EQE in Fig. 3.37 increases, but the EQE linked to the base decreases. With the parameters chosen the base is very limited in the absorption of the photons. Hence, we should change some structural parameters in order to obtain an enhanced efficiency.
The ideal photocurrent for this kind of solar cell, calculated with S-Q model, is around 25 mA as shown in Fig. 3.38, on the right. The J-V characteristic for R=6.6% [20], obtained with the Hovel model is shown in Fig. 3.38, on the left. We can note that both photocurrent and open circuit voltage are lower than that obtained with S-Q model.

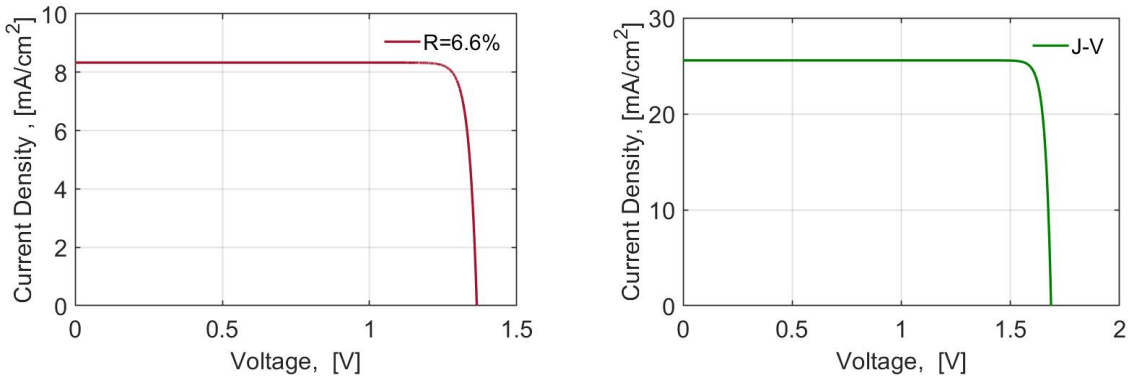

Figure 3.38: J-V characteristic for the n-p $Al_{0.4}Ga_{0.6}As$ solar cell. On the left, J-V based on Hovel model, on the right, J-V based on S-Q model.

3.3.7 AlGaAs-GaAs solar cell: photocurrent, EQE, J-V characteristic

In this section we present another kind of structure composed with both $Al_{0.4}Ga_{0.6}As$ and GaAs. In this case, we consider a heterojunction p-n solar cell with the p-side exposed to the solar irradiance. The p-emitter in $Al_{0.4}Ga_{0.6}As$ and the base in GaAs. In the previous case, the materials were the same for both emitter and base, just the kind of doping was different; hence the depletion region was formed by an homo-junction. In this case, using two different materials, at the interface, there is an hetero-junction. This leads to important consequences in the structure, hence in the equations of the model developed. The aim of this section is to briefly report the only features of the hetero-junctions used to modify correctly the equation of the model in the case of the hetero-structure and simulate this kind of device.
Consider as reference structure that one of Fig. 3.39 where we can observe the effect of the reflectance twice: at the interface Air $-$ $Al_{0.4}Ga_{0.6}As$ and at the interface $Al_{0.4}Ga_{0.6}As$. This is linked to the fact that the two materials have also different refraction index.

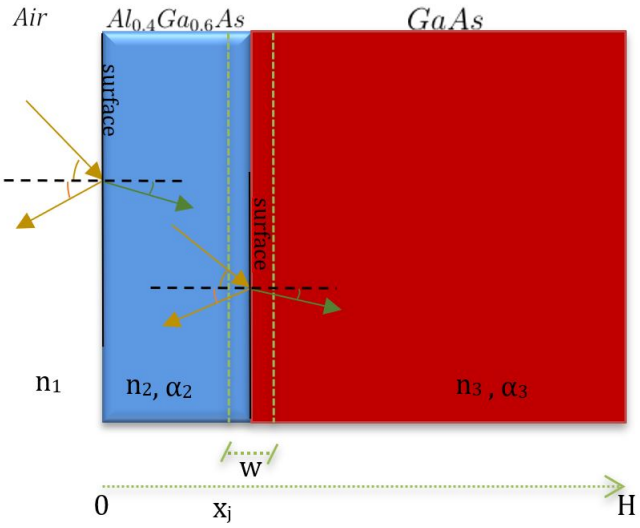

Figure 3.39: $Al_{0.4}Ga_{0.6}As$-GaAs p-n solar cell structure.

In this case, considering normal incidence, photons have a first reflection at the interface Air $-$ $Al_{0.4}Ga_{0.6}As$ and a second reflection at the interface $Al_{0.4}Ga_{0.6}As$-GaAs. In this last one case, the value of Reflectance R' will be lower than that one of the the first case, as already shown in Fig. 3.2. This linked to the fact that the refraction indexes of the two materials are very similar. However, it is necessary taking into account R' into the Generation rate equation (Eq. 3.4).
Another important feature is that the two materials have not only different refraction index but also different absorption coefficient (Fig. 3.3). First of all, photons are

absorbed with the absorption coefficient α_2 in $Al_{0.4}Ga_{0.6}As$ material and then with α_3 in GaAs. It is necessary taking into account also this phenomena. Hence considering also the Reflectance, the Generation Rate for the base region is modified in Eq. 3.92:

$$G(\lambda, x) = \alpha_3(\lambda) SPF(\lambda)(1 - R(\lambda))e^{(-\alpha_2(\lambda)W_1)}(1 - R'(\lambda))e^{(-\alpha_3(\lambda)(x-W_1))} \tag{3.92}$$

Now, let's consider the parameters reported in the following table:

x_j [μm]	W [μm]	H [μm]	S_n $\left[\frac{\text{m}}{\text{s}}\right]$	S_p $\left[\frac{\text{m}}{\text{s}}\right]$	N_E $\left[\frac{1}{\text{cm}^3}\right]$	N_B $\left[\frac{1}{\text{cm}^3}\right]$	L_n [μm]	L_p [μm]
4.68	0.16	6	1	5 x 10^3	10^{18}	10^{17}	4	5

Fig. 3.40, on the left, shows the Diffusion photocurrent for the base and emitter; on the right, the relative EQE is shown.

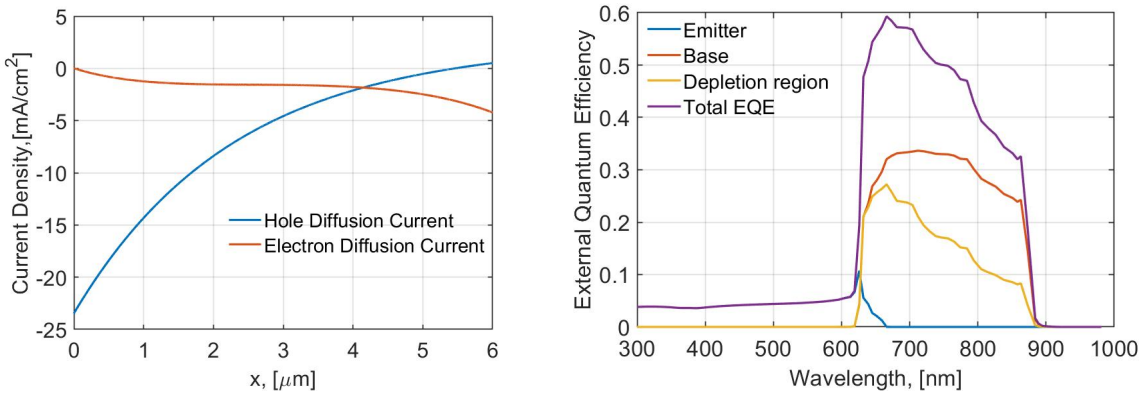

Figure 3.40: Electron and Hole Diffusion Current along x on the left; on the right the EQE.

With these dimensions the emitter region has a bad External Quantum Efficiency and it is not able to absorb photons efficiently.
In order to increase the spectral response let's change some structural parameters:

x_j [μm]	W [μm]	H [μm]	S_n $\left[\frac{\text{m}}{\text{s}}\right]$	S_p $\left[\frac{\text{m}}{\text{s}}\right]$	N_E $\left[\frac{1}{\text{cm}^3}\right]$	N_B $\left[\frac{1}{\text{cm}^3}\right]$	L_p [μm]	L_n [μm]
0.7	0.16	6	1	1	10^{18}	10^{17}	4	5

From Fig. 3.41 we can observe that changing the dimension of the emitter region its spectral response for $S_{n/p} = 1$ $\left[\frac{\text{m}}{\text{s}}\right]$ improves. However, the effect of the parameter S_n is not negligible; indeed for $S_n = 5\text{x}10^3$ $\left[\frac{\text{m}}{\text{s}}\right]$ the EQE linked to the emitter part has a bad behavior.

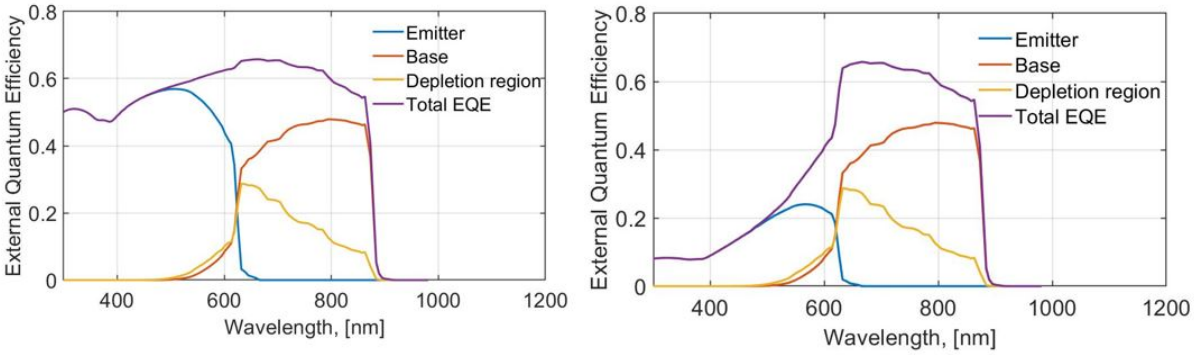

Figure 3.41: EQE characteristic for the p-n $Al_{0.4}Ga_{0.6}As$-GaAs solar cell. On the right for $S_{p/n} = 5x10^3$ $\left[\frac{m}{s}\right]$, on the left for $S_{p/n} = 1$ $\left[\frac{m}{s}\right]$.

Fig. 3.42 shows the characteristic J-V considering R=6.6% [20].

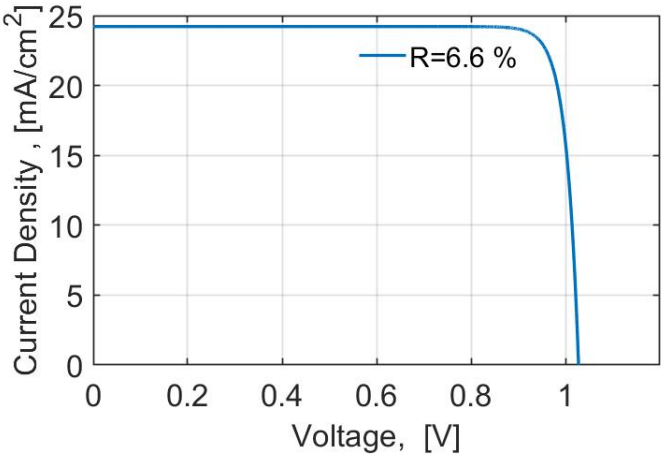

Figure 3.42: J-V characteristic for the p-n $Al_{0.4}Ga_{0.6}As$-GaAs solar cell.

With the parameters used, Fig. 3.42 is similar to that obtained in Fig. 3.35 for a *n-p* GaAs solar cell.
Now, we have analyzed different types of SJ solar cells with the help of Hovel model and observed how the characteristics are modified by the structure and material parameters.
In the following Chapter we will introduce a new kind of DJ solar cell based on $Al_{0.4}Ga_{0.6}As$ and GaAs semiconductor materials in order to explore its several features.

CHAPTER 4

Double Junction Solar cell: the BJT approach

We have analyzed the behavior of a single homo-junction GaAs solar cell, observing the diffusion minority current along the device, the External Quantum Efficiency and the J-V characteristic. Several simulations are also obtained for a *n-p* $Al_{0.4}Ga_{0.6}As$ solar cell and for a hetero-junction $Al_{0.4}Ga_{0.6}As$-GaAs n-p solar cell. In the previous Chapter we have found positive and negative properties of several types of SJ solar cells. Moreover, we have seen that, by playing around with different parameters, it is possible to increase the photocurrent, the EQE or others for a higher conversion efficiency. However, from Chapter 2, we have concluded, thanks to S-Q model, that a DJ solar cell was able to achieve an efficiency higher than that of a SJ one.
DJ solar cells are built by stacking III-V semiconductor layers on top of each other, as several diodes of different materials in series where the current flow between the diodes is realized, practically, by interconnecting them with intermediate tunnel junctions crossed by the electrons thanks to the tunnel effect (Fig. 1.15).
In order to overcome the current matching constraints and achieve a simpler structure respect to the traditional MJ ones, the aim of this chapter is to explore a new kind of DJ solar cell based on a multi-terminal *n-p-n* structure, similar to a heterostructure bipolar transistor (HBJT) proposed, recently, by A. Marti and A. Luque [11]. They were strong-minded about the calculation of the efficiency limit by using the Shokley and Queisser [12]; we will study this new kind of DJ solar cell extending the Hovel model [14].
We will analyze the simulations, using $Al_{0.4}Ga_{0.6}As$ and GaAs materials in order to understand how this kind of device replies to the Solar Spectrum, investigating its features and perhaps recommend some optimization.
We will find that is necessary review the fundamental constraints of a common bipolar structure in order to obtain the same efficiency of a double junction solar cell.

4.1 Bipolar Junction Transistor

First, it is necessary to summarize some properties of the bipolar junction transistor (BJT). Considering a simplified structure *n*-*p*-*n* in Fig. 4.1:

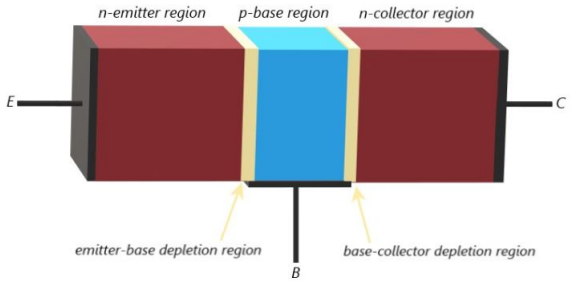

Figure 4.1: *n*-*p*-*n* Bipolar Junction Transistor.

The device is made of three regions doped differently. In Fig. 4.1, for an *n*-*p*-*n* BJT, emitter is **n**-doped, base **p**-doped and collector **n**-doped. There is a terminal contact for each region, for this the Bipolar transistor is known as a three-terminal device [21]. Observing emitter-base junction and base-collector junction we can detect two different diodes. We know that based on how a diode is biased its behavior changes (Fig. 4.2).

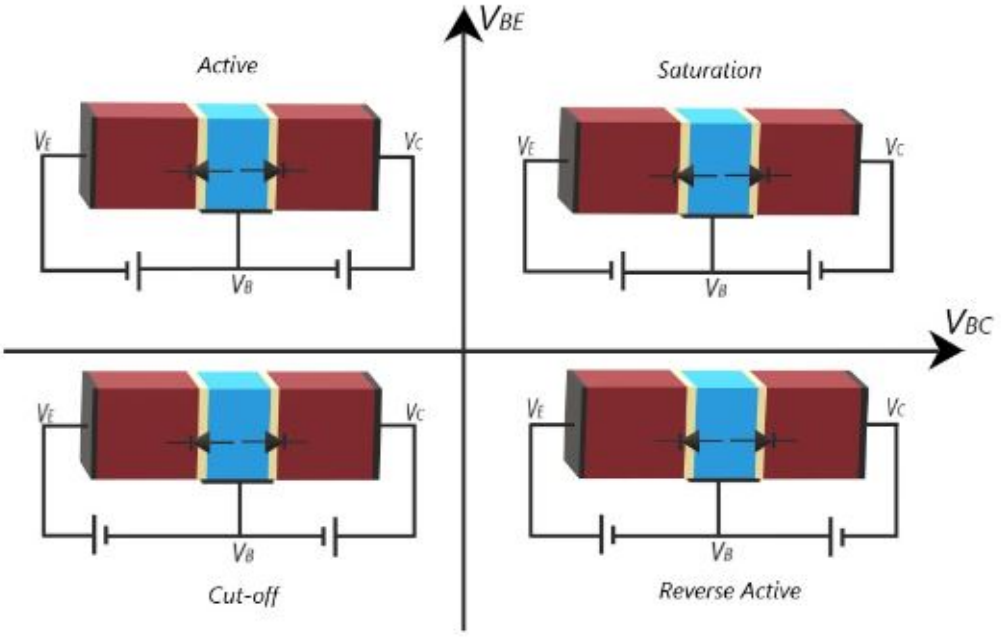

Figure 4.2: BJT device can work in four different regions depending on the value of V_{BE} and V_{BC}.

Fig. 4.2 shows the four operating regions for a BJT [8]:

- **Active region** ($V_{BE} > 0$ and $V_{BC} < 0$) is used if the transistor must be used as an Amplifier;
- **Saturation** ($V_{BE} > 0$ and $V_{BC} > 0$) and **Cut-off** ($V_{BE} < 0$ and $V_{BC} < 0$) mode when the BJT operates like a switching device, for example in digital applications;
- **Reverse Active** ($V_{BE} < 0$ and $V_{BC} > 0$) mode is generally not used; it is specular to the active region but with marginal or no current gain due to the device optimization in terms of doping.

For our goal, we explore the Saturation mode. First, we want to find the Ebers-Moll model, a circuital model helps us to understand how a BJT works.
Fig. 4.3 shows the Band Diagram for a BJT at equilibrium and biased in saturation mode.

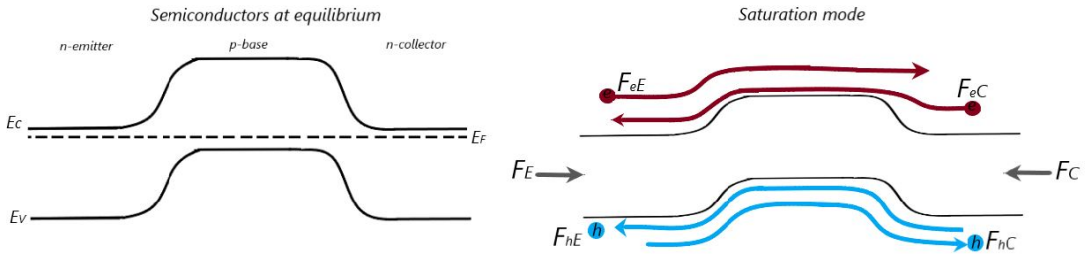

Figure 4.3: Band Diagram: on the left BJT not biased, on the right BJT in saturation mode.

From the theory [8], we know that if we put in contact a n-doped material and a p-doped one, a depletion region is formed and there is a built in potential barrier able to block majority carriers. In saturation mode, the voltage drop at the junction E-B and B-C is lower than that one at equilibrium. In this case, electrons in the emitter Conduction band can cross the barrier and arrive in the base (Red Current flow F_{eE} in Fig. 4.3). In this region, there are two kind of situations based on the relationship between the width of the base W_B and the length that electrons can travel before recombine, expressed by the diffusion length L_D:

- if $W_B > L_D$ significant Recombination takes place;
- if $W_B < L_D$ marginal Recombination takes place.

For a BJT, working in saturation mode, it is very important the second condition because, if there is a marginal recombination, electrons can cross the base and be collected by the collector terminal creating a Current flow F_{eE} between the emitter and collector (Fig. 4.3). In general, a BJT works like a switch in digital applications: cut-off mode in order to have switch OFF and in saturation mode in order to have

switch ON, so maximum transfer of current between emitter and collector. Hence, there is a relationship between the electrons that are injected from the emitter and the electrons that, indeed, arrive at the collector because of Recombination in the base. In Active region the transport of electrons by the emitter to collector F_{eE} is the largest component in a well-designed transistor [8] and the flow F_{eC} is not allowed. In this last operating region, the performance of a BJT is described in terms of its *base transport factor* α_T and *emitter injection efficiency* γ that for a *n-p-n* transistor are defined as follows:

$$\alpha_T \equiv \frac{I_{Cn}}{I_{En}} \tag{4.1}$$

$$\gamma \equiv \frac{I_{En}}{I_{En} + I_{Ep}} \tag{4.2}$$

γ is a measure of the injected electron current compared with the total emitter current I_E; α_T is the ratio between the electron current component able to reach the collector region and the electron current injected from the emitter region. A BJT can reach its ideal performance, the ideal transistor effect, if both the *base transport factor* and *emitter injection efficiency* approach unity.
In Saturation mode, both E-B and B-C are direct biased, so the voltage drop is small in both junctions. In this case, there is not only the Current flow F_{eE} but also the Current flow F_{eC} given by the electrons can cross the barrier going from the collector to the emitter. Again, it is possible quantify the electrons injected from the emitter towards the collector by the *base transport factor* parameter α_F and the electrons injected from the collector towards the emitter by the *base transport factor* parameter α_R.
The points made above are also valid for the holes (Blue Current Flow F_{hE} and F_{hC} in Fig. 4.3), with the only difference that the flux of the holes is the opposite to that of the electrons.
Considering Fig. 4.3, let's calculate the total flux to the emitter and the total flux to the collector.
At the emitter:

$$F_E - F_{eE} + \alpha_R F_{eC} + F_{hE} - \alpha_R F_{hC} = 0 \tag{4.3}$$

Considering that $I_e = -qF_e$ and $I_h = qF_h$, the total emitter Current will be:

$$I_E = -(I_{eE} + I_{hE}) + \alpha_R(I_{eC} + I_{hC}) \tag{4.4}$$

At the collector:

$$F_C - F_{eC} + \alpha_F F_{eE} + F_{hC} - \alpha_F F_{hE} = 0 \tag{4.5}$$

The total collector current will be:

$$I_E = -(I_{eC} + I_{hC}) + \alpha_F (I_{eE} + I_{hE}) \tag{4.6}$$

Eq. 4.4 and Eq. 4.6 lead to the Ebers-Moll model:

$$I_E = -I_{DE} + \alpha_R (I_{DC}) \tag{4.7}$$

$$I_C = -I_{DC} + \alpha_F (I_{DE}) \tag{4.8}$$

By Eq. 4.7 and Eq. 4.8, we can conclude that the bipolar transistor can be modeled by two diodes, whose current components are I_{DE} and I_{DC}, and two Current Controlled Current Sources, $\alpha_F I_{DE}$ and $\alpha_R I_{DC}$.
Fig. 4.4 is the Ebers-Moll scheme, based on Eq. 4.7 and Eq. 4.8:

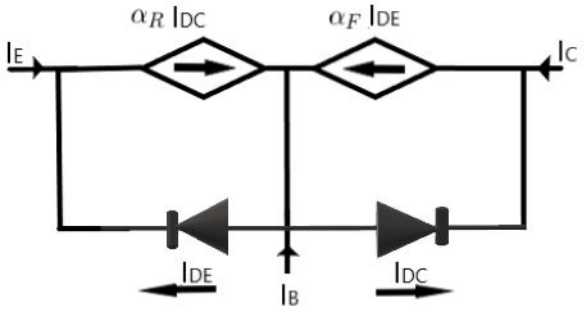

Figure 4.4: Bipolar Junction Transistor: Ebers-Moll model.

The parameter $\alpha_{R/F}$ can have values in the range $0 < \alpha_{R/F} < 1$.

- If $\alpha_{R/F}$ is ideally equal to 1, the charges are able to be collected in the collector or emitter without recombination, hence $I_C \simeq I_E$.
- If $\alpha_{R/F}$ is ideally equal to 0, the charges recombine and the current will be a lot smaller.

In a normal BJT it is clear that we want the first situation with $\alpha_{R/F} = 1$, traduced in practical parameters with $W_B < L_D$.

4.2 BJT under illumination

In the previous discussion we have only considered the contributions obtained without illumination. Based on the fact that the goal is using a Bipolar Transistor structure as a solar cell device is necessary collocate, in this model, the photocurrent component. Consider the BJT of Fig. 4.1 with two loads: one between emitter and base and another between base and collector according to the scheme in Fig. 4.5:

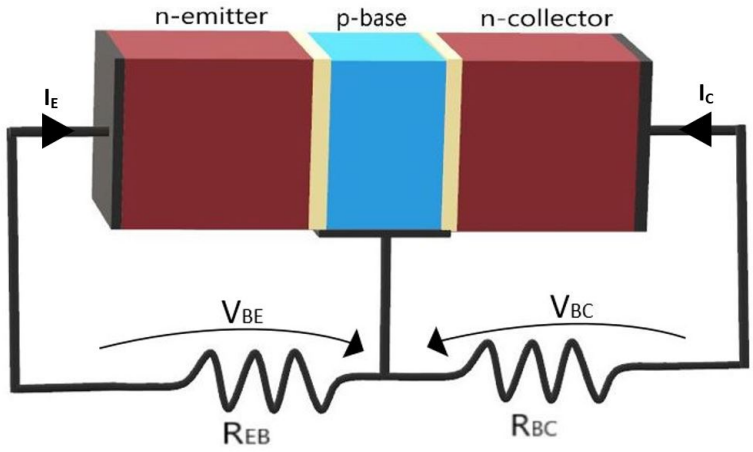

Figure 4.5: BJT device.

Let's illuminate the BJT from the emitter surface. It should be noted that when a BJT is under illumination it is working in a Saturation mode where V_{BE} is the voltage on the load R_{EB} and the V_{BC} is the voltage on the load R_{BC}.
From Fig. 4.5 the total power P extracted from the cell is that through two resistors R_{EB} and R_{BC}.

$$P_{out} = I_E V_{BE} + I_C V_{BC} \tag{4.9}$$

In Section 2.2, the total power extracted by the DJ solar cell was limited by the minimum current between the top diode and the bottom diode (Fig. 2.8) and the electron flow was allowed by a tunnel diode; hence the optimizations of the device taken also into account these current constraints. Instead, considering a BJT structure there are several advantages. The structure in its simplicity reduces the number of layers avoiding tunnel junctions and above all overcomes the constraint on the current flow thanks to the three-terminal configuration by eliminating the configuration in series of the two diodes (Fig. 4.4). Hence, we should be able to maximize independently the current components I_E and I_C.
Fig. 4.6 shows the photogenerated flows. These are in addition to the fluxes, in Dark condition, of Fig. 4.3 . When the BJT device is illuminated, again there are different fluxes linked to the transport of the minority charges based on diffusion phenomena.

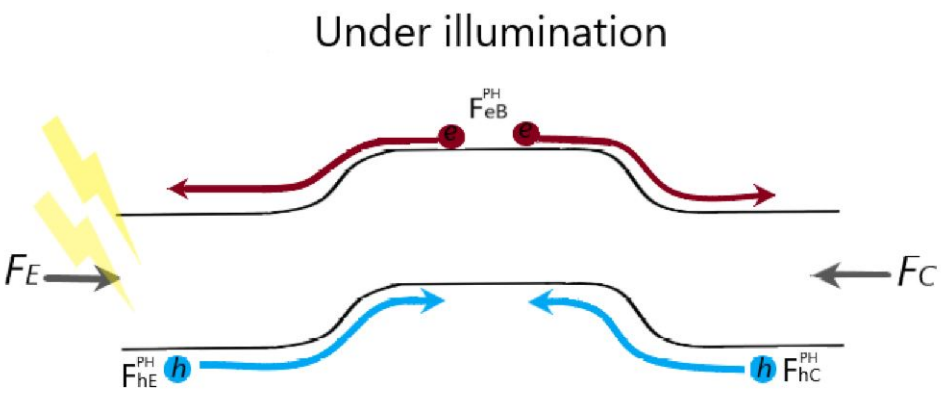

Figure 4.6: Current flows developed under illumination condition.

Under illumination, there is an enhancement of the quantity of the minority charges:

- p_n in the emitter n-region creating the current flux F^{PH}_{hE}
- n_p in the base p-region creating the current flux F^{PH}_{eB}
- p_n in the collector n-region creating the current flux F^{PH}_{hC}

Considering Fig. 4.6 and 4.3 the photogenerated fluxes are in opposite directions to that generated in the dark condition. By these considerations, we can define the Ebers-Moll model with both Photogenerated and Dark Current components (Fig. 4.7).

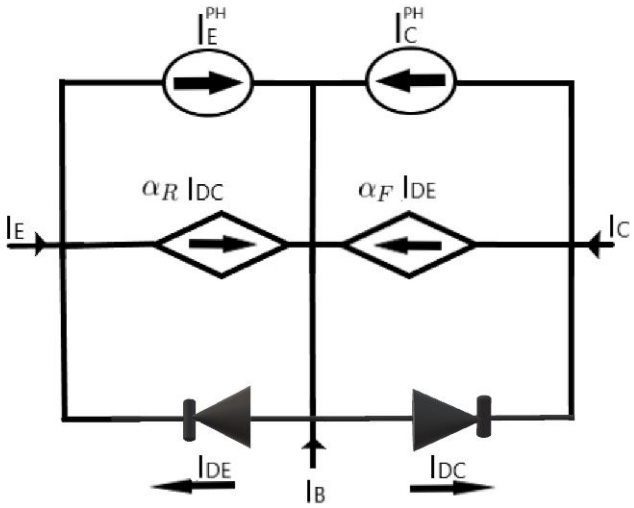

Figure 4.7: BJT-like solar cell: Ebers Moll model under illumination.

The Ebers-Moll model of Fig. 4.7 has, in addition, the component of the photogenerated current, I^{PH}_E and I^{PH}_C, with respect to that of the Fig. 4.4.

There is a high dependence between the parameter $\alpha_{R/F}$ and the generated photocurrent. In Chapter 3 there is an important plot of the Generation rate (Fig. 3.5, Fig. 3.6). In that case we have observed that the Generation rate is based on λ and x, the dimension of the device along the photons propagate. Hence, if the base is short, depending the material adopted, the base will be able or not to absorb some wavelengths. The photocurrent depends a lot by the Generation rate; hence the dimension of each Bipolar Transistor region should influence the total Photocurrent. Probably, for a BJT working under illumination, having a short base can be the worst case.
In this context there is another aspect to underline. In Ebers Moll model, having a BJT with a long base is translated, ideally, into the condition $\alpha_{R/F}$ =0. Only in this case the Ebers Moll model has the scheme of Fig. 4.8:

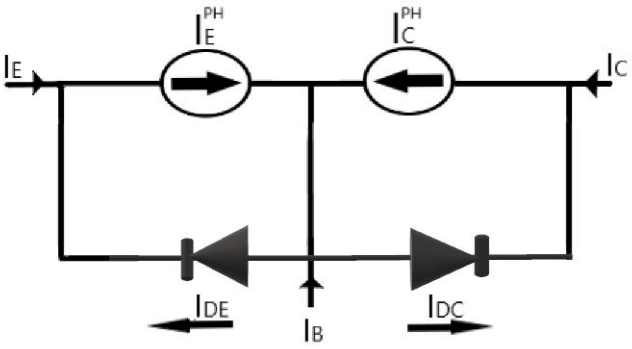

Figure 4.8: BJT-like solar cell: Ebers Moll model under illumination with $\alpha_{R/F}$=0.

Increasing the base dimension, developing a situation of $W_B > L_D$ with total recombination in the base region, in the Ebers-Moll Model it is possible to delete the two Current Controlled Current Sources (Fig. 4.7).
In this situation a Bipolar Transistor can be seen like two diodes with a common region. Without simulations a first idea can be that a multi-terminal solar cell can be approximated by two different solar cells. In order to understand if our considerations are correct, we extend the Hovel model to a BJT structure in order to obtain an analytical way to describe the photovoltaic characteristic of the device.

4.3 Analytical model: multi-terminal solar cell with Bipolar Transistor structure

In order to study the diffusion current along the device, it is necessary to extend the Hovel model, studied in Chapter 3 for a SJ solar cell, to a BJT structure (Fig. 4.9):

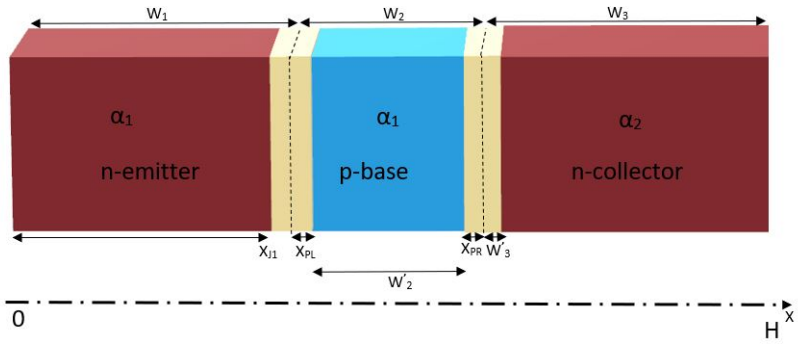

Figure 4.9: Bipolar Junction Transistor structure.

From Fig. 4.9 the dimensions of emitter collector and base are W_1, W_2 and W_3 respectively. The thicknesses of the depletion regions are: $W_1 - x_{j1}$ for the n-emitter side, x_{pl} for the p-base side at the interface with the emitter, instead x_{pr} at the interface with the collector and finally $W_3^{'}$ for the n-collector side. $W_2^{'}$ is the dimension of the base without the depletions region. H is the depth of the solar cell.
The material used for the emitter and base is the same, developing a homojunction; instead the collector has different material; hence creating a heterojunction between base and collector. The material used for the emitter and base is $Al_{0.4}Ga_{0.6}As$ and for the collector is GaAs; α_1 is the absorption coefficient for $Al_{0.4}Ga_{0.6}As$ and α_2 for GaAs. We note that in Chapter 3 we have studied separately the n-p homojunction solar cell in $Al_{0.4}Ga_{0.6}As$ and the heterojunction solar cell in $Al_{0.4}Ga_{0.6}As$-GaAs.

4.3.1 Emitter region

The approach is the same of Section 3.2. First, consider the n-type emitter region whose starting equation is:

$$\frac{d^2(p_n - p_{n0})}{dx^2} - \left(\frac{p_n - p_{n0}}{D_p \tau_p}\right) + \left(\frac{\alpha_1 F(1-R)e^{(-\alpha_1 x)}}{D_p}\right) = 0 \tag{4.10}$$

The associated boundary equations, without considering Dark conditions, are:

$$\frac{d(p_n - p_{n0})}{dx} = \frac{S_p}{D_p}(p_n - p_{n0}); \quad \text{for } x = 0 \tag{4.11}$$

$$p_n - p_{n0} = 0; \quad \text{for } x = x_{j1} \tag{4.12}$$

The solution is the same of that of the previous chapter, just changing the electrons with holes, arriving to the solution given in Eq. 4.13:

$$p_n - p_{n0} = \delta \left[\frac{\mathrm{e}^{-\alpha_1 x_{j1}} \left(\cosh\left(\frac{x}{L_p}\right) + \frac{S_p L_p}{D_p} \sinh\left(\frac{x}{L_p}\right) \right) + \sinh\left(\frac{x_{j1} - x}{L_p}\right) \left(\alpha_1 L_p + \frac{S_p L_p}{D_p}\right)}{\cosh\left(\frac{x_j}{L_p}\right) + \frac{S_p L_p}{D_p} sinh\left(\frac{x_j}{L_p}\right)} \right] + - \delta \mathrm{e}^{-\alpha_1 x} \tag{4.13}$$

where $\delta = \dfrac{\alpha_1 F (1-R) \tau_p}{\alpha_1^2 L_p^2 - 1}$.

From equation:

$$J_p = -qD_p \frac{dp_n}{dx} \tag{4.14}$$

it is possible to obtain the hole diffusion current density, for $x = x_{j1}$:

$$J_p = qL_p \frac{\alpha_1 F (1-R)}{\alpha_1^2 L_p^2 - 1} \left[\frac{-\mathrm{e}^{-\alpha_1 x_{j1}} \left(\sinh\left(\frac{x_{j1}}{L_p}\right) + \frac{S_p L_p}{D_p} \cosh\left(\frac{x_{j1}}{L_p}\right) \right) + \left(\alpha_1 L_p + \frac{S_p L_p}{D_p}\right)}{\cosh\left(\frac{x_{j1}}{L_p}\right) + \frac{S_p L_p}{D_p} \sinh\left(\frac{x_{j1}}{L_p}\right)} \right] + - qL_p \frac{\alpha_1 F (1-R)}{\alpha_1^2 L_p^2 - 1} \left(\alpha_1 e^{-\alpha_1 x_{j1}}\right) \tag{4.15}$$

In order to obtain also the Dark current we put the Generation rate equal to zero:

$$\frac{1}{q} \left(\frac{dJ_p}{dx} \right) + \frac{p_n - p_{n0}}{\tau_p} = 0 \tag{4.16}$$

considering the boundary conditions (Eq. 4.17 and Eq. 4.18):

$$\frac{d(p_n - p_{n0})}{dx} = \frac{S_p}{D_p} (p_n - p_{n0}); \quad \text{for } x = 0 \tag{4.17}$$

$$p_n = p_{n0} e^{\left(\frac{qV_{BE}}{kT} \right)}; \quad \text{for } x = x_{j1} \tag{4.18}$$

where V_{BE} is the voltage across the load R_{BE}.
Solving Eq. 4.16 and using the previous boundary equations we obtain the Dark current.

Let's write the complete equation for the minority charges in the emitter for $x = x_{j_1}$:

$$J_{pE} = qL_p \frac{\alpha_1 F(1-R)}{\alpha_1^2 L_p^2 - 1} \left[\frac{-\mathrm{e}^{-\alpha_1 x_{j1}} \left(\sinh\left(\frac{x_{j1}}{L_p}\right) + \frac{S_p L_p}{D_p} \cosh\left(\frac{x_{j1}}{L_p}\right) \right) + \left(\alpha_1 L_p + \frac{S_p L_p}{D_p} \right)}{\cosh\left(\frac{x_{j1}}{L_p}\right) + \frac{S_p L_p}{D_p} sinh\left(\frac{x_{j1}}{L_p}\right)} \right] +$$

$$- qL_p \frac{\alpha_1 F(1-R)}{\alpha_1^2 L_p^2 - 1} \left(\alpha_1 \ \mathrm{e}^{-\alpha_1 x_{j1}} \right) +$$

$$- qD_p \frac{ni^2}{N_D} \frac{1}{L_p} \left[\frac{\sinh\left(\frac{x_{j1}}{L_p}\right) + \frac{S_p L_p}{D_p} \cosh\left(\frac{x_{j1}}{L_p}\right)}{\cosh\left(\frac{x_{j1}}{L_p}\right) + \frac{S_p L_p}{D_p} \sinh\left(\frac{x_{j1}}{L_p}\right)} \right] \left(\mathrm{e}^{\left(\frac{qV_{BE}}{KT}\right)} - 1 \right) \tag{4.19}$$

4.3.2 Base region

The starting equation for the p-type base region is:

$$\frac{d^2(n_p - n_{p0})}{dx^2} - \left(\frac{n_p - n_{p0}}{D_n \tau_n} \right) + \left(\frac{\alpha_1 F(1-R) \mathrm{e}^{(-\alpha_1 x)}}{D_n} \right) = 0 \tag{4.20}$$

Solving the differential equation, we obtain the solution given by the Eq. 4.21, like in the Chapter 3.

$$n_p - n_{p0} = \Gamma \mathrm{e}^{\left(\frac{x}{L_n}\right)} + \Theta \mathrm{e}^{\left(-\frac{x}{L_n}\right)} - \delta \mathrm{e}^{-\alpha_1 x} \tag{4.21}$$

In order to obtain directly both the Photocurrent and the Dark Current, consider the boundary conditions (Eq. 4.22 and Eq. 4.23) based on the Boltzmann relationships for carriers on the two sides of the junction:

$$n_p - n_{p0} = n_p^{'} = n_{p0} \left(\mathrm{e}^{\left(\frac{qV_{BE}}{KT}\right)} - 1 \right); \quad \text{for } x = W_1 + x_{PL} \tag{4.22}$$

$$n_p - n_{p0} = n_p^{''} = n_{p0} \left(\mathrm{e}^{\left(\frac{qV_{BC}}{KT}\right)} - 1 \right); \quad \text{for } x = W_1 + x_{PL} + W_2^{'} \tag{4.23}$$

For $x = W_1 + x_{PL}$, Eq. 4.21 yields to:

$$\Gamma \mathrm{e}^{\left(\frac{W_1 + x_{PL}}{L_n}\right)} + \Theta \mathrm{e}^{\left(-\frac{W_1 + x_{PL}}{L_n}\right)} - \delta \mathrm{e}^{-\alpha(W_1 + x_{PL})} = n_p^{'} \tag{4.24}$$

From the previous equation:

$$\Gamma = \mathrm{e}^{\left(-\frac{W_1 + x_{PL}}{L_n}\right)} \left[-\Theta \mathrm{e}^{\left(-\frac{W_1 + x_{PL}}{L_n}\right)} + \delta \mathrm{e}^{-\alpha(W_1 + x_{PL})} + n_p^{'} \right] \tag{4.25}$$

Then, apply the boundary condition Eq. 4.23 for $x = W_1 + x_{PL} + W_2^{'}$ to Eq. 4.21:

$$\begin{aligned} \mathrm{e}^{\left(-\frac{W_1 + x_{PL}}{L_n}\right)} \left[-\Theta \mathrm{e}^{\left(-\frac{W_1 + x_{PL}}{L_n}\right)} + \delta \mathrm{e}^{-\alpha(W_1 + x_{PL})} + n_p^{'} \right] \mathrm{e}^{\left(\frac{W_1 + x_{PL} + W_2^{'}}{L_n}\right)} + \\ + \Theta \mathrm{e}^{\left(-\frac{W_1 + x_{PL} + W_2^{'}}{L_n}\right)} - \delta e^{-\alpha\left(W_1 + x_{PL} + W_2^{'}\right)} = n_p^{''} \end{aligned} \tag{4.26}$$

The Eq. 4.26 can be rewritten in the following way:

$$\begin{aligned} -\Theta \mathrm{e}^{\left(-\frac{W_1 + x_{PL}}{L_n}\right)} \mathrm{e}^{\left(\frac{W_2^{'}}{L_n}\right)} + \Theta \mathrm{e}^{\left(-\frac{W_1 + x_{PL} + W_2^{'}}{L_n}\right)} = \\ = -\delta \mathrm{e}^{-\alpha\left(W_1 + x_{PL} + \frac{W_2^{'}}{L_n}\right)} + \delta \mathrm{e}^{-\alpha\left(W_1 + x_{PL} + W_2^{'}\right)} - n_p^{'} \mathrm{e}^{\left(\frac{W_2^{'}}{L_n}\right)} + n_p^{''} \end{aligned} \tag{4.27}$$

Also considering that:

$$-\theta \mathrm{e}^{\left(-\frac{W_1 + x_{PL}}{L_n}\right)} \left[\mathrm{e}^{\left(\frac{W_2^{'}}{L_n}\right)} - \mathrm{e}^{\left(-\frac{W_2^{'}}{L_n}\right)} \right] = -\Theta \mathrm{e}^{\left(-\frac{W_1 + x_{PL}}{L_n}\right)} 2\sinh\left(\frac{W_2^{'}}{L_n}\right)$$

It is possible obtain Θ:

$$\Theta = \frac{\mathrm{e}^{\left(\frac{W_1 + x_{PL}}{L_n}\right)}}{2\sinh\left(\frac{W_2^{'}}{L_n}\right)} \left[\delta \mathrm{e}^{-\alpha(W_1 + x_{PL})} \left[\mathrm{e}^{\left(\frac{W_2^{'}}{L_n}\right)} - \mathrm{e}^{-W_2^{'}} \right] - n_p^{'} \mathrm{e}^{\left(\frac{W_2^{'}}{L_n}\right)} + n_p^{''} \right] \tag{4.28}$$

Replacing Θ in Γ:

$$\begin{aligned} \Gamma = & \frac{\mathrm{e}^{\left(-\frac{W_1 + x_{PL}}{L_n}\right)}}{2\sinh\left(\frac{W_2^{'}}{L_n}\right)} \left[n_p^{'} \left(e^{\left(\frac{W_2^{'}}{L_n}\right)} - \mathrm{e}^{\left(-\frac{W_2^{'}}{L_n}\right)} \right) - n_p^{'} \mathrm{e}^{\left(\frac{W_2^{'}}{L_n}\right)} + n_p^{''} \right] + \\ & + \frac{\mathrm{e}^{\left(-\frac{W_1 + x_{PL}}{L_n}\right)}}{2\sinh\left(\frac{W_2^{'}}{L_n}\right)} \left[-\delta \mathrm{e}^{-\alpha x_j} \left(\mathrm{e}^{\left(\frac{W_2^{'}}{L_n}\right)} - \mathrm{e}^{-\alpha W_2^{'}} \right) + \delta \mathrm{e}^{-\alpha x_j} \left(\mathrm{e}^{\left(\frac{W_2^{'}}{L_n}\right)} - \mathrm{e}^{\left(-\frac{W_2^{'}}{L_n}\right)} \right) \right] \end{aligned} \tag{4.29}$$

Simplifying the previous equation:

$$\Gamma = \frac{\mathrm{e}^{\left(-\frac{W_1 + x_{PL}}{L_n}\right)}}{2\sinh\left(\frac{W_2^{'}}{L_n}\right)} \left[-n_p^{'} \mathrm{e}^{-\left(\frac{W_2^{'}}{L_n}\right)} + n_p^{''} + \delta \mathrm{e}^{-\alpha x_j} \left(\mathrm{e}^{-\alpha W_2^{'}} - \mathrm{e}^{\left(-\frac{W_2^{'}}{L_n}\right)} \right) \right] \tag{4.30}$$

Substituting Eq. 4.30 and Eq. 4.28 in Eq. 4.21, this last one becomes:

$$\begin{aligned} n_p - n_{p0} = & \frac{\mathrm{e}^{\left(-\frac{W_1 + x_{PL}}{L_n}\right)}}{2\sinh\left(\frac{W_2^{'}}{L_n}\right)} \mathrm{e}^{\left(\frac{x}{L_n}\right)} \left[-n_p^{'} \mathrm{e}^{\left(\frac{-W_2^{'}}{L_n}\right)} + n_p^{''} + \delta \mathrm{e}^{-\alpha x_j} \left(\mathrm{e}^{-\alpha W_2^{'}} - \mathrm{e}^{\left(-\frac{W_2^{'}}{L_n}\right)} \right) \right] \\ & + \frac{\mathrm{e}^{\left(\frac{W_1 + x_{PL}}{L_n}\right)}}{2\sinh\left(\frac{W_2^{'}}{L_n}\right)} \mathrm{e}^{\left(\frac{-x}{L_n}\right)} \left[n_p^{'} \mathrm{e}^{\left(\frac{-W_2^{'}}{L_n}\right)} - n_p^{''} + \delta \mathrm{e}^{-\alpha x_j} \left(\mathrm{e}^{-\alpha W_2^{'}} - \mathrm{e}^{\left(-\frac{W_2^{'}}{L_n}\right)} \right) \right] \end{aligned} \tag{4.31}$$

Using Eulero transformations, the previous yields to:

$$n_p - n_{p0} = n_p^{'}\left[\frac{\sinh\left(\frac{x_j + W_2^{'} - x}{L_n}\right)}{\sinh\left(\frac{W_2^{'}}{L_n}\right)}\right] - n_p^{''}\left[\frac{\sinh\left(\frac{x_j - x}{L_n}\right)}{\sinh\left(\frac{W_2^{'}}{L_n}\right)}\right] +$$
$$- \delta e^{-\alpha\left(W_2^{'}+x_j\right)}\left[\frac{\sinh\left(\frac{x_j - x}{L_n}\right)}{\sinh\left(\frac{W_2^{'}}{L_n}\right)}\right] + \delta e^{-\alpha x_j}\left[\frac{\sinh\left(\frac{x_j + W_2^{'} - x}{L_n}\right)}{\sinh\left(\frac{W_2^{'}}{L_n}\right)}\right] - \delta \mathrm{e}^{-\alpha x} \quad (4.32)$$

In order to obtain the diffusion current, apply the following equation:

$$J_n = qD_n\frac{dn_p}{dx} \quad (4.33)$$

So, for $x = x_{PL} + W_1$, the electron diffusion current is:

$$J_{nEB} = qL_n\frac{\alpha_1 F(1-R)}{\alpha_1^2 L_n^2 - 1}\left[\frac{n_{p0}\left(\mathrm{e}^{\left(\frac{qV_{BC}}{KT}\right)} - 1\right) + \mathrm{e}^{-\alpha_1\left(x_{PL}+W_1+W_2^{'}\right)}}{\sinh\left(\frac{W_2^{'}}{L_n}\right)}\right] +$$
$$- qL_n\frac{\alpha_1 F(1-R)}{\alpha_1^2 L_n^2 - 1}\left[\frac{n_{p0}\left(\mathrm{e}^{\left(\frac{qV_{BE}}{KT}\right)} - 1\right) + \mathrm{e}^{-\alpha_1(x_{PL}+W_1)}}{\sinh\left(\frac{W_2^{'}}{L_n}\right)}\cosh\left(\frac{W_2^{'}}{L_n}\right) + L_n\alpha_1\ \mathrm{e}^{-\alpha_1(x_{PL}+W_1)}\right] \quad (4.34)$$

So, for $x = x_{PL} + W_1 + W_2^{'}$, the electron diffusion current is:

$$J_{nBC} = qL_n \frac{\alpha_1 F(1-R)}{\alpha_1^2 L_n^2 - 1} \left[\frac{n_{p0}\left(\mathrm{e}^{\left(\frac{qV_{BC}}{KT}\right)} - 1\right) + e^{-\alpha_1\left(x_{PL}+W_1+W_2^{'}\right)}}{\sinh\left(\frac{W_2^{'}}{L_n}\right)} \cosh\left(\frac{W_2^{'}}{L_n}\right) + \right.$$

$$\left. - qL_n \frac{\alpha_1 F(1-R)}{\alpha_1^2 L_n^2 - 1} \left[\frac{n_{p0}\left(\mathrm{e}^{\left(\frac{qV_{BE}}{KT}\right)} - 1\right) + \mathrm{e}^{-\alpha_1(x_{PL}+W_1)}}{\sinh\left(\frac{W_2^{'}}{L_n}\right)} + L_n \alpha_1 \mathrm{e}^{-\alpha_1\left(x_{PL}+W_1+W_2^{'}\right)} \right] \right. \tag{4.35}$$

4.3.3 Collector region

In order to obtain the photocurrent in the collector region it is necessary to consider that between the base and collector there is a heterojunction.
In this case, the term of the Generation rate changes taking into account the different refraction index between the interface $Al_{0.4}Ga_{0.6}As/GaAs$ and the different absorption coefficient (Section 3.3.6 for more details).
Also for the collector, the solution of Eq. 4.36 is similar to that of Chapter 3. In order to give a complete solution, we report only the relevant changes in the equations with respect to the solution procedure explained in Section 3.2.2. The starting equation is:

$$\frac{d^2(p_n - p_{n0})}{dx^2} - \left(\frac{p_n - p_{n0}}{D_p \tau_p}\right) + \left(\frac{\alpha_2 F(1-R) e^{-\alpha_1(W_1+W_2)}(1-R^{'}) e^{-\alpha_2(x-W_1-W_2)}}{D_p}\right) = 0 \tag{4.36}$$

The general solution of the differential equation is:

$$p_n - p_{n0} = A\cosh\left(\frac{x}{L_p}\right) + B\sinh\left(\frac{x}{L_p}\right) - \delta \mathrm{e}^{-\alpha_2(x-(W_1+W_2))} \tag{4.37}$$

where:

$$\delta = \frac{\tau_p \alpha_2 F\,(1-R)\,(1-R^{'})\mathrm{e}^{\alpha_1(W_1+W_2)}}{\alpha_2^2 L_p^2 - 1}$$

Eq. 4.38 and Eq. 4.39 give the boundary equations at $V_{BE} = 0$ and $V_{BC} = 0$:

$$p_n - p_{n0} = 0; \quad \text{for } x = W_1 + W_2 + W_3^{'} \tag{4.38}$$

$$\frac{d(p_n - p_{n0})}{dx} = -\frac{S_p}{D_p}(p_n - p_{n0}); \quad \text{for } x = H \tag{4.39}$$

Solving Eq. 4.37 with the Eq. 4.38 and the Eq. 4.39:

$$p_n - p_{n0} = \frac{\alpha_2(1-R^{'})F(1-R)\tau_p \mathrm{e}^{-\alpha_1(W_1+W_2)}\mathrm{e}^{-\alpha_2(W_3^{'})}}{\alpha_2^2 L_p^2 - 1}\left[\cosh\left(\frac{x - W_1 - W_2 - W_3^{'}}{L_p}\right) - \mathrm{e}^{-\alpha_2(x-W_1-W_2)}\right] - \left[\frac{\alpha_2(1-R^{'})F(1-R)\tau_p \mathrm{e}^{-\alpha_1(W_1+W_2)}\mathrm{e}^{-\alpha_2(W_3^{'})}}{\alpha_2^2 L_p^2 - 1}\sinh\frac{x - W_1 - W_2 - W_3^{'}}{L_p}\right]$$
$$\mathrm{x}\left[\frac{\frac{S_p L_p}{D_p}\left[\cosh\frac{H'}{L_p} - \mathrm{e}^{-\alpha_2 H'}\right] + \sinh\frac{H'}{L_p} + \alpha_2 L_p \mathrm{e}^{-\alpha_2 H'}}{\cosh\left(\frac{H'}{L_p}\right) + \frac{S_p L_p}{D_p}\sinh\left(\frac{H'}{L_p}\right)}\right] \tag{4.40}$$

where $H^{'} = H - (W_1 + W_2 + W_3^{'})$.
In order to obtain the dark current, we put the Generation rate equal to zero considering the following boundary conditions:

$$p_n = p_{n0}\mathrm{e}^{\left(\frac{qV_{BC}}{kT}\right)}; \quad \text{for } x = W_1 + W_2 + W_3^{'} \tag{4.41}$$

$$\frac{d(p_n - p_{n0})}{dx} = -\frac{S_p}{D_p}(p_n - p_{n0}); \quad \text{for } x = H \tag{4.42}$$

where V_{BC} is the voltage across the load R_{BC}.
Solving Eq. 4.37, with the Generation rate equal to 0, and using the previous boundary conditions we obtain the Dark current.
Eq. 4.43 is the complete solution with both Dark current and Photocurrent for $x = W_1 + W_2 + W_3^{'}$.

$$J_{pC} = -\frac{qL_p\alpha_2(1-R^{'})F(1-R)\mathrm{e}^{-\alpha_1(W_1+W_2)}\mathrm{e}^{-\alpha_2(W_3^{'})}}{\alpha^2L_p^2-1}$$
$$\mathrm{x}\left[\alpha_2L_p - \frac{\frac{S_pL_p}{D_p}\left[\cosh\frac{H'}{L_p} - \mathrm{e}^{-\alpha_2H'}\right] + \sinh\frac{H'}{L_p} + \alpha_2L_pe^{-\alpha_2H'}}{\cosh\left(\frac{H'}{L_p}\right) + \frac{S_pL_p}{D_p}\sinh\left(\frac{H'}{L_p}\right)}\right]$$
$$+ qD_p\frac{ni^2}{N_D}\frac{1}{L_p}\left[\frac{\sinh\left(\frac{H^{'}}{L_p}\right) + \frac{S_pL_p}{D_p}\cosh\left(\frac{H^{'}}{L_p}\right)}{\cosh\left(\frac{H^{'}}{L_p}\right) + \frac{S_pL_p}{D_p}\sinh\left(\frac{H^{'}}{L_p}\right)}\right]\left(\mathrm{e}^{\left(\frac{qV_{BC}}{KT}\right)} - 1\right) \quad (4.43)$$

In order to have a complete model, it is necessary to introduce the equations of the generated photocurrent into the depletion regions.
In the depletion region between emitter and base:

$$J_{drEB} = qF(1-R)\mathrm{e}^{-\alpha_1(x_{j1})}\left(1-\mathrm{e}^{-\alpha_1W_1^{'}}\right) \quad (4.44)$$

In the base depletion region for $(W_1 + W_2 - x_{PR}) < x < (W_1 + W_2)$:

$$J_{drBC} = qF(1-R)\mathrm{e}^{-\alpha_1(x_{j2})}\left(1-\mathrm{e}^{-\alpha_1x_{PR}}\right) \quad (4.45)$$

In the collector depletion region for $(W_1 + W_2) < x < (W_1 + W_2 + W_3^{'})$:

$$J_{drC} = qF(1-R)(1-R^{'})\mathrm{e}^{-\alpha_1(W_1+W_2)}\left(1-\mathrm{e}^{-\alpha_2W_3^{'}}\right) \quad (4.46)$$

Now, we can define the short-circuit current from the emitter part J_E^{sc} (Eq. 4.47) and collector part (Eq. 4.48) J_C^{sc} for $V_{BE} = 0$ and $V_{BC} = 0$.
From Eq. 4.19, Eq. 4.44 and Eq. 4.34, we can obtain:

$$J_E^{sc} = J_{pE} + J_{drEB} + J_{nEB} \quad (4.47)$$

Eq. 4.35, Eq. 4.45, Eq. 4.46 and Eq. 4.43 yield to:

$$J_C^{sc} = J_{nBC} + J_{drBC} + J_{drC} + J_{pC} \quad (4.48)$$

Considering Eq. 4.47, Eq. 4.48, it is possible obtain the nominal efficiency of a HBJT solar cell:

$$\eta_n = \frac{(J_E^{sc}V_{BE}^{oc}) + (J_C^{sc}V_{BC}^{oc})}{P_{in}} \quad (4.49)$$

where the open-circuit voltage V_{BE}^{oc} and V_{BC}^{oc} can be obtained considering the total current from emitter and collector respectively equal to zero; P_{in} is the power incident on the solar cell surface.

4.4 Simulations: multi-terminal solar cell with Bipolar Transistor structure

We have obtained the analytical model able to describe the current components in each region of the BJT. Hence, we are ready, through the following simulations, to find how a traditional BJT can achieve a good efficiency as solar cell.

4.4.1 A common BJT as a solar cell device

First, we consider the BJT in Dark condition in order to observe the concentration profile of the minority charges along the device.
We impose possible values for V_{BE} and V_{BC} similar to that we should obtain under illumination considering the open circuit voltages.
The parameters, referred to Fig. 4.9, have the following values:

W_1 [μm]	W_2 [μm]	W_3 [μm]	H [μm]	x_{PL} [μm]	x_{PR} [μm]	N_{DE} [cm^{-3}]	N_{AB} [cm^{-3}]	N_{DC} [cm^{-3}]	L_{pE} [μm]	L_{nB} [μm]	L_{pC} [μm]
2	0.6	5.4	8	0.047	0.046	10^{19}	10^{18}	10^{19}	0.27	1.38	0.3

Fig. 4.10 shows the minority carriers concentration profile for emitter, base, and collector.

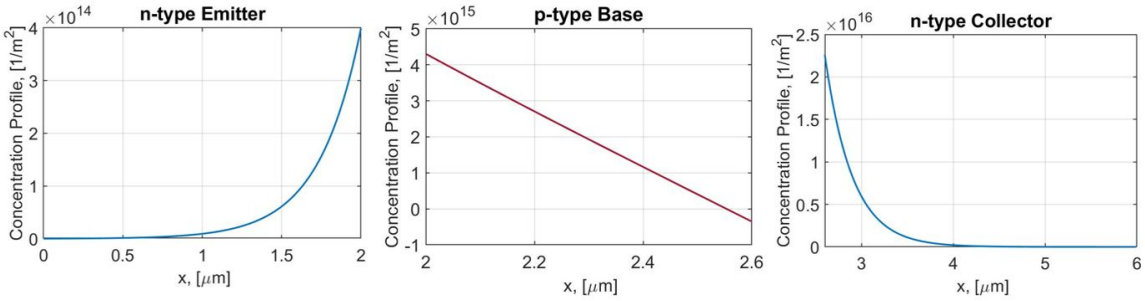

Figure 4.10: Minority carriers concentration profile along the device.

From Fig. 4.10 is interesting to observe the linear behavior of the minority concentration profile in the base; this confirms that there is not recombination phenomena along the base. For a common BJT this is the best case!
Now, we should discover if this case is the best also when the BJT is under illumination.
First of all, let's consider the spectral response EQE

$$EQE = \frac{J_{pE}^{ph}}{qF} + \frac{J_{drB}}{qF} + \frac{J_{nEB}^{ph} + J_{nBC}^{ph}}{qF} + \frac{J_{drBC} + J_{drC}}{qF} + \frac{J_{pC}^{ph}}{qF} \tag{4.50}$$

In order to understand how each component of a traditional BJT replies to the Solar Irradiance let's observe Fig. 4.11.

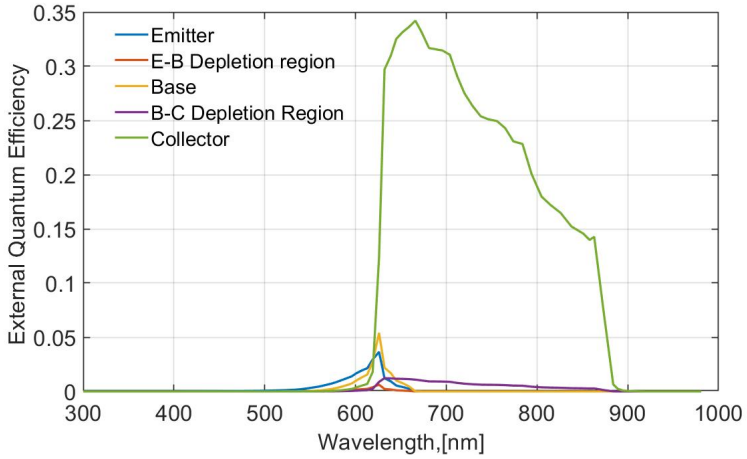

Figure 4.11: External Quantum Efficiency for a common BJT structure.

From Fig. 4.11, we can detect that each component has bad spectral response. The peak of absorption is in the collector region around 0.35 that is a very small value.
Let's observe the diffusion photocurrent J_{pE}^{ph} in emitter, J_{nB}^{ph} in base and J_{pC}^{ph} in collector region shown in Fig. 4.12:

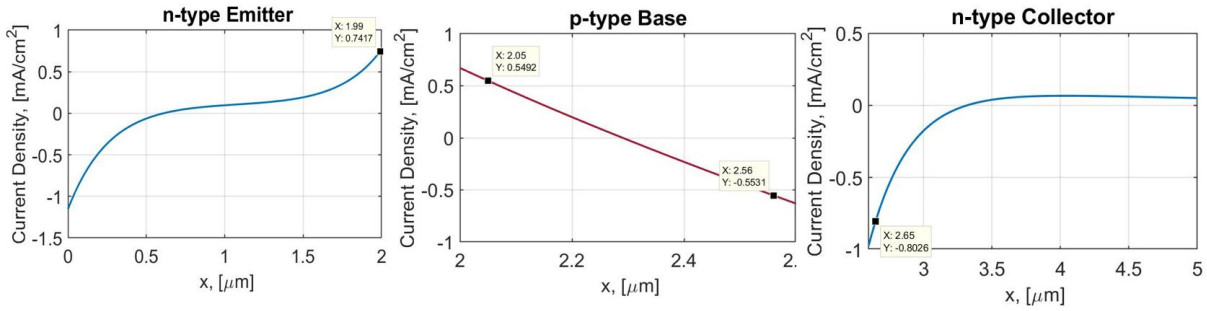

Figure 4.12: Diffusion Photocurrent J_{pE}^{ph} in emitter region, J_{nB}^{ph} in base region and J_{pC}^{ph} in collector region.

Both Fig. 4.11 and Fig. 4.12 are based on the values of the previous table that are typical of a Bipolar Transistor where both emitter and collector are more doped than the base whose width is short in order to avoid recombination phenomena (confirmed from Fig. 4.10).
In Fig. 4.12 data tips are positioned in the points linked to the boundary conditions where the diffusion photocurrent components are calculated:

- emitter part: $x = x_{j1}$;
- base part: $x = W_1 + x_{PL}$ and $x = W_1 + x_{PL} + W_2^{'}$;
- collector part: $x = W_1 + W_2 + W_3^{'}$.

In the positions itemized, the relative photocurrent has a very small value, hence the total emitter current (Eq 4.47) and collector current (Eq. 4.48) will be small, leading to a low efficiency.
It is possible conclude that a standard HBJT with these dimensions and doping levels cannot be used as solar cell.
As we have said in Section 4.2, there is a strong dependency between the base width, the Generation rate and the photocurrent density. In particular, we have underlined that if the base is short, probably we should have a bad photocurrent components, also proven from simulations in Fig. 4.11 and in Fig. 4.12.
Based on this consideration, let's change some parameters in order to find out if we have some improvements.
Let's suppose to increase the base dimension; in the following table we report the value of the new structural parameters:

W_1	W_2	W_3
[μm]	[μm]	[μm]
0.7	4	3.3

First, increasing the base width, let's see also how the minority concentration profile in the base changes.
Fig. 4.13 shows the new concentration profile of the minority charges in Dark condition.

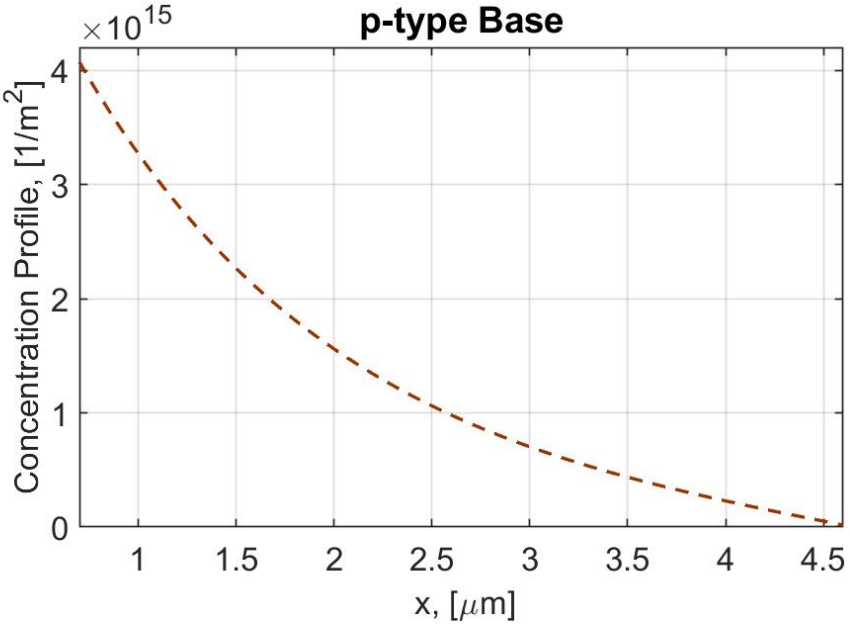

Figure 4.13: Minority carriers concentration profile along the base.

In Fig. 4.13, it is possible to note the Recombination phenomena. In fact, increasing the base Width up to 4 μm the behavior changes from linear (Fig. 4.10) to exponential

(Fig. 4.13) due to Recombination ($L_{nB} < W_2$).
Let's observe the base photocurrent:

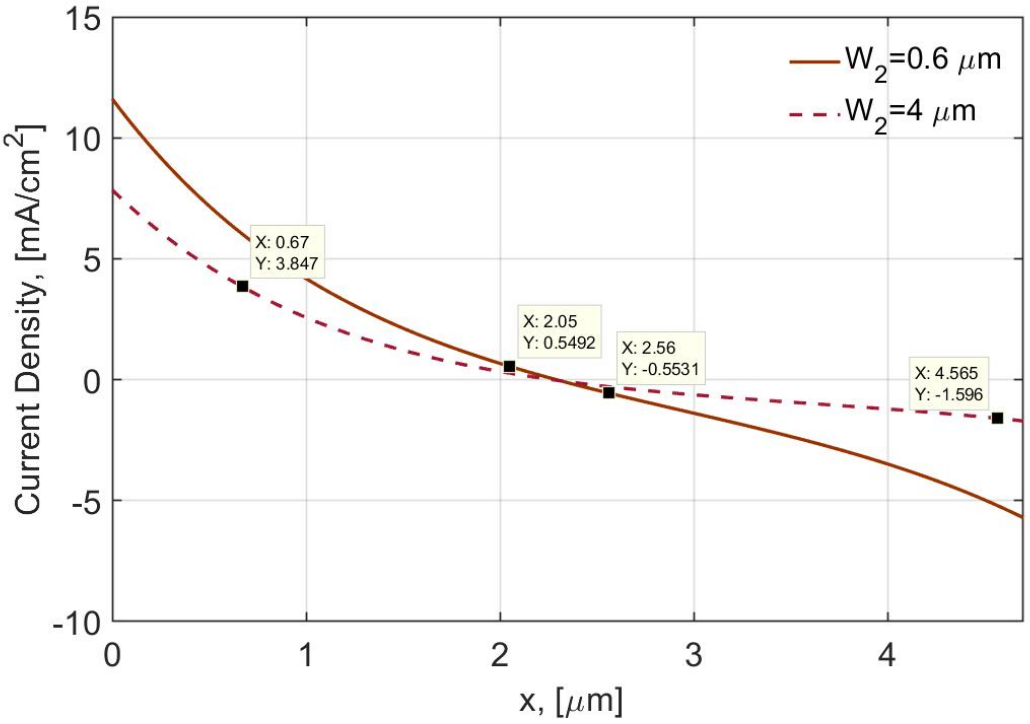

Figure 4.14: Photocurrent in the base region for $W2 = 0.6\mu\mathtt{m}$ and for $W2 = 4\mu\mathtt{m}$.

From Fig. 4.14, we can see that increasing the width of the base the value of the photocurrent at the boundary conditions increases respect to that obtained for a short base. In particular, the dashed line is achieved only changing structural parameters.
In order to increase both photocurrent in emitter, base and collector it is also necessary reasoning on the effect of the doping level.
For the purpose of finding the best compromise for our structure we remember that doping parameter and dimensions are linked. Indeed, there are several points to take into account; following we report the most important points:

- If we put in contact a n-region and a p-region, a depletion region is formed and it will cover more space in the material less doped. Let's consider a practical example linked to our device. If the emitter is less doped respect to the base, we put attention that the depletion region doesn't cover all the emitter part. The greater the emitter region covered from the depleted one, the lower will be its spectral response. By this, it is necessary to examine how the doping level influences the dimensions of the depletion region respect to the width of the emitter part.

- Another important parameter is the diffusion length and the problem of the

recombination. This phenomenon, in the collector and in the emitter, is not good because we want that electrons and holes should be collected at the contacts. We know that there is a strong connection between doping level and diffusion length. Consider a practical case. Emitter is, in our case of study, n-type doped. This has an important consequence on the quantity of the holes and electrons. For the electrons, the diffusion length in the n-material is not important because they are the majority carriers: a very small quantity recombines with holes, so this percentage of electrons is negligible. Instead, the amount of holes is very low in a n-type material. This means that if the diffusion length of the holes is very low, the recombination is high and holes cannot be collected. Hence, the generated photocurrent in the emitter and collector will be very small. This effect can be seen, very well, in the spectral response (Fig. 4.11) with high doping level in the emitter and collector.
Usually, in a common BJT, the emitter and collector doping is higher than that in base because the minority charges have a different and negligible roles.
Instead, for a BJT used as solar cell is very important that holes can be collected, avoiding recombination. In order to do that we can working on the doping and on the width of the emitter. It is important noting the role of the emitter and collector are different. In fact, the first is the window, the first layer exposed to the Solar Irradiance, of a hypothetical solar cell. Instead, the collector has the role of a "base", "base" referred to the term used for a common Single Junction solar cell.

- For the collector region is important a good thickness in order to collect the part of SI with high wavelength.

Summarizing, the starting point was considering a BJT with its common structural and doping parameters. In that case, from Fig. 4.11 and Fig. 4.12 we have noted that the EQE and the photocurrent for the base, emitter and collector had a bad values; concluding that a common BJT cannot be a good solar cell device. Hence, we have changed the width of the base finding, from Fig. 4.14, that the values of the photocurrent, in the base, rise increasing the base dimensions.
Now, we try to do some changing on doping and structure dimensions. It is very difficult find the best structure; our aim is to achieve a medium optimization in order to understand if our BJT with some changes can be used as a solar cell.
Let's consider the parameters reported in the following tables:

W_1 [μm]	W_2 [μm]	W_3 [μm]	H [μm]	$(W_1 - x_{j1})$ [μm]	x_{PL} [μm]	x_{PR} [μm]	$W_3^{'}$ [μm]	N_{DE} [cm^{-3}]	N_{AB} [cm^{-3}]	N_{DC} [cm^{-3}]
0.7	4	1.3	6	0.14	0.014	0.015	0.15	10^{17}	10^{18}	10^{17}

S_{pE} $\left[\frac{\mathtt{m}}{\mathtt{s}}\right]$	S_{pC} $\left[\frac{\mathtt{m}}{\mathtt{s}}\right]$	L_{pE} $[\mu\mathtt{m}]$	L_{nB} $[\mu\mathtt{m}]$	L_{pC} $[\mu\mathtt{m}]$
5 x 10^3	5 x 10^3	4	1.38	5

Based on these parameters, Fig. 4.15 shows the Diffusion Photocurrent along the device.

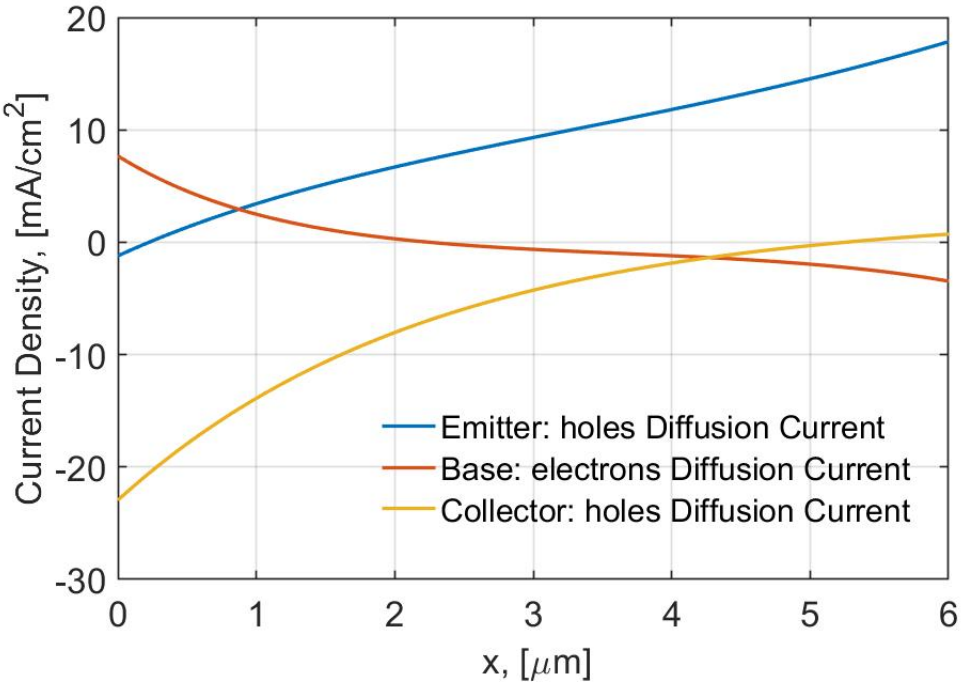

Figure 4.15: Diffusion Photocurrent along the BJT structure.

First, it is necessary to remember that the BJT, that we are simulating, is composed by $Al_{0.4}Ga_{0.6}As$ emitter and base and GaAs collector. The width of the base, now, is $W_2 = 4\mu\mathtt{m}$ with a high Recombination phenomena (Fig. 4.13). This means that in the Ebers-Moll model of Fig. 4.7 both the parameters α_R and α_F decrease to zero. Hence we are moving to the Ebers-Moll model of Fig. 4.8 where the BJT can be represented by two diodes with a common region:

- a n-p diode in $Al_{0.4}Ga_{0.6}As$;
- a p-n diode in $Al_{0.4}Ga_{0.6}As$-GaAs.

Each diode can be seen as a SJ sub-cell connected to a load. Hence, we are reducing to the cases just studied in Section 3.3.6 where we have applied the Hovel model to a *n-p* homojunction $Al_{0.4}Ga_{0.6}As$ solar cell and in Section 3.3.7 for a heterojunction *p-n* $Al_{0.4}Ga_{0.6}As$-GaAs solar cell.

We report the simulations about the diffusion photocurrent obtained in the cases mentioned (Fig. 4.16).

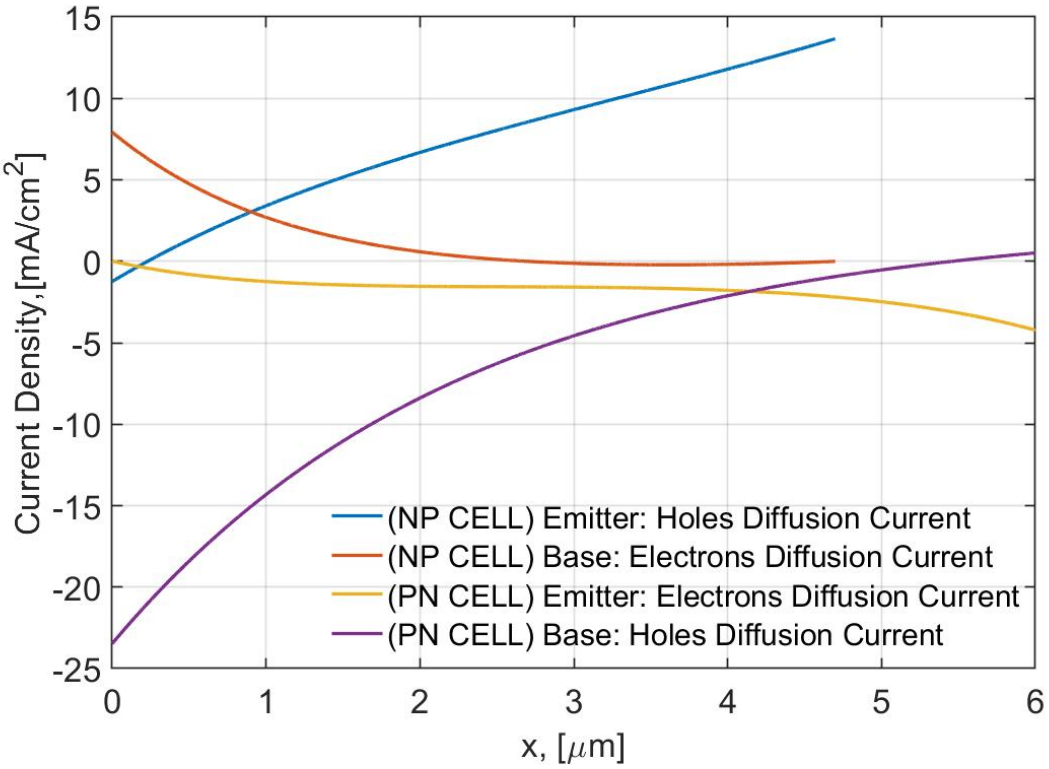

Figure 4.16: Diffusion Photocurrent for a homojunction n-p $Al_{0.4}Ga_{0.6}As$ solar cell and for a heterojunction p-n $Al_{0.4}Ga_{0.6}As$-GaAs solar cell.

Let's observe Fig. 4.15 and Fig. 4.16 based on the same parameters. Very interesting is the behavior of the base Diffusion photocurrent referred to the BJT (red line in Fig. 4.15) respect to the same Diffusion photocurrent for the two types of solar cell (red and yellow line in Fig. 4.16). In fact, we can note that the base photocurrent in bipolar transistor is nothing than more a compromise between the two curves obtained from the single sub-cells. Initially, its behavior is similar to that we can find in the *n-p* solar cell (red line), and then, around $x = 3\mu\mathtt{m}$, the electrons photocurrent of Fig. 4.15 changes its behavior leading to that of the electrons photocurrent in the emitter region of the *p-n* heterojunction solar cell (yellow line). About the emitter and collector bipolar transistor photocurrent it is possible to note that they are the same respectively to the Holes Diffusion Current of the *n-p* solar cell and to the Holes Diffusion Current of the *p-n* solar cell. It is possible to conclude that increasing the width of the base, the photocurrent components of the *n-p-n* BJT solar cell lead to that of two independents *n-p* and *p-n* sub-cells. Hence, by changing the traditional structure parameters, a BJT can be used as a possible solar cell.

4.4.2 A better design

First, let's observe the External Quantum Efficiency of Fig. 4.17 considering the parameters of the previous table.

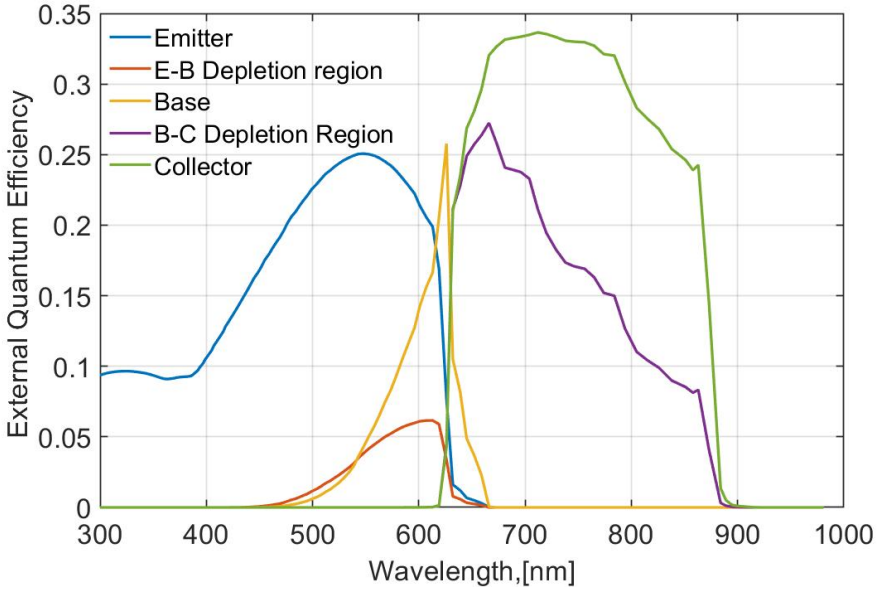

Figure 4.17: External Quantum Efficiency for a BJT solar cell.

From Fig. 4.17 we can observe that the EQE has improved respect to that of Fig. 4.11. However, the spectral response is not good above all in the emitter region.
In order to increase the EQE, let's consider the following parameters:

W_1 [μm]	W_2 [μm]	W_3 [μm]	H [μm]	$(W_1 - x_{j1})$ [μm]	x_{PL} [μm]	x_{PR} [μm]	$W_3^{'}$ [μm]	N_{DE} [cm^{-3}]	N_{AB} [cm^{-3}]	N_{DC} [cm^{-3}]
0.1	3	4.9	8	0.0.34	0.034	0.014	0.15	10^{18}	10^{18}	10^{17}

S_{pE} [$\frac{m}{s}$]	S_{pC} [$\frac{m}{s}$]	L_{pE} [μm]	L_{nB} [μm]	L_{pC} [μm]
5 x 10^3	5 x 10^3	1	1.38	5

Fig. 4.18 shows the External Quantum Efficiency considering separately emitter base sub-cell and base collector one.
The blue line in Fig. 4.18 is obtained from:

$$EQE_{EB} = \frac{J_{pE}^{ph}}{qF} + \frac{J_{drB}}{qF} + \frac{J_{nEB}^{ph}}{qF} \tag{4.51}$$

The green line in Fig. 4.18 is obtained from:

$$EQE_{BC} = \frac{J_{nBC}^{ph}}{qF} + \frac{J_{drBC} + J_{drC}}{qF} + \frac{J_{pC}^{ph}}{qF} \tag{4.52}$$

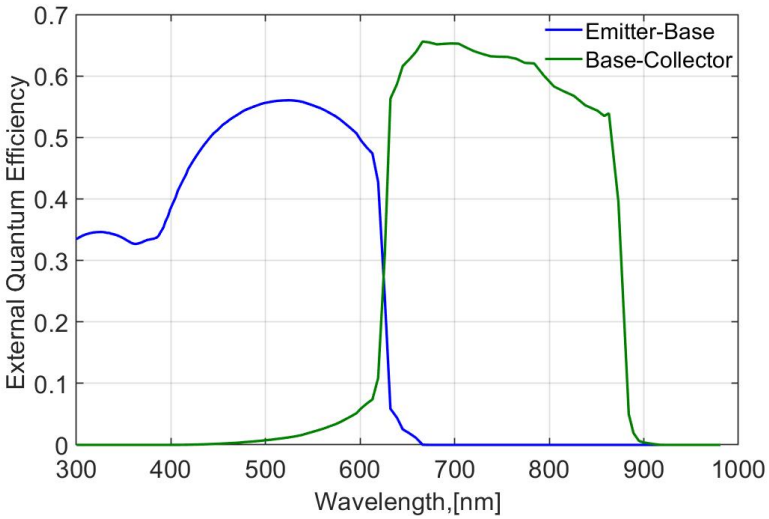

Figure 4.18: External Quantum Efficiency for emitter-base and base-collector sub-cell.

From Fig. 4.18 we can note that the EQE is increased respect to the previous cases. This means that with some changes the BJT can have a good External Quantum Efficiency. In order to quantify how much Solar Irradiance this BJT solar cell can absorb, we can observe Fig. 4.19. From this simulation we can detect that the BJT structure has the behavior of DJ solar cell (Fig. 2.7), in fact the first layers of a material absorb the first part of spectrum and the others, the remaining one.

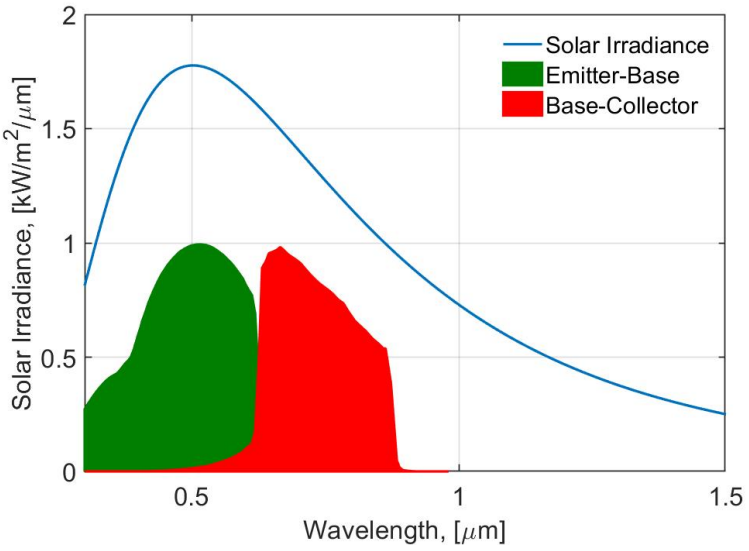

Figure 4.19: Solar Irradiance absorbed by the emitter-base and base-collector sub-cells respect to the total one.

For the collector we have chosen GaAs material that has an Eg=1.42 eV. This means that the part of the Solar Irradiance since $\lambda > 870$nm cannot be absorbed.
In order to solve this problem, the idea can be to choose a material with a smaller Eg or very interesting should be using the BJT structure as a building block for a MJ solar cell. In this way, for example, we can choose for the second BJT building block materials with lower Eg in order to cover all parts of the Solar Irradiance spectrum.
However, in order to complete the discussion is very interesting to obtain the characteristic J-V for the three-terminal HBJT solar cell.
In Fig. 4.5 we can detect two loads R_{EB} and R_{BC}. The current J_E on the load R_{EB} is obtained from the sum of: J_{pE} (Eq. 4.19), J_{drEB} (Eq. 4.34) and J_{nEB} (Eq. 4.44), instead on the load R_{BC} the current J_C is obtained from J_{nBC} (Eq. 4.35), J_{drBC} (Eq. 4.43), J_{drC} (Eq. 4.45) and J_{pC} (Eq. 4.46).
The short-circuit current J_E^{sh} and J_C^{sh} are obtained from Eq. 4.47 and Eq. 4.48.
Then, in order to obtain the open-circuit voltage V_{BE}^{oc} across the load R_{EB} we put $V_{BC} = 0$ and J_E=0.
For the open-circuit voltage V_{BC}^{oc} across the load R_{BC} we put $V_{BE} = 0$ and J_C=0.
We put also the Reflectance of the $Al_{0.4}Ga_{0.6}As$ equal to 6.6% (taken by [20]); S_n and S_p equal to 1.

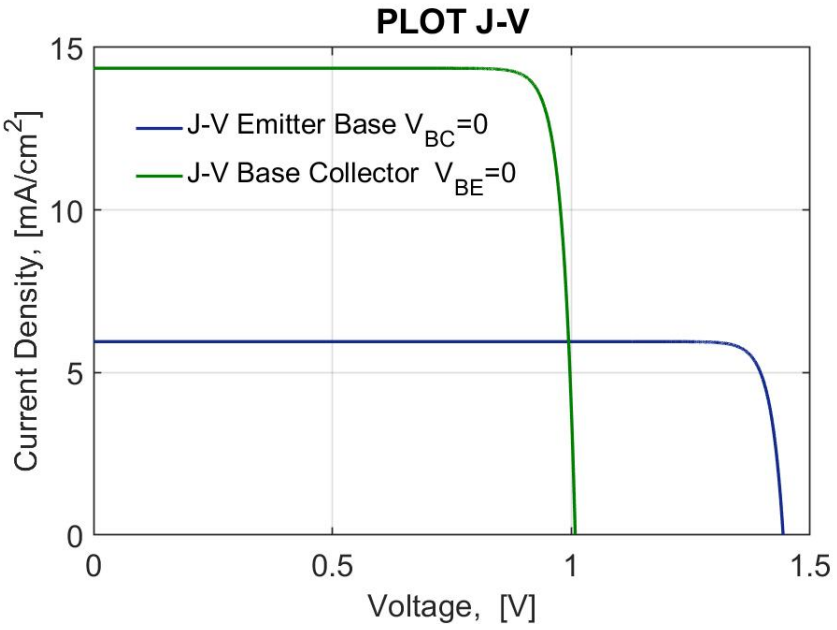

Figure 4.20: emitter-base J-V characteristic and base-collector J-V characteristic.

Fig. 4.20 is based on the parameters reported in the following table:

W_1 [μm]	W_2 [μm]	H [μm]	N_{DE} [cm^{-3}]	N_{AB} [cm^{-3}]	N_{DC} [cm^{-3}]
0.1	2	14	10^{18}	10^{18}	10^{17}

The length diffusion for emitter, base and collector are the same of previous. The blue and green characteristic are not good if we take them separately. The advantage of this multi-terminal structure is that the base-emitter and the base-collector sub-cells are connected to two independent loads leading to a high efficiency obtained from Eq. 4.49.
Finally, we propose some plots in order to understand how the total efficiency can change respect to some parameters.
There are a lot of degrees of freedom linked to doping and to the structure dimensions. We must remember that the creation of two sub-cells is linked to the dimension of the base and to the recombination phenomena.
Fig. 4.21 shows the Nominal Efficiency respect to the emitter Thickness. In all solar cells the emitter layer thickness has an important effect on the solar cell efficiency. A good efficiency is given by a short emitter, but it is necessary to control that the depleted region doesn't cover the emitter one. In order to decide the best emitter thickness, it will be necessary to put attention on both doping level and width of the depletion region.

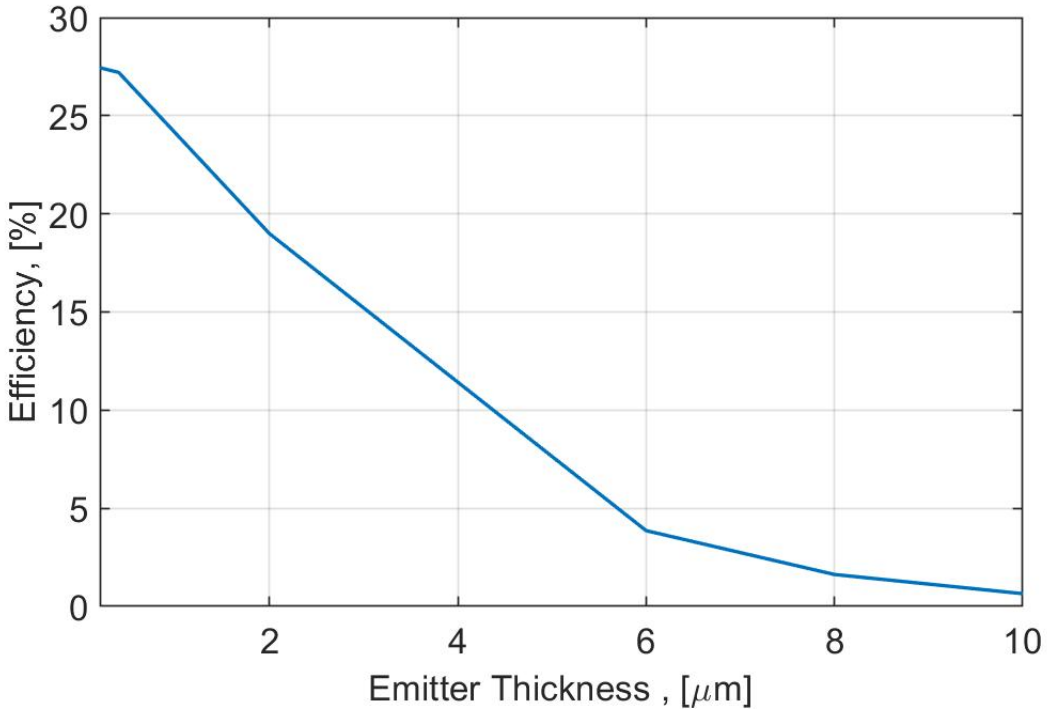

Figure 4.21: Nominal Efficiency versus emitter Thickness.

Finally, let's consider the following parameters:

W_1	W_2	H	N_{AB}
[μm]	[μm]	[μm]	[cm^{-3}]
0.2	1.8	14	10^{18}

We have fixed a value for the base doping. Hence, let's change the emitter doping and collector one in order to observe the behavior of the Efficiency.

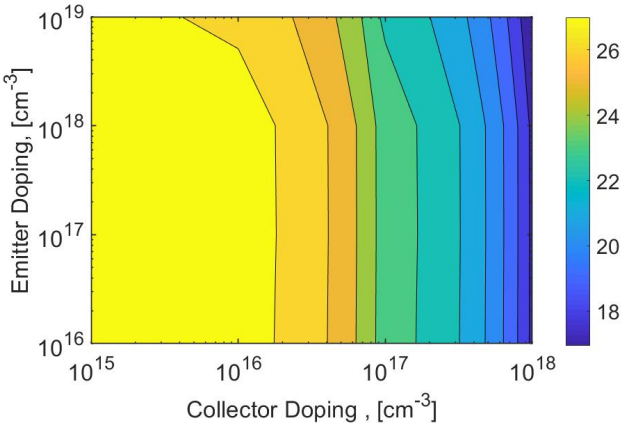

Figure 4.22: Nominal Efficiency based on emitter doping and collector doping.

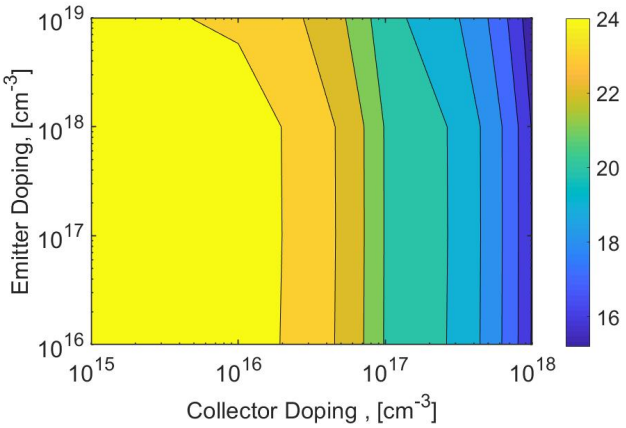

Figure 4.23: Efficiency based on emitter doping and collector doping.

From Fig. 4.23 we can note that increasing the collector doping, the Efficiency decreases. In general, with the parameters chosen in this last section the maximum nominal efficiency is around 26-27%. This value is consistent with values that can be found in literature [22][23]. Probably, the efficiency found can be improved choosing others structural parameters and levels doping.
However, from the previous results we must be optimistic on future developing of this type of solar cell. Based on this thesis project it is possible to conclude that a multi-terminal solar cell with Bipolar transistor structure can be used as an alternative to the traditional DJ solar cell or as a building block for MJ solar cell reducing the number of layers and at the same time avoiding tunnel junctions.

Conclusions

Solar power is one of the most important solutions against the *non-renewable* resources that are the main resources for the energy production and responsible for ecological disasters.
In modern days, there are several kinds of solar cells; MJ ones play a leading role achieving a high conversion efficiency thanks to their structure and innovative materials. In general, for a successful solar cell, the keywords are: high efficiency, good reliability and low manufacturing cost.
For MJ cells, the design and practical realization are not an easy task due to the current limitations and the need of tunnel junctions. Furthermore, if the number of junctions increases, the efficiency improves, but also the device complexity and manufacturing costs rise.
In this scenario, *multiterminal solar cells with heterojunction-bipolar transistor structure* can be a good alternative to the traditional DJ solar cells. Indeed, as shown from the study carried out in this thesis, this device is potentially usable as solar energy absorbers, despite the fundamental limitations, such as requiring a long base. Particularly, the efficiency leads to that of a DJ solar cell alongside reducing the number of layers and avoiding tunnel junctions.
Although the simulations of the MT bipolar transistor device lead to a confident conclusion about the possibility of implementation, it is necessary to solve several problems. In fact, this type of solar cell can be also used as a building block for MJ solar cell leading to several challenges on the design and technological levels including but not limited to the necessity to extract additional contacts to connect the sub cells independently. Also many problems are linked to the design and layout of the metal grid.
At the end of this thesis, the hope is that the interest in this new kind of technology and, in general, for photovoltaic devices will grow up in the coming years in order to obtain solar cells more efficient able to become the driving force in the global energy market.

Bibliography

[1] BP. BP Energy Outlook, 2019edition. London, United Kingdom2019.

[2] https://www.youtube.com/watch?v=Z4bSxb5THm4.

[3] https://www.lifegate.com/people/news/greta-thunberg-speech-cop24.

[4] https://en.wikipedia.org/wiki/Planck%27s_law.

[5] https://commons.wikimedia.org/wiki/File:Airmass_geometry.

[6] https://rredc.nrel.gov/solar//spectra/am1.5/ASTMG173/ASTMG173.html.

[7] https://rredc.nrel.gov/solar//spectra/am0/ASTM2000.html.

[8] Simon Sze and Ming K. Lee, *Semiconductor Devices, Physics and Technology*, 3rd ed., Wiley, Hoboken, 2013.

[9] https://www.nrel.gov/pv/assets/pdfs/best-reserch-cell-efficiencies.pdf

[10] Frank Dimroth and Sarah Kurtz, *High - Efficiency Multijunction Solar Cells*, MRS Bulletin, vol 32, March 2007.

[11] A. Martí and A. Luque, *Three-terminal heterojunction bipolar transistor solar cell for high-efficiency photovoltaic conversion*, Nat. Commun. 6:6902doi: 10.1038/ncomms7902, April 2015.

[12] W. Shockley and H. J. Queisser, *Detailed Balance Limit of Efficiency of p-n Junction Solar Cells*, J. Appl. Phys, vol. 32, no. 3, pp. 510-519, March 1961.

[13] M. Sotoodeh; A. H. Khalid; A. A. Rezazadeh, *Empirical low-field mobility model for III-V compounds applicable in device simulation codes*, J. Appl. Phys, vol. 87, no. 6, pp. 2890-2900, March 2000.

[14] Harold J.Hovel, *Semiconductors and Semimetals. Vol 11: Solar Cells*, 1st ed., Academic Press, NY, February 1976.

[15] P. Mazzoldi; M. Nigro; C. Voci, *Elementi di Fisica Vol. 2: Elettromagnetismo e Onde*, 2nd. ed., EdiSES, 2012.

[16] Matthew P. Lumb; Christopher G. Bailey; Jessica G. J. Adams; Glen Hillier; Francis Tuminello; Victor C. Elarde; Robert J. Walters, *Extending the 1-D Hovel Model for Coherent and Incoherent Back Reflections in Homojunction Solar Cells*, IEEE Journal of Quantum Electronics, vol. 49, no. 5, pp. 462-470, May 2013.

[17] Sthephen J. Fonash, *Solar Cell Device Physics*, 2nd ed., Academic Press, NY, 2010.

[18] Antonio Luque and Steven Hegedus, *Handbook of Photovoltaic Science and Engineering*, Wiley, Chichester, 2010.

[19] J. S. Blakemore, *Semiconducting and other major properties of gallium arsenide*, J. Appl. Phys., vol. 53, no. 10, pp. 123181, May 1982.

[20] Xufeng Wang; Mohammad Ryyan Khan; Jeffery L. Gray; Muhammad Ashraful Alamand; Mark S. Lundstrom, *Design of GaAs Solar Cells Operating Close to the Shockley-Queisser Limit*, IEEE Journal of Photovoltaics, vol. 3, no. 2, pp. 737-744, April 2013.

[21] Adel S. Sedra and Kenneth C. Smith, *Circuiti per la microelettronica*, 4th ed., Edises, Napoli, August 2013.

[22] Ali Bahrami; Shahram Mohammadnejad and Nima Jouyandeh Abkenar, *Optimized structure of AlGaAs/GaAs double junction solar cells*, Journal of Modern Optics, vol. 61, no.7, pp. 568-575, DOI: 10.1080/09500340.2014.900123, (2014).

[23] Md. Kamrul Hasan; Lutfun Nahar Lata and Khairul Alam, *Effect of band gap on the performance of AlGaAs/GaAs dual junction solar cell*, IEEE, pp. 64-67, DOI: 10.1109/ICAEE.2017.8255328, September 2017.